



UNIVERSITÀ DEGLI STUDI DI PALERMO

Dottorato in Scienze della Terra - Geochimica
Dipartimento di Scienze della Terra e del Mare (DiSTeM)
GEO/08

**REAL-TIME MEASUREMENT OF VOLCANIC GASES
BASED ON INFRARED SPECTROSCOPY**

**IL DOTTORE
MARIA PEDONE**

**IL COORDINATORE
PROF. FRANCESCO PARELLO**

**IL TUTOR
PROF. ALESSANDRO AIUPPA**

**IL CO TUTOR
ING. GAETANO GIUDICE**

**CICLO XXV
ANNO CONSEGUIMENTO TITOLO 2015**

Contents

Abstract	1
1 Introduction	2
1.1 Motivation	3
1.2 Thesis objectives	6
1.3 Content summary	6
2 Near-infrared Spectroscopy	7
2.1 Infrared Spectroscopy: an introduction	7
2.2 General principles	7
2.3 CO ₂ Structure	11
2.4 Absorption Spectroscopy: Beer-Lambert Law	13
2.5 Laser Spectroscopy	15
2.6 Spectral Lineshapes	16
3 Methods and Techniques	17
3.1 Tunable Diode Laser absorption Spectroscopy (TDLS)	17
3.2 Diode Lasers	17
3.3 Modulation spectroscopy	18
3.4 GasFinder 2.0 Tunable Diode Laser	20
3.4.1 Role of the reference cell to determinate the CO ₂ mixing ratio	22
3.5 Field operations	23
3.5.1 Geometry of field experimental set-up	25
4 GasFinder-dataset processing	26
4.1 Dataset download from GasFinder	26
4.2 Post-processing	27
4.3 Tomographic maps	27
4.3.1 Description of the Matlab Tomographic Algorithm	29
4.3.2 Results on synthetic data	31
4.3.3 Iterative algorithm to create a tomographic matrix for Surfer software	32

4.4 Flux estimates	33
5 Study areas: descriptions, results and discussions	34
5.1 Campi Flegrei	34
5.1.1 Results and Discussions	37
5.1.2 Results from 2014 campaigns	44
5.2 Nea Kameni volcano (Santorini)	46
5.2.1 Results and Discussions	47
5.3 Hekla summit crater (Iceland)	50
5.3.1 Results and Discussions	51
5.4 Krýsuvík area (Iceland)	53
5.4.1 Results and Discussions	54
5.5 Vulcano island	56
5.5.1 Results and Discussions	56
5.6 Paternò	60
5.6.1 Results and Discussions	61
5.7 Furnas volcano (Azores)	66
5.7.1 Results and Discussions	68
6 CO₂ emissions from the analyzed areas: implications	74
6.1 CO ₂ emissions from the investigated areas	74
6.2 Implications to global scale	75
7 Conclusions	79
Acknowledgements	80
References	81
Supplementary Materials	100
Dataset	100

Abstract

The interpretation of volcanic gas datasets offers key information to build/validate geological models relevant to a variety of volcanic processes and behaviours, including eruptions. Major efforts have therefore been spent in recent years to improve our ability to measure volcanic gas compositions and fluxes.

In the last decades, near-infrared room-temperature diode lasers, though in an experimental phase, are finding applications in volcanic gas studies. In this PhD dissertation, I use the GasFinder 2.0, a commercial tunable diode infrared laser transmitter-receiver unit, operating in the 1.3-1.7 μm wavelength range, in the attempt to measure CO_2 mixing ratios and fluxes in volcanic gas emissions.

I initially report on the first field tests conducted at Campi Flegrei volcano (near Pozzuoli, Southern Italy). In later sections, I then focus on observations performed at other degassing systems (Nea Kameni volcano, Greece; Hekla Volcano and Krýsuvík hydrothermal area, Iceland; Furnas volcano, Azores; Vulcano summit crater and Paternò area, Italy). In all such systems, the GasFinder was used to repeatedly measure the path-integrated mixing ratios of CO_2 along cross-sections of the atmospheric plumes of the main fumarolic fields. At each site, an ad-hoc designed measurement geometry was used, using the GasFinder unit and several retro-reflector mirrors, to scan the plumes from different angles and distances. From post-processing of the data using a tomographic Matlab routine, the contour maps of CO_2 mixing ratios in the fumaroles' atmospheric plumes were resolved for each of the manifestations. From their integration (and after multiplication by the plumes' transport speeds), the CO_2 fluxes were evaluated. The so-calculated fluxes range from $\sim 5.7 \pm 0.9$ (Krýsuvík) to $\sim 524 \pm 108$ (Vulcano) tons/day, supporting a significant contribution of fumaroles to the global CO_2 budget. Overall, the results presented in this study contribute to improve understanding of the rates of CO_2 release from sub-aerial volcanism. Our observations suggest, in particular, that the cumulative CO_2 contribution from weakly degassing volcanoes in hydrothermal stage may be more significant at global scale than previously thought.

Chapter 1

1. Introduction

In the last decades, near-infrared room-temperature diode lasers have increasingly been used in atmospheric research (Werle 1998) and, though in an experimental phase, are now finding applications in volcanic gas research (Gianfrani et al. 1997a; 1997b; 2000; De Natale et al. 1998; 2001; Richter et al. 2002; Belotti et al. 2003; De Rosa et al. 2007). Prototypes for simultaneous detection of CO₂ and H₂O mixing ratios in volcanic gas mixtures are under testing (Gagliardi et al. 2001), and the possibility to measure the isotope (¹³C/¹²C) composition of volcanic carbon (Gagliardi et al. 2002; 2003; Weidmann et al. 2005) has also been recently explored. Yet, the application of lasers to volcanic gas studies is still an emerging research field, and requires more testing and validation experiments.

In this thesis, the use of Tunable Diode Laser Spectrometers (TDLS) for estimating volcanic/hydrothermal CO₂ fluxes from dormant volcanoes is explored. I report on the results of TDL observations I conducted in a selected number of volcanic/hydrothermal areas: Campi Flegrei, Vulcano Island, and Paternò mud volcano (all in Italy); Nea Kameni (Santorini, Greece), Hekla and Krýsuvík (Iceland) and Furnas (Azores). These volcanoes were selected because they display a range of fumarolic activity, from weak (Hekla) to moderate (Vulcano Island). While there are strong arguments for that the global volcanic CO₂ budget is dominated by a relatively small number of strong emitters (Shinohara 2013), it remains that are weakly degassing volcanoes that dominate - at least in number - the population of historically active volcanoes on Earth. The CO₂ output from these passive, sluggish emissions needs to be better explored and quantified.

The purposes of the PhD thesis are: (1) to present an experimental set-up for measuring volcanic gas manifestations via a Tunable IR Laser; (2) to test the performance of a tomographic technique to contouring CO₂ mixing ratios in volcanic plumes, (3) to use the tomographic reconstruction to estimate CO₂ fluxes and (4) to characterise the typical levels of CO₂ emission from feeble volcanic point sources in solfatara stage of activity.

1.1 Motivation

The chemical composition of volcanic gas emissions can provide hints onto the mechanisms of magma ascent, degassing and eruption (Allard et al. 2005; Burton et al. 2007; Oppenheimer et al. 2009; 2011), and can add useful information for interpreting the dynamics of fluid circulation at dormant volcanoes (Giggenbach 1996; Chiodini et al. 2003; 2012).

Carbon dioxide (CO₂) is, after water vapour, the main constituent of volcanic (Giggenbach 1996) and hydrothermal (Chiodini et al. 2005) gases, and has attracted the attention of volcanologist because it can effectively contribute to track magma ascent prior to eruption (Aiuppa et al. 2007; 2010). Volcanic gases have traditionally been monitored by means of direct in-situ sampling of fumaroles (Fischer 2008), followed by laboratory analysis (Symonds et al. 1994).

Giggenbach's (1975) soda flasks allow several species to be measured simultaneously, but requires post-collection chemical determinations in a laboratory, that preclude any real-time continuous monitoring of volcanic activity.

In addition, direct sampling is often impractical and hazardous, particularly during eruptions, or of too low temporal resolution. Efforts have therefore been made (since the 1970s) to improve volcanological applications of optical remote-sensing techniques, including the Correlation Spectrometer (COSPEC; Millan et al. 1985), Differential Optical Absorption Spectroscopy (DOAS; Galle et al. 2003), Light Detection and Ranging (LIDAR; Svanberg 2002) or open-path Fourier Transform Infrared spectroscopy (FTIR; Francis et al. 1998). These optical techniques rely on resolving the wavelength-dependent "fingerprints" of target molecules. They have proved particularly successful in the UV region of the electromagnetic spectrum, where volcanic SO₂ can strongly absorb radiation (typically scattered sunlight), enabling estimation of SO₂ fluxes (Oppenheimer 2010).

The SO₂ flux has been widely measured for volcano monitoring purposes, demonstrating its utility as a tracer of magmatic processes (Edmonds et al. 2003; Caltabiano et al. 2004), and as a precursor to eruptive activity (Daag et al. 1996).

In contrast, measurement of H₂O and CO₂ fluxes, the two major volcanic gas components, has long been a goal of volcanology, yet one frustrated by the dwarfing of the volcanogenic signals by these species' high atmospheric background levels (Aiuppa et al. 2008).

Fourier transform Infra Red (FTIR) spectrometers have valuably been used for both active (e.g., using an artificial IR lamp; Burton et al. 2000) and passive (using the magma or hot rocks as source; Allard et al. 2005; Burton et al. 2007; Sawyer et al. 2008; Oppenheimer et al. 2009) observations of volcanic CO₂ mixing ratios in plumes.

Fourier Transform Infra Red (FTIR) spectroscopy has been used to record the total gas composition from some volcanoes, e.g., Stromboli (Burton et al. 2007), Yasur (Oppenheimer et al. 2006), Masaya (Burton et al. 2000) and Nyiragongo (Sawyer et al. 2008). H₂O and CO₂ FTIR measurements have been carried out in attempt to estimate the fluxes of these species e.g., at Etna volcano (Allard 2005).

Aiuppa et al. (2007; 2008) and Shinohara et al. (2008) reported H₂O, CO₂ and SO₂ concentration time series detected in the plumes (from Etna's summit vents), using the MultiGAS technique. Combining MultiGAS measurements and remotely sensed SO₂ fluxes they made the first assessment of Etna's H₂O flux, and extended further the limited CO₂ emission database (Allard et al. 1991; Aiuppa et al. 2006).

Attempts to estimate the CO₂ flux were carried out by Yoshimura et al. (2013) analysing melt inclusion (MI) in Etna's samples characterized by high CO₂/H₂O. Starting from MI data and the detailed eruption history (duration of CO₂ fluxing), they estimated a CO₂ flux of 2.4–6.0 kt/day, consistent with the observed CO₂ emission rate of 1–10 kt/day (Aiuppa et al. 2008) for the same period (Fig. 1.1).

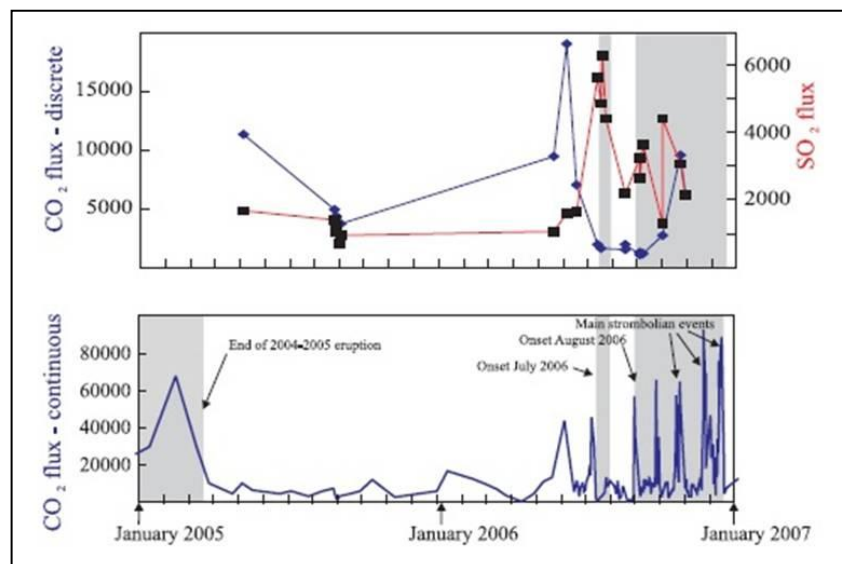


Fig. 1.1 Plots taken from Aiuppa et al. 2008. Top: SO₂ (red, right scale) and CO₂ (blue, left scale) fluxes (all fluxes in tons/day); the former obtained from car traverses, and the latter by multiplying these SO₂ emission rates by the Voragine crater CO₂/SO₂ ratios. Bottom: CO₂ fluxes obtained by multiplying data from the permanently installed Multi-GAS at Voragine crater and the network of UV scanning spectrometers. The unshaded areas represent periods of passive degassing from the central craters; whilst the grey areas mark periods of semi-continuing effusive and mild-explosive eruptive activity at the South-East Crater.

CO₂ emissions from fumarolic fields can be determined through the introduction of a known flux of a tracer gas (e.g. SF₆). Measuring the volcanic CO₂/SF₆ ratio in emissions placed downwind, Mori et al. (2001) calculated the CO₂ flux at fumarolic vents at Izu-Oshima and Kirishima (Japan) and Teide (Canary Islands, Spain). Most previous assessment of the CO₂ flux have been obtained indirectly from co-acquired SO₂ fluxes and volcanic gas CO₂/SO₂ ratios (Aiuppa et al. 2006; 2010; McGonigle et al. 2008; Burton et al. 2009). The available dataset of volcanic CO₂ fluxes is however still fragmentary, and estimates of the global volcanic CO₂ flux are poorly accurate (Burton et al. 2013).

The measurement of the soil CO₂ flux, received more attention for both geothermal prospection and volcanic surveillance. The soil CO₂ flux, is a permeability-indicator and can be used as a prospecting tool to locate geothermal reservoirs of different temperature (Chiodini et al. 1998). To determinate the soil CO₂ flux, both indirect and direct methods are known.

The direct methods for the determination of soil CO₂ flux require dynamic or static procedures. The dynamic procedures consist in the measurement of CO₂ concentration in a known air soil flux, through an inverted chamber and across a known surface of the soil (e.g. Reinert 1968; Kucera and Kirkham 1971). Gurrieri and Valenza (1988) inserted in the soil a pipe opened at the base (1.3 cm in diameter and 50 cm long). A known flux of gas is pumped out from the base of the pipe and the CO₂ concentration of this gas is continuously measured. The sucked gas is replaced by atmospheric air entering the top of the pipe. After a given time, the CO₂ concentration reaches a constant value termed “dynamic concentration (Cd)” which is proportional to the soil CO₂ flux (Diliberto et al. 2002). However, in order to calculate soil CO₂ flux, the “Cd” value must be multiplied by a factor which depends on the experimental device, working conditions as well as physical characteristics of the soil in each measurement point.

Many researchers have performed soil CO₂ flux measurements by using static techniques which utilize an alkaline solution (e.g. Lieth and Ouelletle 1962; Cerling et al. 1991), or solid soda lime (Edwards 1982; Cropper et al. 1985) to absorb CO₂ that is released from the soil into an inverted and closed container. Another static technique for measuring the soil CO₂ flux consists of the determination of the rate of increase in the CO₂ concentration within an inverted chamber placed on the soil surface. This technique, known as the accumulation chamber method or closed-chamber method, has been successfully used, at the beginning, in agricultural sciences to determine soil respiration (Parkinson, 1981) and

to measure the flux from the soil of other gaseous species, e.g., N₂O (Kinzig and Socolow, 1994), and CO₂ (Chiodini 1998; Viveiros 2010).

The volcanic/hydrothermal CO₂ flux sustained by diffuse soil degassing can relatively easily be measured both in surveys (Reiners 1968; Kucera and Kirkham 1971; Kanemasu et al. 1974; Parkinson 1981; Chiodini et al. 1996a; Favara et al. 2001; Hernandez 2001; Rogie 2001; Cardellini et al. 2003; Chiodini et al. 2005; Inguaggiato et al. 2005; Pecoraino et al. 2005; Mazot et al. 2011; Inguaggiato et al. 2012; Burton et al. 2013) and with permanent installations (Brusca et al. 2004; Carapezza et al. 2004; Werner and Cardellini 2006; Inguaggiato et al. 2011).

1.2 Thesis objectives

This study reports on the results of measurement field surveys conducted with a commercial IR Diode Laser system (GasFinder 2.0) at several volcano targets. A new post-processing routine is also presented, which allows for the volcanic CO₂ output to be quantified for each of the investigated areas. As such, the presented results add novel information on the CO₂ degassing regime of quiescent volcanoes in solfatara stage of activity, and on their potential contribution to the global volcanic CO₂ budget.

1.3 Content summary

This thesis is divided into four main sections:

Section 1: Introduction (Chapter 1)

Section 2: Theory and Methodologies (Chapters 2-3-4)

Section 3: Results and discussions (Chapters 5-6)

Section 4: Conclusions (Chapter 7)

Chapter 2

Near-infrared Spectroscopy

2.1 Infrared Spectroscopy: an introduction

Spectroscopy is the study of the absorption and emission of light and other radiations by matter, and of the dependence of these processes on the wavelength of the radiation. More recently, the definition has been expanded to include the study of the interactions between particles such as electrons, protons, and ions, as well as their interactions with other particles as a function of their collision energy.

Spectroscopic techniques, applied in virtually all technical fields of science and technology, are extremely sensitive. Single atoms and even different isotopes of the same atom can be resolved among 10^{20} or more atoms of a different species. Trace amounts of pollutants or contaminants are often detected most effectively by spectroscopic techniques.

Spectroscopy is actually a measure of the interaction of photons with matter as a function of the photon energy. The energy E of a photon (a quantum of light) is related to its frequency ν by the relation $E = h\nu$, where h is Planck's constant.

2.2 General principles

Electromagnetic radiation is composed of oscillating electric and magnetic fields that have the ability to transfer energy through space. The energy propagates as a wave, such that the crests and troughs of the wave move in vacuum at the speed of 299,792,458 metres per second. The distance between successive crests in a wave is called wavelength. The various forms of electromagnetic radiation differ in wavelength. For example, the visible portion of the electromagnetic spectrum has wavelengths ranging between 4×10^{-7} and 8×10^{-7} metre. The decomposition of electromagnetic radiation into its component wavelengths is fundamental to spectroscopy.

The frequency with which the electromagnetic wave oscillates is also used to characterize the radiation. The product of the frequency (ν) and the wavelength (λ) is equal to the speed of light (c); *i.e.*, $\nu\lambda = c$. The frequency is often expressed as the number of oscillations per second, and the unit of frequency is hertz (Hz), where one hertz is one cycle per second.

Vibrational Spectroscopy is used as a tool for studying the structures of atoms and molecules. The large number of wavelengths emitted by these systems makes it possible to investigate their structures in detail, including the electron configurations of ground and various excited states.

It also provides a precise analytical method for finding the constituents in material having unknown chemical composition. In a typical spectroscopic analysis, a concentration of a few parts per million of a trace element in a material can be detected through its emission spectrum.

The model for the vibrational motion of a diatomic molecule is the one-dimensional harmonic oscillator. An oscillator is a system capable of converting periodicity with the potential energy into kinetic energy and vice versa; the oscillator is harmonic if the dynamics are described by the relation: $f = -kx$, which indicates that the returning force (f) is proportional to the contrary of the shift (x) from the equilibrium position through the constant k . In other words, vibrational spectroscopy can be thought of by starting with a simple harmonic oscillator model. In this model, two atoms are joined by a bond to be equivalent to two masses joined by a spring. The spring can be compressed, forcing the spheres close to each other - stretched, moving them apart - or allowed to freely come to rest in the spheres' equilibrium positions. This can be shown in a potential energy curve (Fig. 2.1).

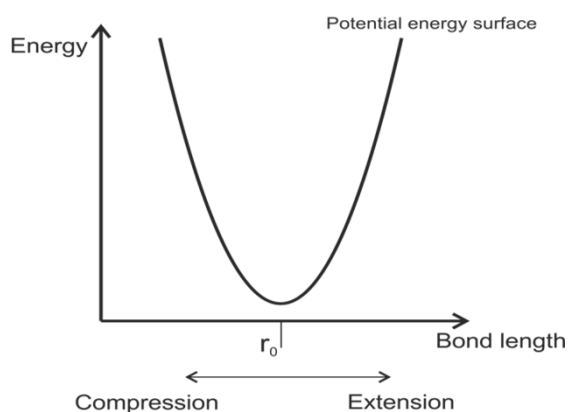


Fig. 2.1 Simple harmonic oscillator model. Two atoms are joined by a bond to be equivalent to two masses joined by a spring. The spring can be compressed, forcing the spheres close to each other - stretched, moving them apart - or allowed to freely come to rest in the spheres' equilibrium positions. See text.

The potential energy function is given by the expression (2.1):

$$V = -\int f dx = \frac{1}{2} kx^2 \quad (2.1)$$

that is a harmonic oscillator is characterized by a potential energy of parabolic type (Fig. 2.1).

The possible vibrational states are given by the vibration quantum number, v , and vibrational selection rule $\Delta v = \pm 1$ where the positive sign corresponds to the absorption and the negative to the emission.

The energy of each level, E_v , is given by:

$$E_v = (v + \frac{1}{2})h\nu \quad (2.2)$$

where ν is the fundamental frequency.

The fundamental frequency is given by the equation:

$$\nu = (1/2\pi) \times (k/\mu)^{1/2} \quad (2.3)$$

where μ is the reduced mass of the molecule, and k is the bond force constant. Note that this k is similar to the spring force constant from Hooke's Law. This leads to a potential energy surface as that shown in figure 2.2.

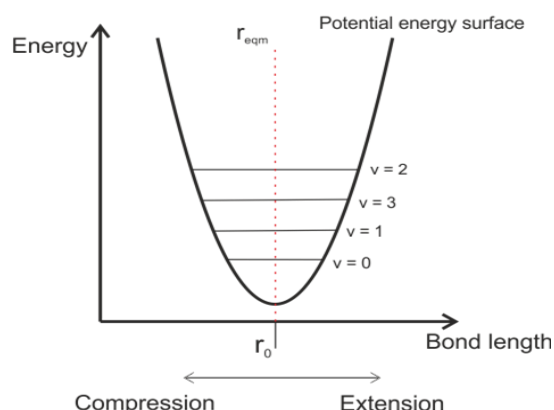


Fig. 2.2 Simple Harmonic Oscillator model in which the possible vibrational states are given. The energy levels are equally spaced, and the equilibrium bond length is constant for all energy levels.

The energy levels are equally spaced, and the equilibrium bond length is constant for all energy levels. However, this model is imperfect - it does not account for the possibility of bond dissociation (under this model, the bond would never break, no matter the magnitude of the vibrational energy). It also does not account for extra repulsive effects at very small bond lengths caused by the electroweak force. This is the force which prevents atoms from being forced together as the distance between them gets very small (the reason nuclear fusion only occurs at very high temperatures, for example). A model which takes into

account these factors, and which more accurately models a vibration diatomic molecule, is the Anharmonic Oscillator, and the corresponding potential energy surface called the Morse potential. The corresponding potential energy curve is shown in figure 2.3.

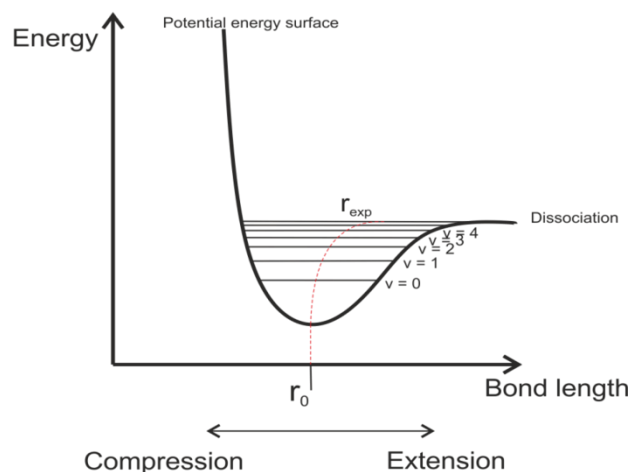


Fig. 2.3 Anharmonic Oscillator model of the diatomic molecule vibration, which includes the possible bond dissociation. Bond length is not the same for all energy levels.

In this model, the bond length is not the same for all energy levels. One effect of the anharmonicity is this deformation as the energy of the vibrations increases. Another is that now, the vibrational energy levels are no longer equally spaced, but instead get closer together as the vibrational quantum number increases. This model also illustrates that the number of vibrational energy levels is not infinite - above some energy, the bond breaks and the molecule dissociates.

In the infra-red (IR) region of the electromagnetic spectrum, vibrational energies occur roughly in the $100 - 4000 \text{ cm}^{-1}$ (about $1 - 50 \text{ kJ mol}^{-1}$). The fundamental principle for obtaining a vibrational spectra is that the electric dipole moment of the molecule must change during the vibration. If there is no change in dipole moment, then this particular vibration will not give rise to any absorption in the IR region. An example of this can be seen below for the symmetric stretch mode of carbon dioxide. Because both C=O bond lengths change exactly in phase, there is never a net dipole moment on the molecule. A homonuclear diatomic molecule such as dioxygen (O_2) has zero dipole moment, so it has no IR spectrum.

The number of modes (types) of vibration can be predicted for a molecule, containing N atoms, using the following general expressions (Table 2.1). For linear molecule (such as CO_2), the possible “normal vibration modes” rise to $3N-5$; where N is the atoms number.

Table 2.1 The number of modes (types) of vibration.

Linear molecules	Non-linear molecules
$3N - 5$	$3N - 6$

2.3 CO₂ Structure

Linear molecules such as CO₂ can generally be treated as diatomics with regard to their moments of inertia. The moment of inertia on the A-axis (I_A), along the molecule (figure 2.4), is approximately zero: and the other two moments (I_B and I_C) are equal ($I_B = I_C$).

Figure 2.4 shows two axes of symmetry of CO₂, including an infinite number of C₂ axes that align through the C atom and perpendicular to the bonds. These axes are two-fold symmetric, thus a rotation of 180° produces an indistinguishable change. In addition, CO₂ has the C_∞ axis along the molecule, along which an infinite number of rotations produces no distinguishable change in orientation. Because CO₂ has an ∞-fold axis C_∞ that is perpendicular to an infinite number of planes of symmetry, it belongs to the point group D_{∞h} and has a symmetry number $\sigma=2$ (Herzberg 1991).

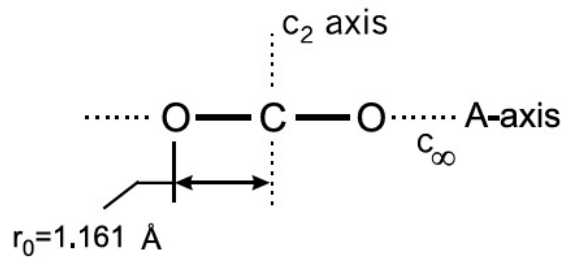


Fig 2. 4 CO₂ axes of symmetry.

Table 2.2 shows the main properties of CO₂ molecule (Khristenko 1998). Since CO₂ is linear and symmetric, it does not have a permanent dipole moment. Thus, CO₂ is only spectroscopically active in the IR when a dipole is induced due to bending or asymmetric stretching (as explained above; see also Figure 2.5).

Table 2.2 CO₂ property (by Khristenko 1998).

Property	Value
Mass	44 [uma]
Bond length	$r_0 (\text{CO}) = 1.162 [\text{\AA}]$
Rotational constant	$B_0 = 0.390 [\text{cm}^{-1}]$
Symmetry number	$\sigma = 2$

Carbon dioxide has four classically-described vibrational modes, of which two bending modes are degenerate, as shown in Figure 2.5.

The two stretching modes, asymmetric and antisymmetric, are parallel vibrations (symbol \parallel), since the vibrations occur parallel to the main symmetry axis and the bending modes are perpendicular, since they induce changes in the molecule that are perpendicular to the main symmetry axis (Fig. 2.5). Only the vibrations that induce a dipole moment are spectroscopically active in the Infra-Red.

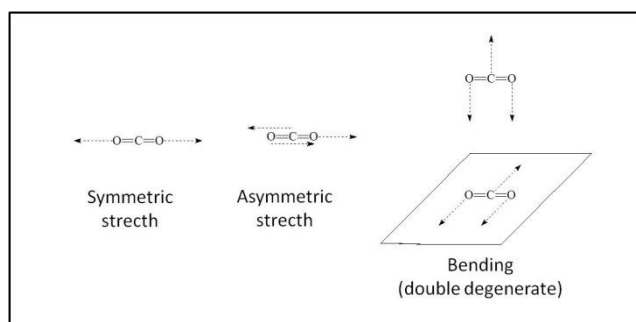


Fig 2.5 CO₂'s vibrational modes. See text.

In detail, the symmetric stretch of CO₂ does not modify the dipole moment which remains zero before and after the oscillation: this is IR inactive. Instead, modes of asymmetric stretching and bending are associated with changes of the dipole moment and therefore are IR active. In the asymmetric stretching, the dipole moment varies along the direction parallel to the molecular axis and the spectral transition band is called therefore parallel. Instead, in bending, the dipole moment is perpendicular to the axis and the transition band is called perpendicular. These features are shown in Table 2.3 (Khristenko 1998).

Table 2.3 Fundamental vibrations, frequencies, types and descriptions for CO₂ (by Khristenko 1998).

Vibration	Frequency [cm ⁻¹]	Type	Description	IR-active?
ν_1	1333	\parallel	Symmetric stretch	No
ν_2	667	\perp	Bending (Degenerate)	Yes
ν_3	2349	\parallel	Asymmetric stretch	Yes

2.4 Absorption Spectroscopy: Beer-Lambert Law

The energy of infrared radiation produces a change in a molecule's or a polyatomic ion's vibrational energy, but is not sufficient to effect a change in its electronic energy. As shown in figure 2.6, vibrational energy levels are quantized; that is, a molecule may have only certain, discrete vibrational energies. The energy for an allowed vibrational mode, E_v , is: $E_v = v + (1/2)h\nu_0$, where v is the vibrational quantum number, which has values of 0, 1, 2, ..., and ν_0 is the bond's fundamental vibrational frequency. The ν_0 value, which is determined by the bond's strength and by the mass at each end of the bond, is a characteristic property of a bond.

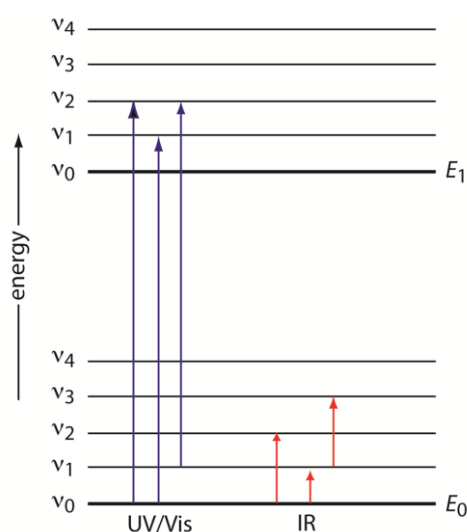


Fig. 2.6 Diagram showing two electronic energy levels (E_0 and E_1), each with five vibrational energy levels (v_0 – v_4). Absorption of ultraviolet and visible radiation leads to a change in the analyte's electronic energy levels and, possibly, a change in vibrational energy as well. A change in vibrational energy without a change in electronic energy levels occurs with the absorption of infrared radiation.

The fundamental theory governing absorption spectroscopy is embodied in the Beer-Lambert law (Eq. 2.4). The ratio of the transmitted intensity (I_t) and initial (reference) intensity (I_0) of monochromatic laser radiation at a particular frequency is exponentially related to the absorption transition's linestrength S_i [$\text{cm}^{-2}\text{atm}^{-1}$], lineshape function ϕ [cm], total pressure P [atm], mole fraction of the absorbing species x_j , and the pathlength L [cm] through which the radiation passes:

$$\frac{I_t}{I_0} = \exp(-S_i \phi P x_j L) \quad (2.4)$$

The Beer's law suggests a linear dependence between the species absorbance and its concentration. In many cases a calibration curve deviates from this ideal behaviour (Fig. 2.7). Deviations from linearity are divided into three categories:

- Fundamental
- Chemical
- Instrumental.

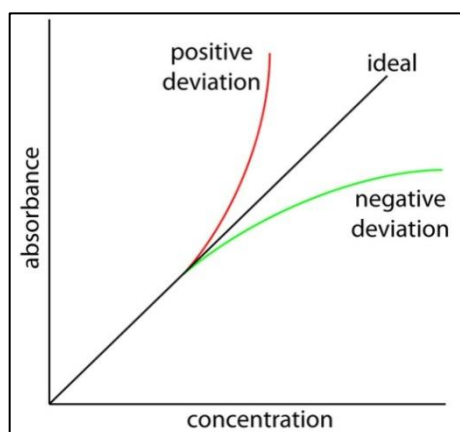


Figure 2.7 Calibration curves showing positive and negative deviations from the ideal Beer's law calibration curve, which is a straight line.

The fundamental deviation arises from the fact that, at higher concentrations, the individual particles of a given analyte no longer behave independently of each other. The resulting interactions between particles may change the analyte's absorptivity. An additional aspect is that the analyte's absorptivity depends on the sample's refractive index (a function of the analyte's concentration itself). It is only at low concentrations of analyte that the refractive index is essentially constant, and the calibration curve linear. A chemical deviation from Beer's law may occur if the analyte is involved in an equilibrium reaction. Finally, a principal instrumental limitations affect Beer's law linearity. The limitation is that Beer's law assumes that the radiation reaching the sample is of a single wavelength - that is, that the radiation is purely monochromatic. As shown in Figure 2.8, however, even the best wavelength selector passes radiation with a small, but finite effective bandwidth. Polychromatic radiation always gives a negative deviation from Beer's law. For this reason, as shown in Figure 2.8, absorbance measurements are recommended at the top of a broad absorption peak.

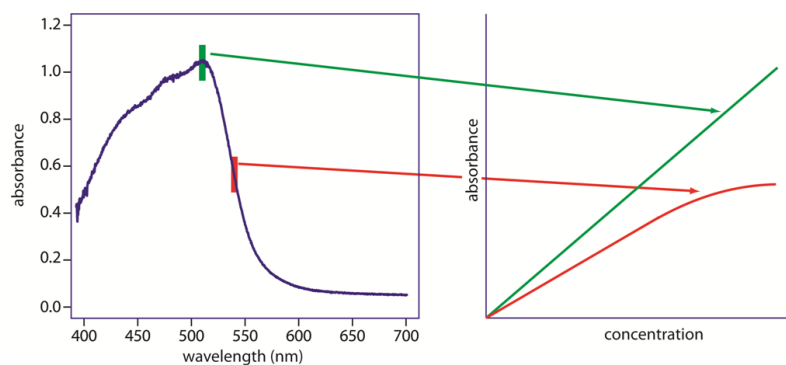


Figure 2.8 Example of the effect of the wavelength choice on the linearity of a Beer's law calibration curve. The green calibration curve has an higher slope - a greater sensitivity - than the red calibration curve.

2.5 Laser Spectroscopy

Lasers are line sources that emit high-intensity radiation over a very narrow frequency range. The invention of the laser by the american physicists Arthur Schawlow and Charles Townes in 1958, the demonstration of the first practical laser by the american physicist Theodore Maiman in 1960, and the subsequent development of laser spectroscopy techniques, revolutionized a field that had previously seen most of its conceptual developments before the 20th century (Enciclopedia Britannica <http://www.britannica.com/EBchecked/topic/558901/spectroscopy>).

Intense, tunable (adjustable-wavelength) light sources now span most of the visible, near-infrared, and near-ultraviolet portions of the spectrum.

As it will explain in the next chapter, there are several advantages to using a laser light source: (1) the light from lasers can be made highly monochromatic (light of essentially one "colour" - *i.e.*, composed of a very narrow range of frequencies). As the light is tuned across the frequency range of interest, extremely narrow spectral features can be measured; (2) laser light in a given narrow frequency band is much more intense than virtually all broadband sources of light used in spectroscopy. A potential limitation to spectroscopic sensing of gases is due to the motion of the atoms or molecules relative to the observer. The Doppler shifts that result from the motion of the atoms will broaden any sharp spectral features. A gas cell will have atoms moving both toward and away from the light source, so that the absorbing frequencies of some of the atoms will be shifted up while others will be shifted down.

2.6 Spectral Lineshapes

The lineshape function ϕ reflects the relative variation in the spectral absorption coefficient with frequency. Since it is normalized, the lineshape integrated value over frequency is equal to unity (Eq. 2.5)

$$\int_{-\infty}^{+\infty} \phi dv = 1 \quad (2.5)$$

Figure 2.9 shows a typical lineshape of an isolated absorption line centered at ν_0 as a function of frequency. The lineshape has a maximum value at a frequency ν_0 . The width of the feature, (Fig. 2.9), is defined by the width at half the maximum value (the full width at half maximum, or, FWHM). Since the units of $d\nu$ are typically either cm^{-1} or s^{-1} , $\phi(\nu)$ will have units of centimeters or seconds respectively.

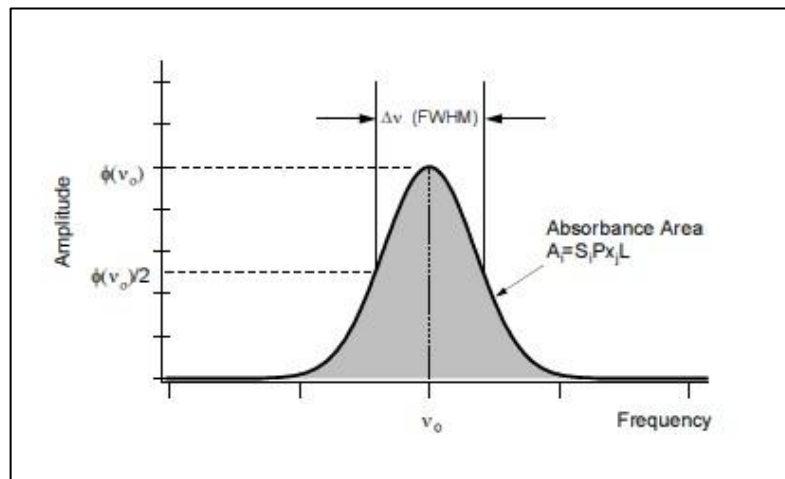


Fig. 2.9 Example of lineshape as a function of frequency.

Ideal lineshapes include Gaussian, Lorentzian, and Voigt functions, whose parameters are the line position, maximum height and half-width.

Chapter 3

Methods and Techniques

3.1 Tunable Diode Laser absorption Spectroscopy (TDLS)

The Tunable Diode Laser Spectroscopy technique (TDLS) relies on measuring the absorbance due to the absorption of IR radiation (at specific wavelengths) by a target gas. Rather than using a continuous-wavelength light source and sensing across a wide band of the infrared spectrum (as FTIR), TDLS employs a light source of very narrow line-width that is tunable over a narrow wavelength range. In other words, TDL steams on absorption spectroscopy using a single isolated absorption line of the target species. TDLS typically has spectral resolution narrower than Doppler line widths, which permits positive identification and unambiguous measurement of complex gas mixtures. An additional advantage of TDLS is increased sensitivity, since the narrow laser line-width allows one to measure accurately small absorbances due to specific rotational lines in a vibration-rotation spectrum with high selectivity. Additional characteristics of TDLS include:

- temporal resolution of ~ 1 Hz;
- intense laser light concentrated at the absorption wavelength, enabling path-lengths of up to 1 km to be measured;
- wide measurement range;
- self-calibration, through an internal reference cell;
- no “poisoning” or degradation of the instrument with long-term exposure to a gas.

A major disadvantage is that TDLS applications are better suited to accurate measurement of a specific target gas (known to be present in the atmosphere) than for identification of previously unidentified species.

3.2 Diode Lasers

Lead-salt tunable diode lasers were first developed in the mid 1960s. Diode lasers made from Group III (Ga, Al and In) and Group V (P, As and Sb) elements, that emit at

wavelengths under 2 μm (5000 cm^{-1}) (Schiff et al. 1994a; Schiff et al. 1994b; Werle et al. 2002), can be used for carbon dioxide measurement.

A diode is typically mounted onto a support such as copper, that serves as a temperature controller during operation. When an electrical current is applied, the diode emits light spontaneously at a wavelength corresponding to the energy band gap in the semiconductor. Laser action results from reflections from the end-faces of the crystal. This gap depends on the chemical composition of the laser and hence different wavelengths can be produced by altering the diode composition. Tuning of the emitted wavelengths can be accomplished, in principle, through variation of one of three possible parameters: applied magnetic field strength, diode temperature, and hydrostatic pressure. In practice, a change in temperature, which can be obtained by changing the current through the diode, is generally used.

3.3 Modulation spectroscopy

The output at a given current is a series of longitudinal modes whose separation is determined by $(2nL)^{-1}$, where n is the index of refraction of the salt (usually 4.5-7) and L is the length of the laser cavity, i.e., separation of the end-faces of the crystal (typically 300-400 μm). A number of different modulation techniques can be used to increase the signal-to-noise ratio (Schiff et al. 1994a; Schiff et al. 1994b). The most commonly used method for accurately measuring small gas amounts, and to discriminate against background signals, is to modulate the frequency output of the laser (Reid et al. 1978; Schiff et al. 1994a). The instantaneous laser frequency is:

$$f(t) = f_0 + m\gamma \times \sin(2\pi f_m t) \quad (3.1)$$

Where f_0 is the laser centre frequency, m is the frequency modulation index, γ is the half width at half maximum of the absorption line, and f_m is the modulation frequency. If $f_m \ll \gamma$ this is referred to as wavelength modulation spectroscopy (WMS), otherwise it is called frequency modulation spectroscopy (FMS) (Linnerud et al. 1998). In conventionally labelled 2f detection (Linnerud et al. 1998), as in the case of the GasFinder, a sinusoidal frequency modulation is applied to a probe laser, which is then scanned across a sharp absorption peak (Weida 2007). Figure 3.1 is an example which shows that the absorption peak works as a transducer to convert the frequency modulation into a sinusoidal amplitude modulation. In detail, if the laser is modulated over the central absorption peak ("A" in Fig. 3.1), the resulting amplitude modulation is two times the frequency

modulation. If the laser is centered on the side of the peak (“B” in Fig. 3.1), the sinusoidal amplitude modulation is at the same frequency. Instead, modulating the frequency at the flat absorption baseline, no amplitude modulation is observed (Weida 2007).

The benefits of modulation spectroscopy in TDL are twofolds. Firstly, it produces a signal directly proportional to the species concentration; secondly, it allows the signal to be detected at a frequency at which the laser noise (one of the two main factors limiting sensitivity) is much reduced.

After signal modulation, the emitted beam propagates through the atmosphere to reach a retroreflector, which reflects it back to the detector inside the receiver/laser unit. To discriminate against net offsets, broad absorption features and interfering signals in the background, the returning radiation is demodulated. If the resulting amplitude-modulated signal is demodulated at twice the laser frequency modulation, the second derivative of the absorption peak is obtained. This, known as the “2f signal” (red curve in Fig. 3.2), is the case of the technique used here. As shown in figure 3.2, the demodulated signals are sensitive to the overall absorption (see the slope or the curvature of the absorption feature for the “1f” and “2f” signals, respectively). In this case, in 2f-detection, this produces a negative-going signal that is proportional to the absorption of the radiation by the investigated specie.

Atmospheric carbon dioxide measurements using a tunable diode laser based system have recently described by Humphries et al. (2008).

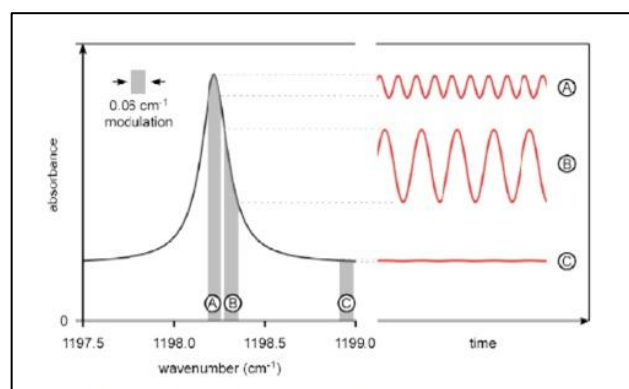


Fig. 3.1 Example of broadened transition acting as a transducer for a sinusoidal frequency modulation (from Weida 2007).

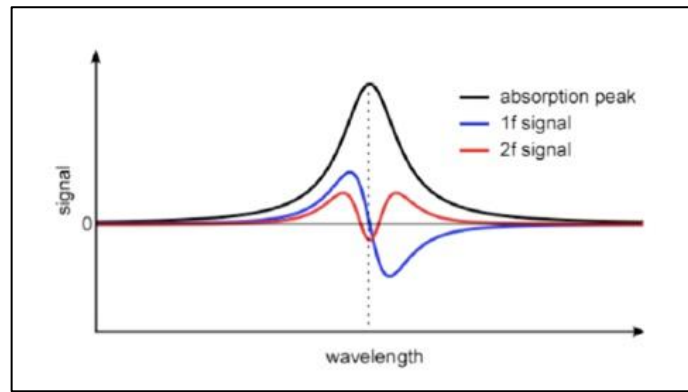


Fig. 3.2 Lorentzian absorption peak and corresponding 1f and 2f demodulated signals obtained from scanning frequency modulated laser over peak. The signals (1f and 2f) yield the first and second derivatives of the peak, respectively.

3.4 GasFinder 2.0 Tunable Diode Laser

The instrument used in this study is a GasFinder 2.0 Tunable Diode Laser (produced by Boreal Laser Inc.), a transmitter/receiver unit that can measure CO₂ mixing ratios over linear open-paths of up to 1 km distance. The laser source consists of a near-infrared room temperature tunable diode laser operating in the 1.3-1.7 μm wavelength range, where CO₂ has a single absorption line. Radiation emitted by the IR laser transmitter propagates to a retro-reflector mirror (single or triple corner cube, gold plated, figure 3.3), where the beam is reflected back to the receiver and focused onto a photodiode detector.

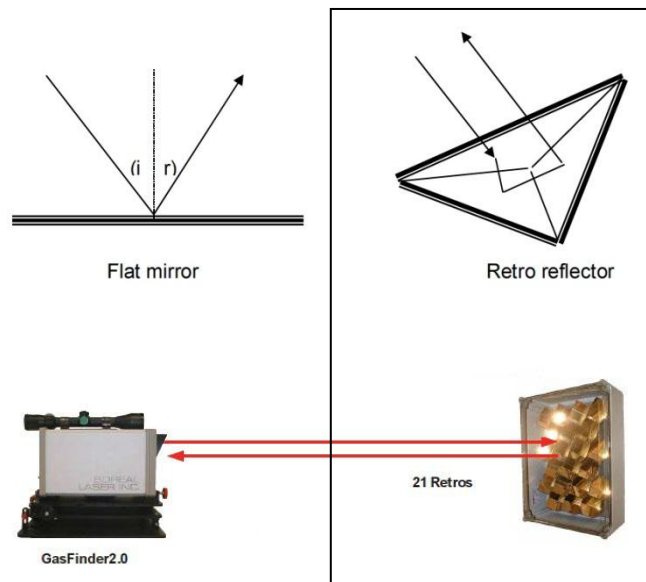


Fig. 3.3 A retroreflector is different from a flat mirror (top panel) in that the reflected light returns in the same direction as the incident light. A retroreflector is like a section through a corner and has three faces that form the inside corner of a cube. In the down panel a scheme of radiation beam path from the GasFinder 2.0 and a retroreflectors array (21 retro elements) and vice versa.

The laser beam, when emitted from the GasFinder 2.0, is about 1mm in diameter (Boreal Laser Inc. 2007). It diverges at about 1.5 milli-radians, so at 100 m the diameter of the beam is 150 mm and at 600 m the diameter is about 1 m. This divergence allows for a small movement of the GasFinder without becoming non-aligned. However there is a “sweet spot” (Fig. 3.4) in the centre of the beam which is used when making the initial alignment (before each acquisition). This is where the returning light value (see below) and the signal strength are at maximum.

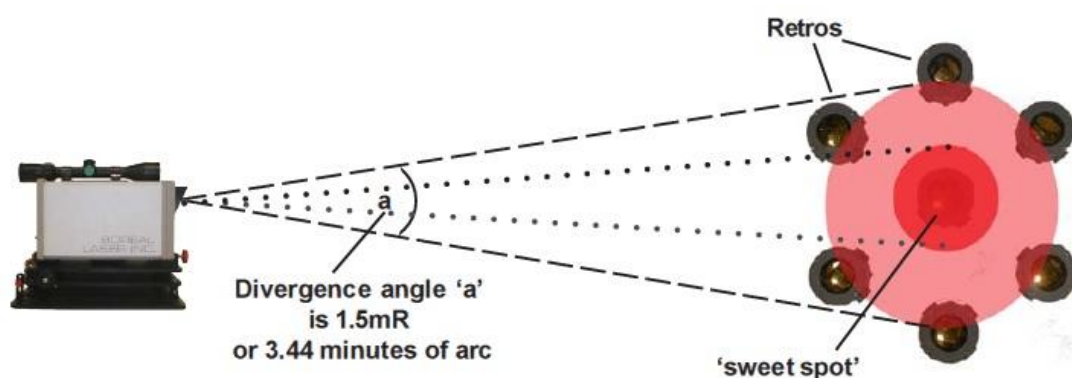


Fig. 3.4 Divergence of the laser beam emitted from the GasFinder 2.0. See text.

A portion of the emitted beam passes through a reference cell (with known and stable CO₂ reference mixing ratio), inside the GasFinder unit, which allows for continuous calibration. The signals received from the retro-reflector mirror and from the reference cell are converted into electrical waveforms, and processed to determine in real-time CO₂ column amounts (in ppm·m) along the optical path, using the procedure described in Tulip (1997). The computed gas mixing ratio is then displayed on the back-panel of the instrument, and can be transmitted to a computer and collected. Figure 3.5 is a schematic representation of GasFinder 2.0.

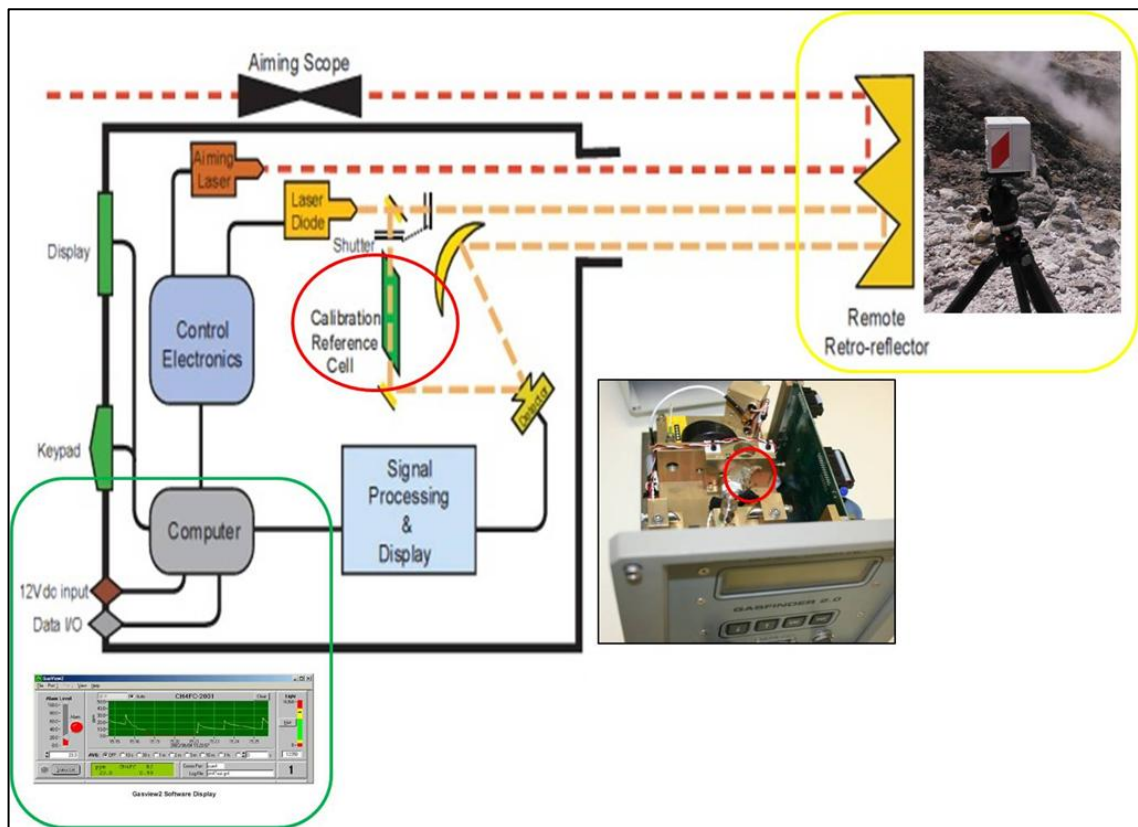


Fig. 3.5 Schematic representation of GasFinder 2.0. See text.

3.4.1 Role of the reference cell to determinate the CO₂ mixing ratio

Estimating the density of the detected gas is achieved by passing the laser light through a reference cell-gas and comparing the detected signal from the target zone with the detected signal from the reference cell-gas. The receiver unit includes: a photo detector for producing a detected signal as output from the laser that has passed through the target zone; a reference signal generator to create a reference signal by detection of light that has passed through the target zone; the reference signal having a frequency corresponding to a modulation frequency of the light output from the laser; and a mixer for mixing the detected sample signal and the reference signal to produce mixer output. The presence of the target gas is determined by a signal analyzer connected to the mixer.

Moreover, measuring the density of the target gas density is possible by comparing the intensity of detected signal (that passed through the target-sample zone) and the intensity of reference signal (that passed through the reference cell containing a sample of the target gas).

Noise reduction can be achieved by adjusting the phase difference between the reference and detected signals and tuning the laser to transmit radiation at a frequency that is absorbed by the target gas (Tulip 1997).

Figure 3.6 is an example of reference cell providing calibration from GasView2 software. Red and blue curves are sample and reference signals, respectively. During acquisition, for comparison of the arrays (see after), the concentration target-gas value is given.

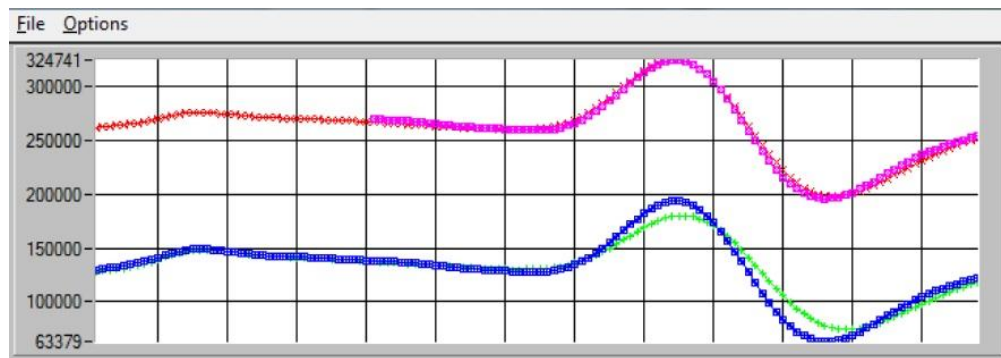


Fig. 3.6 View from GasView2 software (given by Boreal Laser inc.) during calibration provided from internal reference cell. Red and blue curves are sample and reference signals, respectively.

3.5 Field operations

The comparison between the target and the reference signals yields CO₂ column amounts (ppm·m) in the volcanic atmosphere. Column amounts are converted into average CO₂ mixing ratios (in ppmv) along the path using path lengths (see below). The accuracy of the measurement is evaluated by a correlation coefficient (R^2), which is a measure of the similarity between the waveform of the signal passing through the reference and the measured sample. In fact, an accepted mathematical procedure to compare curves or numerical arrays is the Linear Least Squares Regression analysis. This analysis results in a measure of the similarity (R^2), between the two signals (target and reference). A perfect similarity would give a value for $R^2 = 1.0$, and a total mismatch would give $R^2 = 0.0$. According to the manufacturer's datasheets, an accuracy of $\pm 2\%$ is achieved for $R^2 > 0.95$ (Trottier et al. 2009).

In the field, the GasFinder was set as to measure CO₂ mixing ratios (ppmv) at 1 Hz rate. Alignment between the laser unit and the retro-reflector mirror was optimised using a red visible aiming laser and a sighting scope.

The size of the retro-reflectors mirror was chosen as to adjust the returning light level to a desired value, depending on the path-length and the expected absorption of IR radiation. The light level is the amount of energy returned by the retro-reflector and captured by the optics inside the GasFinder. This parameter is non-dimensional and can range between 500 and 16,368. During field operations, the desired working range (where the GasFinder behaves linearly) is between 2000 and 12,000: at lower light levels (<2000) there is not sufficient radiation captured by the optics, while non-linear behaviour and/or signal "deformation" due to saturation can be attained for values >12,000. The 2000-12,000 range is also necessary to obtain adequate signal strength for optimal digitization.

Moreover, GasFinder uses the average ambient temperature and pressure readings obtained during each measurement cycle to automatically compensate for T- P-dependence of the laser-receiver unit response (using response functions calibrated in laboratory by Boreal Laser Inc., Fig. 3.7).

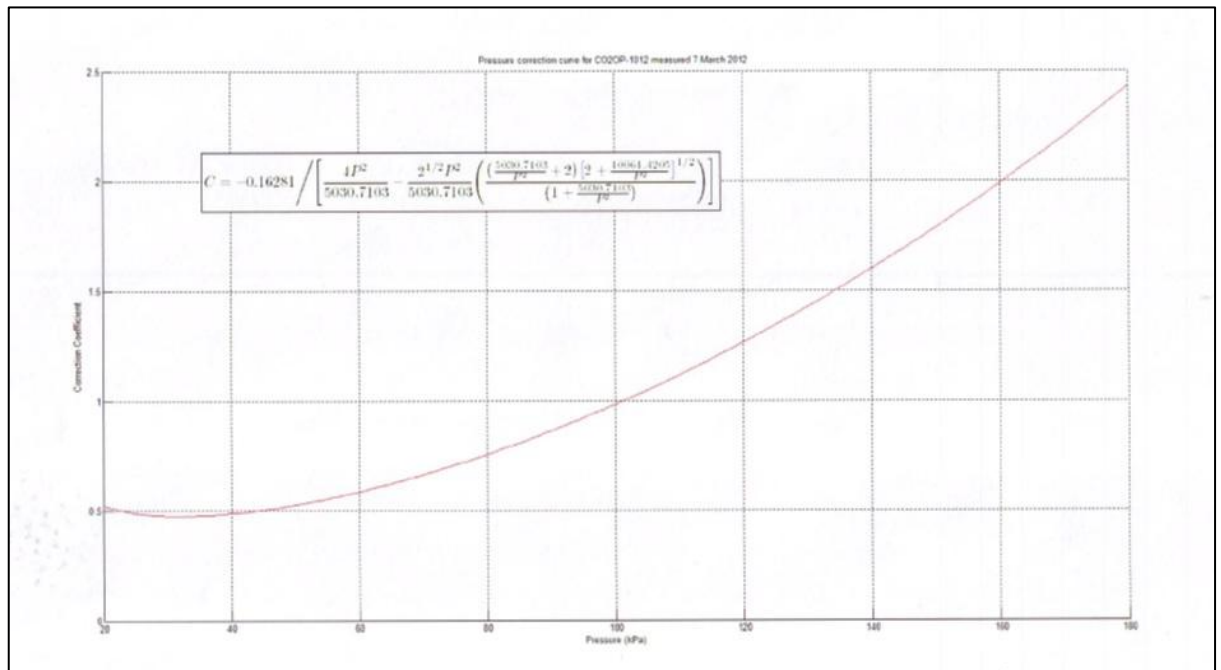


Fig. 3.7 Response functions calibrated in laboratory by Boreal Laser Inc. for pressure-compensation in the mixing ratios calculations.

Standard ambient pressure at sea level is 101.35 kPa thus the graph (Fig. 3.7) shows 1.0. Instead, at 40kPa, the graphs (Fig. 3.7) gives 0.5. Thus the instrument reads 1/0.5=2 times as much as there really is at 40kPa. Pressure-compensated reading can be manually operated (from the relation in figure 3.7), or can be automatically operated via the

GasFinder acquisition software (setting the temperature and ambient pressure in the instrument menu and having direct correction). The temperature effect is much smaller and trivial between 0° C and 35° C.

3.5.1 Geometry of field experimental set-up

For each campaign, carried out using GasFinder 2.0, an ad-hoc measurement geometry was used. At each site, the positions of retro-reflectors and the laser unit were expressed by numbers and letters, respectively.

These positions were geo-referenced with a portable GPS, and were chosen so to have the target fumaroles' plumes in between retro-reflectors and the GasFinder, allowing for complete coverage of each degassing area. During the field operations, the portable laser unit was moved along the designed positions, so to scan the fumaroles' plume from different angles and distances (aiming toward several differently positioned retro-reflectors).

Path lengths (the distance between the laser unit and each retro-reflector) were measured with an IR range finder (to approximately ± 1 m a). For short distances, a measuring tape was also used for more accurate measurements. A portable meteorological station was continuously recording (at 1 Hz) during the measurements to restrict post-processing to sampling intervals characterized by similar meteorological conditions of stable wind speed and direction.

Chapter 4

GasFinder-dataset processing

4.1 Dataset download from GasFinder

The field-acquired datasets were downloaded from the GasFinder internal memory card via a serial cable at 9600 baud rate (bits per second) and transmitted as ASCII string as shown in figure 4.1 (an example taken from the Operation Manual written by Boreal Laser Inc.). The data strings are comma-delimited (,) and an asterisk (*) signifies the string end.

Data_header,	R ² ,	light_level,	serial_number,	*check_sum.
\$GFDTA,	27.7,	98,	246.3,	5527,
	gas_concentration,	distance,	date_time,	NH3OP-1015,
				1,
				*56
data_header	header designating the type of data			String
gas_concentration	in ppm (parts per million meter)			Number
confidence_factor,R ²	between 0 and 99			Integer
distance	user-set distance to retro in metres			Number
light_level	returning light level			Integer
date_time	current date and time	YYYY/MM/DD	hh:mm:ss	
ser_number	identification number of the system			String
status_code	code giving system operating status			Integer
check_sum	checks the data stream for errors			String

Fig. 4.1 Example of an ASCII string, comma-delimited (,) and ending with an asterisk (*).

Figure 4.2 explains the status codes of the string. The above sample status code of “2800” corresponds to “0010_1000_0000_0000”. This indicates an instrument status of n_{13} – NOT_CALIB, n_{11} – MENU_MODE.

Under normal operating conditions, the most common status code is “1”. This is actually 0001, but the software ignores the leading zeros and indicates a status code of “1”. This corresponds to “0000_0000_0000_0001” and indicates an instrument status of: n_0 – NO_ERROR.

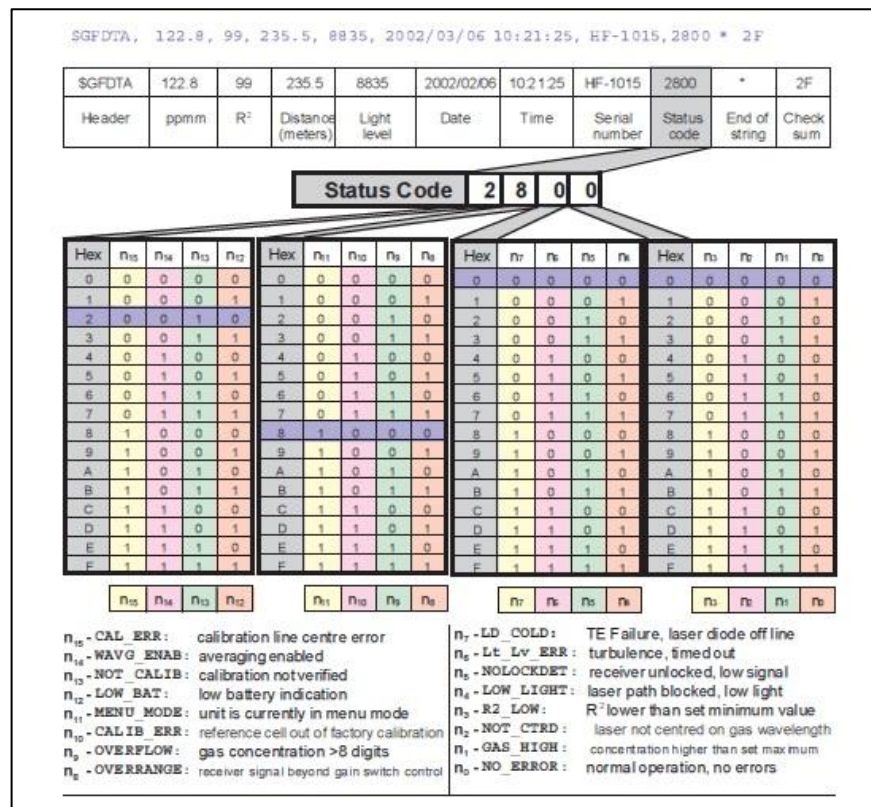


Fig. 4.2 Example of status code.

4.2 Post-processing

CO₂ mixing ratios, acquired during operation fields, were filtered to confine analysis to a sub-set of data with R² (>0.95) and light values of 4000-8000. Moreover, a portable meteorological station was continuously recording (at 1 Hz) to restrict post-processing to sampling intervals characterized by similar meteorological conditions of stable wind speed and direction.

4.3 Tomographic maps

After operation field, the initial step was to use a Matlab script, to:

- create a matrix containing information on the geometry of the experimental setup;
- obtain a 2D reconstruction of CO₂ mixing ratios in a cross-section of the atmospheric plumes, starting from the raw GasFinder dataset.

In order to start the calculations, the Matlab script was initialized with the coordinates of laser and retro-reflector positions. The additional input data was a column vector containing the mean CO₂ column amounts (in ppm·m) obtained for each GasFinder-retro-reflector path.

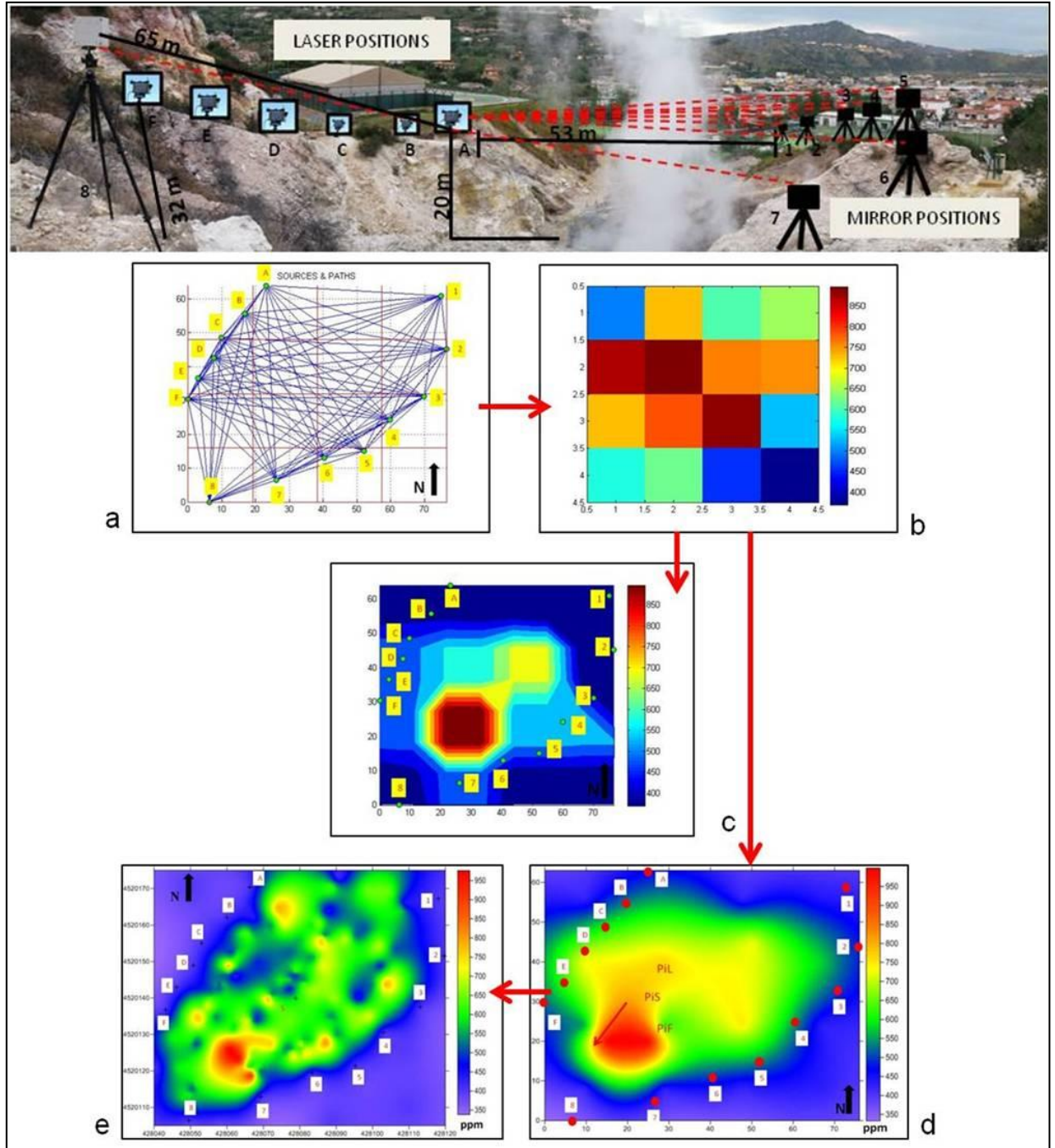


Fig. 4.3 Output of data processing routine, applied to the dataset collected at Pisciarelli site on 8th May 2013; **a** geometric matrix; **b** and **c** maps of CO₂ mixing ratios, resulting from the Matlab algorithm; **d** Matlab contour map extrapolated and displayed on Surfer software; **e** contour map of CO₂ mixing ratios, resulting from Surfer software; X-Y axes in the contour plots are distances (in metres) for the Matlab plots (c and d) and UTM positions for the Surfer contour map (e). On the top: a schematic representation of the experimental set-up geometry in the field. Positions of the laser unit and retroreflectors are given.

Figure 4.3 exemplifies the steps taken by the Matlab algorithm to image CO₂ mixing ratios in the plume in a 2D contour map (the example refers to the May 2013 campaign at Pisciarelli site, from Pedone et al. 2014a). In detail, Figure 4.3a is an example of a *geometric matrix* generated by the Matlab algorithm: this is a geometric reconstruction of the experimental set-up (GasFinder positions are indicated with letters and retro-reflectors positions are indicated with numbers). The *geometric matrix* also contains coordinates for all the possible (GasFinder-retro-reflector) paths in a 4×4 matrix (e.g., the explored space was divided into 16 equally sized cells; the red cells in Fig. 4.3a). In step b (Figure 4.3b), the scripts uses the data inversion procedure (see below) to assign an averaged CO₂ mixing ratio (in ppmv) to each cell of the 4×4 matrix (the same 16 cells of Fig 4.3a) (see colour scale for mixing ratio range): this is the so-called *tomographic matrix* (Fig. 4.3b). In step c, the *tomographic matrix* (Fig. 4.3b) is presented in visual form as the CO₂ *tomographic contour maps* of Figure 4.3c and 4.3d, which were generated by the Matlab script (which used the least squares regression technique to interpolate the mixing ratio data for each cell; note that the mixing ratio value for each cell was assigned to the cell centre during interpolation) and Surfer software (which used the Point Kriging geo-statistical method to interpolate the available data and produce an interpolated grid; Isaaks and Srivastava 1989), respectively. For comparison, an independent contour map of CO₂ mixing ratios was also realized directly with the Surfer imaging software (Fig. 4.3e). This was obtained by arbitrarily taking a number of four equally spaced points over each GasFinder retro-reflector path, and assigning the average CO₂ mixing ratio (in ppmv) for that path to each of these points (Point Kriging was again used for interpolation). The output of the Matlab (Fig. 4.3d) and Surfer (Fig. 4.3e) contouring routines yield similar results.

4.3.1 Description of the Matlab Tomographic Algorithm

The Matlab script (author, Gaetano Giudice, INGV Palermo; modified by Gaetano Giudice and Maria Pedone, DiSTeM, University of Palermo) was used to create a matrix containing the geometry of the experimental setup (*geometric matrix*, M) and obtain bi-dimensional CO₂ mixing ratio maps from path-integrated CO₂ column amounts (ppm·m).

The input of the Matlab script was a matrix of coordinates, e.g., the positions of the laser unit (Tx in the following) and of the retro-reflectors (Rx in the following), shown as letters and numbers. The additional input data was a column vector, containing the CO₂ column amounts obtained for each Tx-Rx path (vector a). The background CO₂ column amount

was assigned to the Tx-Tx and Rx-Rx paths (which were out of the plume). For each single laser beam path, the following equation holds:

$$m_0 \times c_0 = a_0 \quad (4.1)$$

Where m_0 is the path length in metres, c_0 is the mean CO₂ mixing ratio in ppmv and a_0 is the path-integrated CO₂ column amount, in ppm·m.

From this, the script calculates the CO₂ mixing ratios (ppmv) at the nodes of a regular $k \times j$ grid (covering the plan view of the measuring site), solving the matrix equation

$$M \times c = a \quad (4.2)$$

where:

$$M = \begin{matrix} & l_{11} & l_{12} & \dots & l_{1n} \\ \begin{matrix} l_{21} \\ l_{22} \\ \dots \\ l_{m1} \end{matrix} & & \begin{matrix} l_{22} \\ l_{22} \\ \dots \\ l_{m2} \end{matrix} & & \begin{matrix} \dots \\ \dots \\ \dots \\ \dots \end{matrix} \\ & l_{1n} & l_{2n} & \dots & l_{mn} \end{matrix}; \quad c = \begin{matrix} c_1 \\ c_2 \\ \dots \\ c_n \end{matrix}; \quad a = \begin{matrix} a_1 \\ a_2 \\ \dots \\ a_m \end{matrix} \quad (4.3)$$

is the matrix of the lengths, of size $m \cdot n$, where m is the number of paths and n is the number of cells in which the space domain is divided:

$$cell\ number\ (n) = \begin{matrix} 1 & 2 & 3 & 4 \\ 5 & 6 & 7 & 8 \\ 9 & 10 & 11 & 12 \\ 13 & 14 & 15 & 16 \end{matrix} \quad (4.4)$$

In both cases $n = 16$ (red cells in Fig. 4.3a). In the *geometric matrix* M , each element $M(i,j,k)$ is the portion (in metres) of the path from the i -th Tx to the j -th Rx, falling inside the k -th cell of the grid.

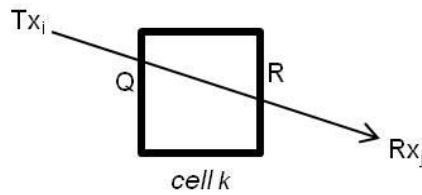


Fig. 4.4 an example of a k -th cell crossed by the Tx_i-Rx_j path; QR is the length of the path segment inside the cell.

For example, M_{p4} should be the length of the segment of the p -th ray in the path vector, i.e. from Tx_i to Rx_j inside the cell number 4 (segment in Fig. 4.4).

An example of the *geometric matrix* generated by the Matlab algorithm is given in figure 4.3a, referring to the second campaign at Pisciarelli site. Figure 4.3a is the reconstruction of the experimental geometric set-up. Tx are indicated with letters and Rx are indicated with numbers.

The tomographic problem is complex from mathematical point of view, as in the algebraic system $(m \times n)$, $m \gg n$. In the condition where cells are traversed by more than one path, this creates an over-determined problem, that has no unique solution. In addition, M is a “sparse” matrix, e.g. a matrix populated primarily with zeros (Stoer and Bulirsch 2002) as elements of the table. For the resolution of these problems, iterative algorithms to solve linear systems are typically used. In this work, the LSQR method was used, which is a method for the resolution of the least squares linear problems containing sparse matrices. The result of Least squares method is a bi-dimensional planar section of CO₂ mixing ratios (here referred as *tomographic matrix*), in which the color scales mark a different gas distribution in the investigated area (Fig 4.3).

4.3.2 Results on synthetic data

Sets of synthetic data were used to test the algorithm. These synthetic arrays of concentration data, an example of which is shown in Figure 4.5a, were created to resemble as much as possibly those found in our real application. Since M (the matrix of the lengths) and mixing ratios are both known in the synthetic samples, they can be combined to calculate the vector a (column amounts, in ppm·m). From this, the Matlab algorithm (see above) was used to convert again into model-derived mixing ratios (Fig. 4.5b). Figure 4.5c shows the resultant errors (in %), highlighting small discrepancies between synthetic reference values and mixing ratios predicted by the tomographic algorithm (Fig. 4.5a and b). Furthermore, in the construction of the vector a , a random error of about 1% of measurement was deliberately added. Thus, the maximum error inducted by the algorithm is ~3% .

4.3.3 Iterative algorithm to create a tomographic matrix for Surfer software

In figure 4.3a, Tx and Rx positions are known, allowing for straightforward calculation of the spatial coordinates of the midpoint of each cell of the grid. The *tomographic matrix* shown in Figure 4.3b is a referenced map of X , Y , C coordinates, in which C is the CO_2 mixing ratio in each cell, and X and Y are the spatial coordinates of the cell itself. This matrix was then interpolated and displayed with the Surfer software (Figure 4.3d).

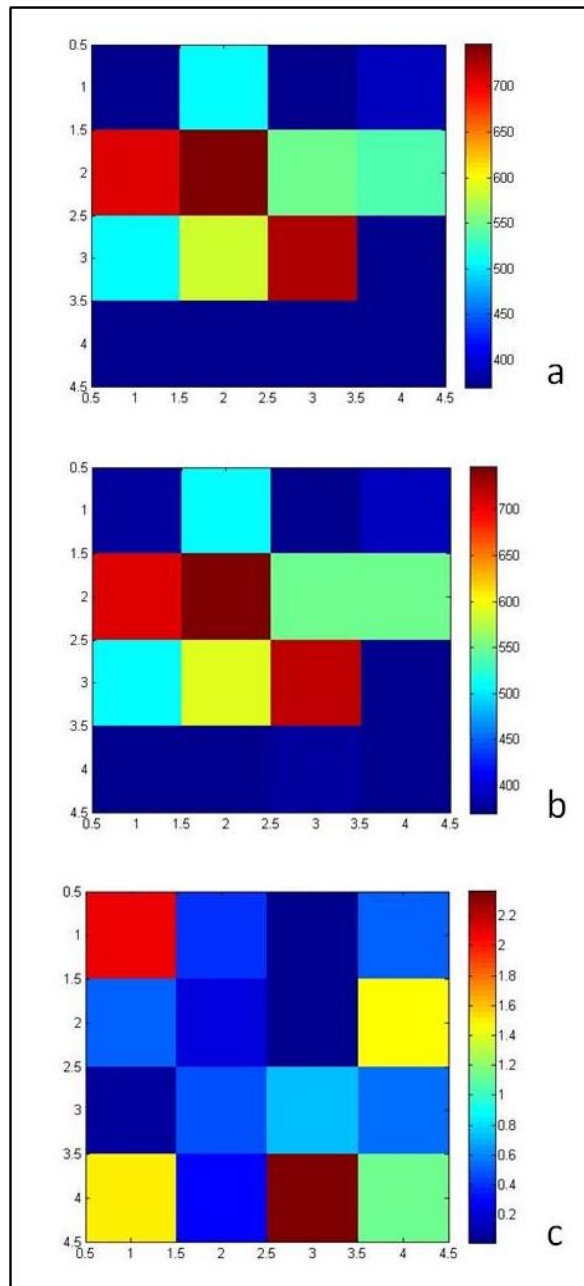


Fig. 4.5 Test of Least-squares method using synthetic data; **a** synthetic reference mixing ratio values (expressed in ppmv); **b** mixing ratio values (in ppmv) predicted by the tomographic algorithm; **c** error distribution (difference between **a** and **b**) expressed in %.

4.4 Flux estimates

In order to calculate, for each survey, the total CO₂ output from each degassing area, we integrated each set of simulated CO₂ mixing ratios (e.g., Figs 4.3 d and e) over the entire grid area, to obtain the CO₂ Integrated Column Amount (ICA) over a cross-section of the plume. This ICA, expressed in ppm·m², was first converted into mass units (kg/m), and then multiplied by the vertical plume transport speed (in m/s) to obtain the CO₂ mass flux.

Chapter 5

Study areas: descriptions, results and discussions

5.1 Campi Flegrei

Campi Flegrei (Fig. 5.1) is an active caldera located in Campania (Southern Italy; Fig. 5.1), whose complex volcanic history has involved phases of quiescence interrupted by at least two large caldera-forming eruptions (the Campanian Ignimbrite, 200 km³ of erupted rocks, 39 ka BP; and the Neapolitan Yellow Tuff, 40 km³ of erupted rocks 14.9 ka BP; Rosi et al. 1983; Orsi et al. 1996).

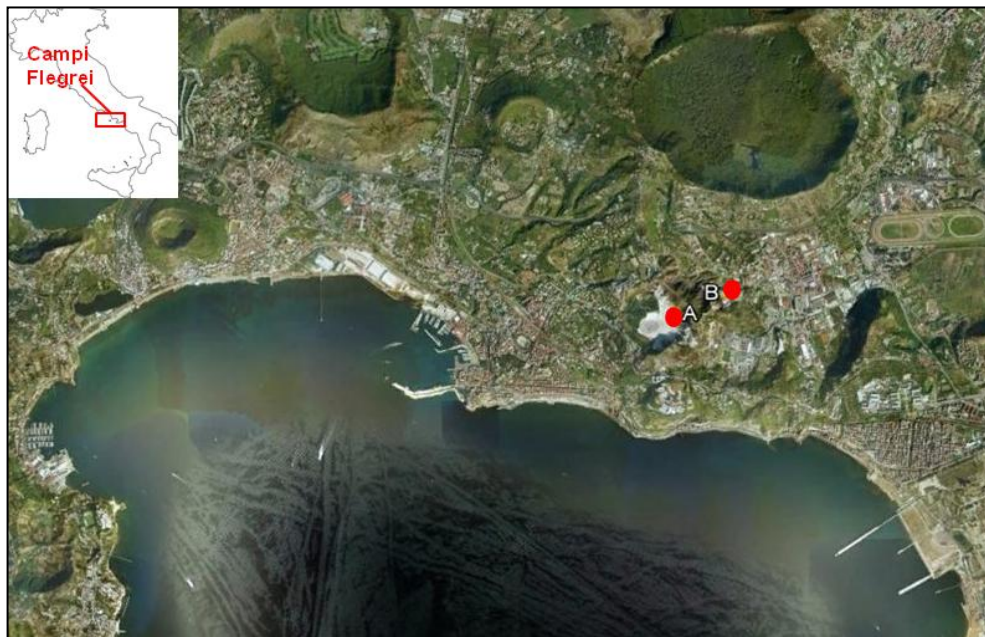


Fig 5.1 The study area: the two analysed fumarolic sites, Solfatara and Pisciarelli, are indicated as “A” and “B”, respectively.

Less voluminous explosive eruptions have occurred in the last 15 ka, concentrated into three main epochs of activity (Orsi et al. 2004; 2009) plus an isolated eruption in 1538 (the Monte Nuovo eruption). The caldera has undergone recurrent periods of unrest (Chiodini et al. 2012), including at least three seismic and ground deformation episodes (referred as

“bradyseismic crises”) in the last 30 years (Del Gaudio et al. 2010). While a magma ascent trigger for such crises has been invoked by several authors (e.g., Trasatti et al. 2011 and references cited), recent work (e.g., Bonafede and Mazzanti 1998; Chiodini et al. 2003) has also emphasised the role of fluid pressure increase due to injection of magmatic fluids into the hydrothermal system.

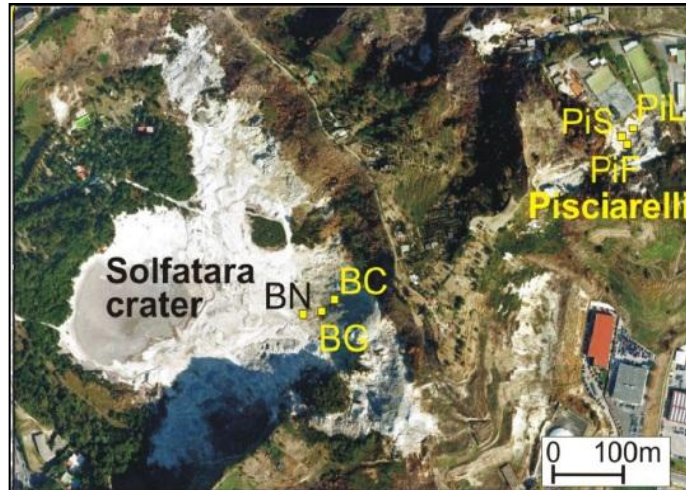


Fig. 5.2 A detail of positions of the main fumarolic vents at Solfatara crater and Pisciarelli fault. BN: Bocca Nuova; BG: Bocca Grande; BC: a vent opened in 2008; PiL: mud pool with bubbling gas; PiS: jet-like main degassing vent; PiF: smaller fumarolic fields.

The most evident surface hydrothermal manifestation on Campi Flegrei is the fumarolic field of Solfatara, a tuff-cone located near Pozzuoli and formed between 3.8 and 4.1 ka (Di Vito et al. 1999). The Solfatara crater (“A” in Fig. 5.1) hosts a large diffuse degassing structure (DDS) (Chiodini et al. 2001; 2010), sustaining a total CO₂ output of $\sim 1100 \pm 120$ Mg/day (Chiodini et al. 2010). Bocca Grande (BG) and Bocca Nuova (BN) fumaroles are the two most persistent higher-temperature ($T \sim 160^\circ\text{C}$) degassing vents in the area (Chiodini et al. 2012) (Fig. 5.2). Extensive degassing also occurs in the nearby area of Pisciarelli, a fault-related fumarolic field located a few hundred metres east of Solfatara (Chiodini et al. 2010). During our study, degassing at Pisciarelli was mainly sustained by: a vigorous jet-like degassing vent ($T \sim 105^\circ\text{C}$), currently the main active gas source at this site (PiS in Fig. 5.2); a mud pool with vigorous gas bubbling (PiL in Fig. 5.2); and a small active fumarolic field in the southern part of the area (PiF in Fig. 5.2).

The CO₂ output sustained by the fumarolic fields of Solfatara and Pisciarelli has long remained undetermined: since SO₂ is typically absent in the fumaroles, standard ultraviolet sensing techniques (e.g., Oppenheimer 2010) cannot be applied to derive the gas output.

Very recently, Aiuppa et al. (2013) reported on the first Multi-GAS-based estimate of the CO₂ output, which was evaluated at $\sim 460 \pm 160$ Mg/day.

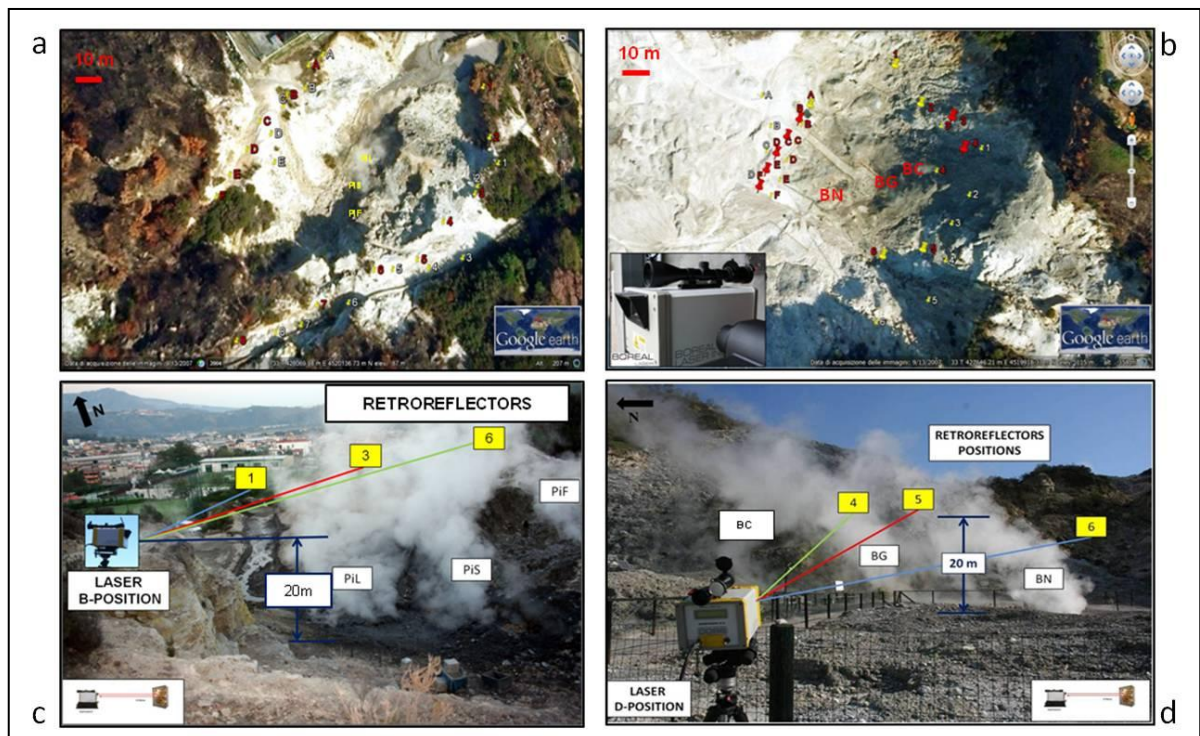


Fig. 5.3 **a-b** Position of retro-reflector units (numbers) and of the GasFinder unit (letters) at Pisciarelli site and Solfatara crater; White colour: October campaign; Red: January and May campaigns; **c** Example of acquisition over open-path laser (B position) and retro-reflectors (1-3-6); PiL: mud pool with bubbling gas; PiS: jet-like main degassing vent; PiF: smaller fumarolic fields; **d** Example of acquisition over open-path laser (D position) and retro-reflectors (4-5-6); BG: Bocca Grande; BN: Bocca Nuova; BC: new degassing vent (opened in 2008).

Figure 5.3 (a and b) shows the positions of retro-reflectors (numbers) and of the GasFinder unit (letters) during the three field campaigns at, respectively, Pisciarelli (B in Fig. 5.1) and Solfatara (A in Fig. 5.1) in October 2012, January 2013 and May 2013. These positions were geo-referenced with a portable GPS, and were chosen so to have the target fumaroles' plumes in between retro-reflectors and the GasFinder, and to allow for complete coverage of the degassing area. The degassing vents at Pisciarelli site (shown in Fig. 5.2) are found at the bottom of a narrow valley, at the outer rims of which the retro-reflectors and GasFinder were positioned. In such conditions, the laser-paths (from the GasFinder unit to each retro-reflector) intercepted the fumaroles' atmospheric plumes at ~ 20 m height, as shown in Fig. 5.3c. At Solfatara, observations were focused on a 8100 m^2 area, intercepting the atmospheric plumes of Bocca Grande (BG) and Bocca Nuova (BN) fumaroles (Fig. 5.3b). The BC degassing vent of Aiuppa et al. (2013) was also covered by our measurements (Fig. 5.3b). Path lengths were measured with an IR range finder (to

approximately ± 1 m a), and ranged 32-81 m at Pisciarelli and 49-136 m at Solfatara. For short distances, a measuring tape was also used for more accurate measurements. A portable meteorological station was continuously recording (at 1 Hz) during the measurements to restrict post-processing to sampling intervals characterized by similar meteorological conditions of stable wind speed and direction. We additionally measured ambient pressure and temperature by using a co-exposed Multi-GAS (Aiuppa et al. 2013); the GasFinder uses the average readings obtained during each measurement cycle to automatically compensate for T- P-dependence of the laser-receiver unit response (using response functions calibrated in laboratory by Boreal laser).

5.1.1 Results and Discussion

The GasFinder operated for more than 17 hours during the three field campaigns (five in October 2012, six in January and six in May 2013). Measuring at 1 Hz, the GasFinder therefore provided more than 20,000 readings of path-integrated CO₂ abundances. However we focus here onto a subset of data (9127 readings), extracted from the original dataset based on data quality criteria (readings characterized by R² value >0.96 and optimal light values – between 4000 and 8000 – were selected) and meteorological conditions, and during which the plume was not condensing. In particular, we extracted only those GasFinder readings obtained during phases of stable wind direction and speed. West-southwest trending winds prevailed during the three campaigns at Pisciarelli, while east-northeast wind direction was most common at Solfatara.

During operations, the GasFinder was left to acquire along each single GasFinder – retro-reflector path (e.g., B-1 in Fig. 5.3) for ~5 min, before being rotated to measure along the successive path (e.g., B-2). With this set-up, the whole measurement grid (e.g., the total number of possible Gas-Finder – retro-reflector paths) was covered in approximately 3 hours.

Detailed datasets and mixing ratios presentation are available in (Pedone et al. 2014) and in the Supplementary Materials.

Examples of GasFinder-derived CO₂ time-series are shown in figures 5.4 and 5.5. In each plot, each curve represents a 1 min record of CO₂ mixing ratios taken along a specific GasFinder-retro-reflector path. As expected, the highest CO₂ mixing ratios (>1000 ppmv)

were observed in GasFinder-retro-reflector paths crossing the near-vent fumarolic plumes (e.g., B-6 and D-4 in Figs 5.3a and 5.3b, respectively).

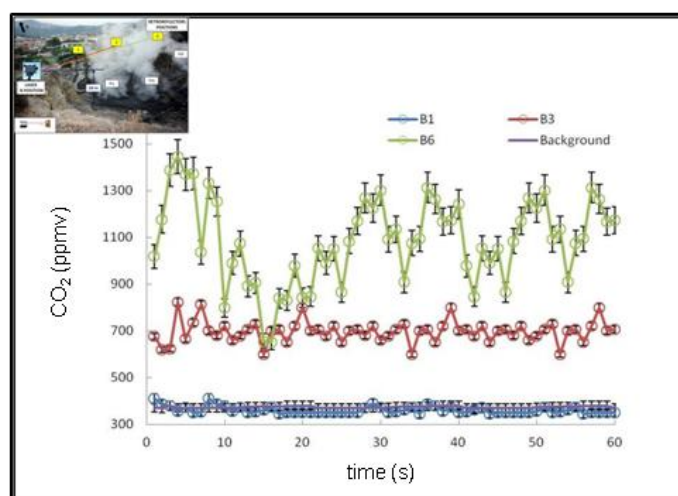


Fig. 5.4 Example of time-series of CO₂ mixing ratios (one minute data acquisition) at Pisciarelli obtained over three different categories of open paths: (i) near-vent plumes (B6); distal (aged) plumes (B3); plume margins (B1).

The peak mixing ratio of 1444 ppmv was obtained in path B-6 (see Fig 5.4). In all these near-vent path time-series, significant fluctuations of CO₂ mixing ratios were observed, with cycles of CO₂ increase-decrease typically lasting tens of seconds, and reflecting changes in plume density (because of fluctuations in gas emission rate at the fumaroles, or, more likely, due to changes in plume transport speed/direction). Lower (e.g., 600-700 ppmv), more stable, CO₂ mixing ratios were typically observed farther from the degassing vents, where more aged (diluted) plumes were intercepted by the GasFinder-retro-reflector paths (e.g., B-3 and D-5 in Figs. 5.4 and 5.5, respectively); while near-to background CO₂ mixing ratios (~400 ppmv) were typically detected at the plume' margins (e.g., B1 and D6). Background readings, respectively of ~380-390 ppmv at Pisciarelli and >400 ppmv at Solfatara (see Figs. 5.4 and 5.5), were obtained in each of the measurement day/site by pointing the laser beam toward a mirror, positioned upwind of the fumarolic area.

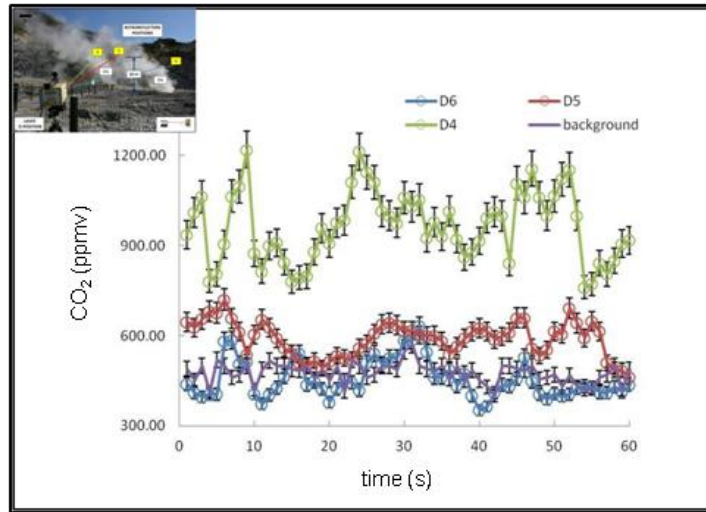


Fig. 5.5 Example of time-series of CO₂ mixing ratios (one minute data acquisition) at Solfatara obtained over three different categories of open paths: (i) near-vent plumes (D4); distal (aged) plumes (D5); plume margins (D6).

Figures 5.6 and 5.7 compare the CO₂ contour maps obtained for the three different campaigns at the Pisciarelli site (25th October 2012, 29th January 2013, and 8th May 2013) and Solfatara crater (26th October 2012, 30th January 2013, and 9th May 2013). As shown in figure 5.6, there are some remarkably similar features in the three maps, including (i) low CO₂ mixing ratio (≤ 390 ppmv) at the margins of the fumarolic area; (ii) higher CO₂ mixing ratios (from 700 to ~950 ppmv) in the central portion of the gas emission zone; (iii) peak CO₂ mixing ratios south-west the principal gas vent (marked as “PiS”), reflecting the principal direction of plume dispersal (red arrows in Fig. 5.6). Similar results have also been obtained at Solfatara (Fig. 5.7). In this area, the background CO₂ mixing ratio is higher (>400 ppmv) than at Pisciarelli, likely reflecting diffuse CO₂ outgassing from the soils (Chiodini et al. 2001; 2010). The highest CO₂ mixing ratios (up to ~950 ppmv) are consistently detected in the central part of the three maps, downwind from the BN, BG and BC fumarolic vents (the principal direction of plume dispersal is indicated by red arrows in Fig. 5.7).

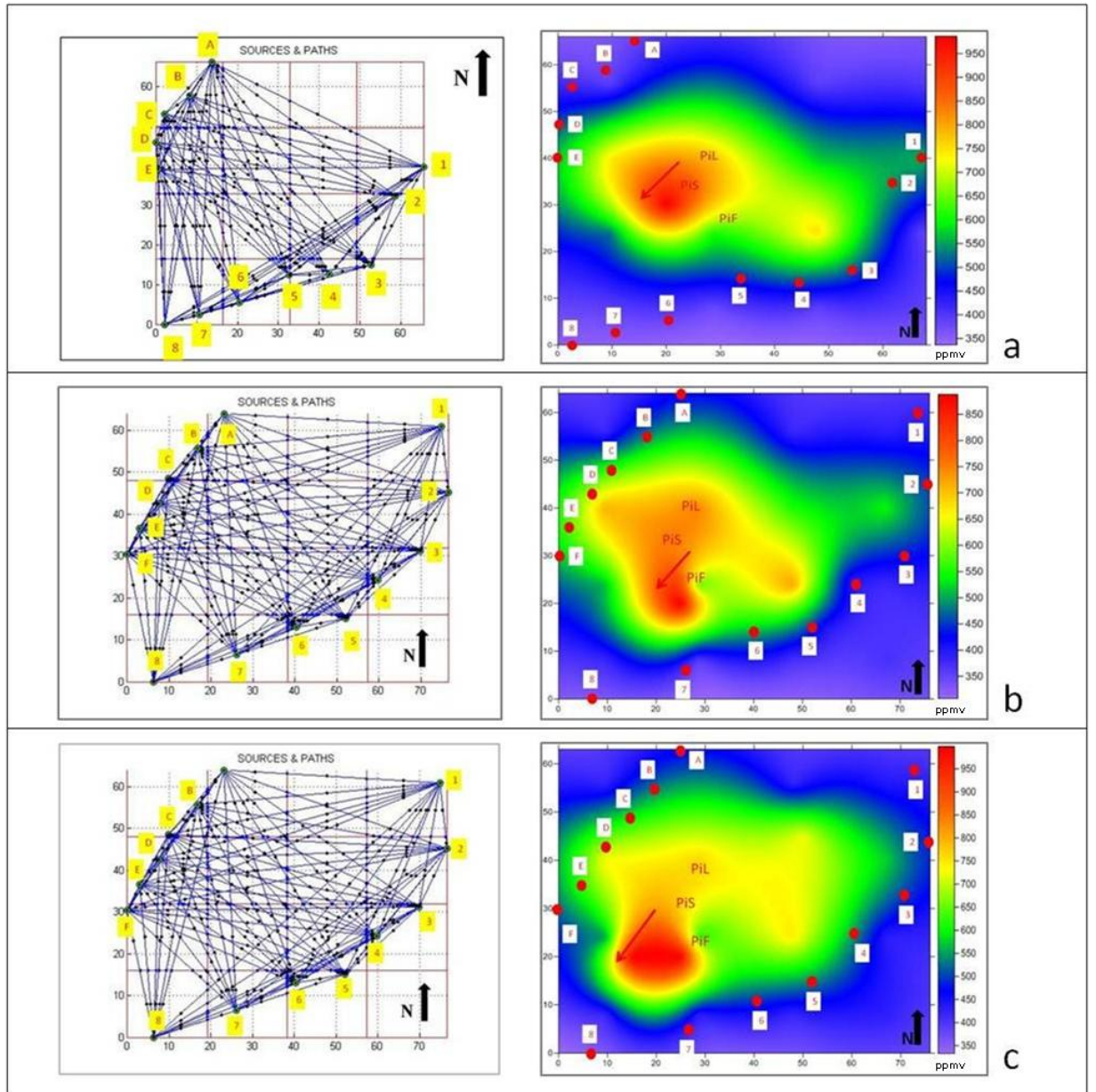


Fig. 5.6 Matlab-derived geometry and Surfer-derived CO₂ contour maps obtained for the three different campaigns at Pisciarelli site; **a** 25th October 2012; **b** 29th January 2013; **c** 8th May 2013; PiL, PiS and PiF: main degassing vents positions; red arrows: principal directions of plume dispersal.

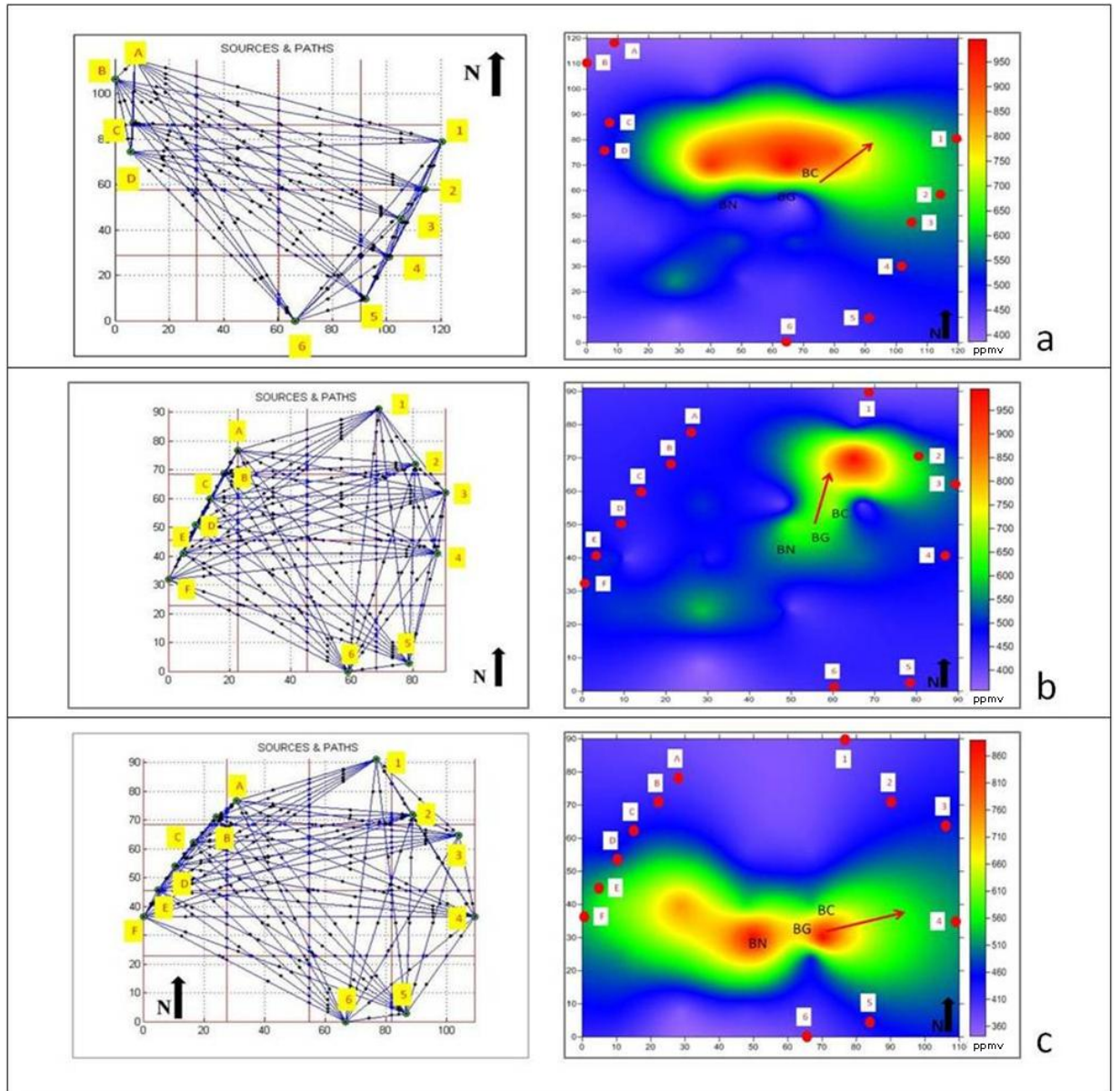


Fig. 5.7 Matlab-derived geometry and Surfer-derived CO₂ contour maps obtained for the three different campaigns at Solfatara site; **a** 26th October 2012; **b** 30th January 2013; **c** 9th May 2013; BG, BN and BC: main fumarolic vents positions; red arrows: principal directions of plume dispersal.

Occasionally (e.g., on 31st January 2013), some more detailed mapping was carried out by using a dense network of retro-reflectors in the vicinity of fumaroles BN, BG and BC. These identified the three main degassing areas with higher precision and spatial resolution (see the peak CO₂ mixing ratios of up to 950 ppmv in Figure 5.8, all located in correspondence to the principal fumarolic vents).

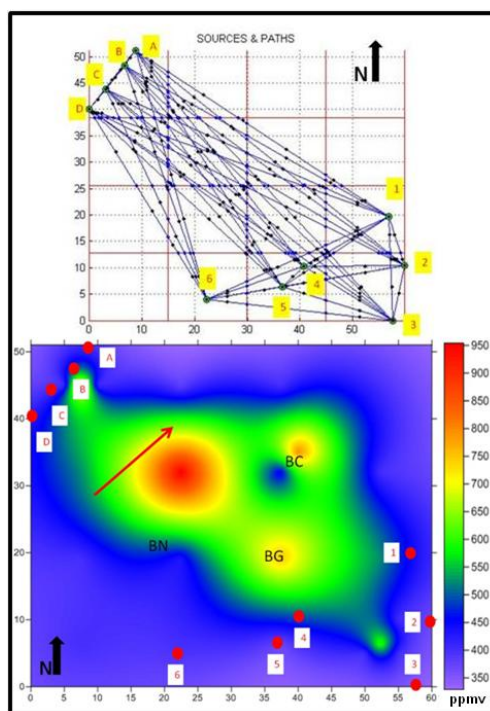


Fig. 5.8 Solfatara, 31st January 2013. Detail of three major fumarolic emissions: Bocca Grande (BG), Bocca Nuova (BN) and BC site; red arrow: principal direction of plume dispersal.

The calculated CO₂ fluxes are listed, for each site and campaign, in Table 5.1. For each campaign, there is close agreement (~ 5% difference) between CO₂ fluxes calculated from integration of either Matlab or Surfer contour maps (Tab. 1). For example, in October 2012 we estimated the CO₂ flux from Pisciarelli between 171 Mg/d (Surfer) and 182 Mg/d (Matlab). These results match closely the CO₂ output independently evaluated (by using the MultiGAS) by Aiuppa et al. (2013) for Pisciarelli in October 2012 (177 Mg/d). The increase in CO₂ output reported by Aiuppa et al. (2013) in January 2013 (up to 307 Mg/d) is not matched by a comparable increase in the GasFinder dataset (the CO₂ output – 181-195 Mg/d, Table 5.1 – is only <10% higher in January compared with other campaigns). The presence of a strong (several metres high) liquid water jet at PiS in January and May 2013 might have hampered laser observations in the core of the plume (where strong signal attenuation was observed).

The total CO₂ output from Solfatara is evaluated at ~300 Mg/day in the three campaigns (Tab. 1). This is somewhat higher than the CO₂ output reported by Aiuppa et al. (2013) (176-251 Mg/d), who however investigated a more restricted area (251 m² compared with 8100 m² here). When (on 31st January 2013) the GasFinder measurements were confined in the same restricted area (BN, BG and BC) studied by Aiuppa et al. (2013) (Fig. 5.6), a much lower CO₂ flux (120 Mg/d) was consistently obtained.

Finally, combining Pisciarelli + Solfatara datasets, a total CO₂ output of ~500 Mg/d (range, 461-507 Mg/d) were estimated for Campi Flegrei area, which agrees well with an independent evaluation of about 460 Mg/d recently made by Aiuppa et al. (2013).

The fumarolic CO₂ output, estimated here and in Aiuppa et al. (2013), is an additional contribution to the soil CO₂ output from Campi Flegrei. This latter has repeatedly been evaluated by soil surveys with the accumulation chamber method, which typically covered a large degassing structure around the fumarolised areas, but not the fumaroles themselves (Chiodini et al. 2010). For comparison, such diffuse soil CO₂ emissions ranged from 1400 (May 2013) to 1520 (October 2012 and January 2013) Mg/day (Cardellini C. pers. comm.) during our study period, somewhat above the time-average of ~1100±120 Mg/day (Chiodini et al. 2010).

Moreover, this flux value confirmed a significant contribution of fumaroles to the total CO₂ budget of the area. The fumarolic CO₂ flux from Campi Flegrei (~500 Mg/day) is substantial, and comparable to the total CO₂ flux (~453 Mg/day) over the summit area of La Fossa cone (Vulcano island) (Inguaggiato et al. 2012). It also represents an additional ~30-35% to the Campi Flegrei total soil CO₂ output of ~1480±70 Mg/day (October 2012-May 2013), leading to a combined (soil+fumarole) CO₂ output of ~2000 Mg/day.

Table 5.1 CO₂ flux estimates at the study area in October 2012, January and May 2013 using two different methods: Surfer software and Matlab algorithm. The CO₂ flux values are expressed in Mg/d. The wind speed (in m/s) at each site is given.

Period	wind speed^a	wind speed^b	CO₂ Flux	CO₂ Flux	Total CO₂ Flux
	(m/s)	(m/s)	Pisciarelli	Solfatara	(Mg/d)
October	1.4	1.0	171 ^c (182 ^d)	306 ^c (325 ^d)	477 ^c (507 ^d)
January	1.5	1.3	181 ^c (192 ^d)	316 ^c (301 ^d)	497 ^c (493 ^d)
May	1.4	1.4	175 ^c (173 ^d)	314 ^c (288 ^d)	489 ^c (461 ^d)

^a Measured at Pisciarelli site

^b Measured at Solfatara site

^c Calculated flux values using Surfer software

^d Calculated flux values using Matlab algorithm

5.1.2 Results from 2014 campaigns

Figure 5.9a compares the CO₂ emissions at Pisciarelli and Solfatara measured during the 2012-13 campaigns with more recent results obtained on 10-11 February and 23-24 October 2014. In detail, the CO₂ flux values decreased at both sites in February 2014, followed by a sharp increase in October (particularly evident at Pisciarelli, where the CO₂ fluxes peaked at ~560 t/d). It is worth noting that this increase in degassing has occurred in concomitance with a phase of resumed ground uplift and (weak) seismicity at Campi Flegrei. Actually, a few low magnitude earthquakes have recently been recorded at Campi Flegrei (the maximum magnitude = 0.5, on 25 October at 19:29:29). Most of these events concentrated in a small earthquake swarm occurred on 25 October, between 19:27 and 19:32 UT (data from “Bollettino di sorveglianza settimanale” of 28-10-2014, by INGV-OV, “Osservatorio Vesuviano – sezione di Napoli”); five of these shallow seismic events, located by INGV-OV, were characterised by hypocenters depths <2 km (red dots in Fig. 5.9b). Moreover, ground uplift also intensified in the same period, as shown in the time-series of ground level variations recorded by the GPS “Rite” Station in Pozzuoli (Fig. 5.9c).

Finally, combining Pisciarelli + Solfatara datasets, a total CO₂ output of ~1000 t/d (twice as much as measured in October 2012 to May 2013) was estimated for Campi Flegrei in October 2014 (Fig. 5.9a). This result agrees well with an independent CO₂ flux value of

~1200 t/d evaluated by using the MultiGAS technique during the same campaigns (unpublished data).

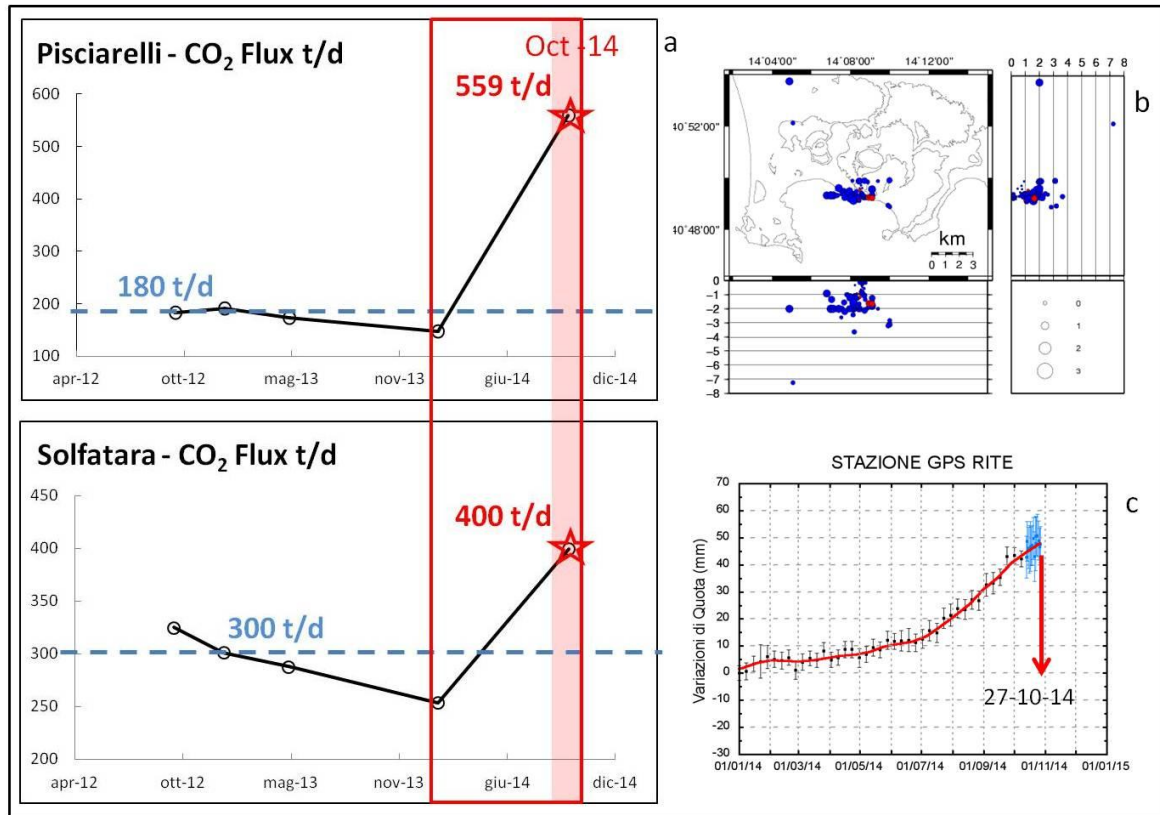


Fig 5.9 Recent measurements and results. **a** Variation of CO₂ emissions at Pisciarelli and Solfatara t (by using the TDLS), including the recent measurements of 10-11 February and 23-24 October 2014. **b** Hypocenters of earthquakes located at Campi Flegrei in the last 12 months (in total 77). In red: events occurred in the week before 25 October 2014 (in total 5). **c** Time series of soil level variations recorded by the RITE station (in Pozzuoli) from 1 January to 27 October 2014. **a** and **b** taken by "Bollettino settimanale" of 28 October 2014 (available on-line) edited by INGV-OV, Naples.

5.2 Nea Kameni volcano (Santorini)

Santorini is located in the Aegean Sea, and is part of the Cyclades archipelago. Santorini is 75.8 km² and it is a complex of five islands known as Thera, Therasia, Aspronisi, Palea Kameni and Nea Kameni, from the active intra-caldera volcanic field (Dominey-Howes et al. 2004). Volcanic activity began approximately 3-4 million years ago and the caldera is a composite structure resulting from several collapses (Druitt et al. 1999). Santorini has been the focus of significant volcanological research because its 3500 BP paroxysmal explosive eruption that buried the ancient town of Akrotiri (Bond and Sparks 1976) and possibly impacted the Minoan civilization (Marinatos 1939; McCoy and Heiken 2000). The outer islands of Thera, Therasia and Aspronisi are composed of rocks that predate the Late Bronze Age (LBA) or Late Minoan (LM) eruption of 3500 BP. Palea and Nea Kameni are composed of dacitic lavas that post-date the LBA eruption and outcrop at the centre of the caldera (which bottom reaches the depth of 390 m below sea level). After the Minoan eruption, volcanic activity was to a major degree concentrated in the central part of the caldera complex (Fyticas et al. 1990). This activity produced lava domes, flows and pyroclasts that built up Palea and Nea Kameni islet between 197 BC and 1950 AD (Stiros et al. 2010). In the 20th century, four periods of unrest led to small-scale eruptions in 1925-1926, 1928, 1939-1941 and in 1950 (Fyticas et al. 1990; ISMOSAV, 2009). Outside the caldera, volcanic activity was recorded only once, in 1649-1650 AD, in the Columbo submarine volcano, characterized by an up to 4 km long underwater caldera, 18-512 m below sea level (Vougioukalakis et al. 1994). Since the last eruption in 1950, Santorini volcano has been relatively quiescent (Tsapanos et al. 1994; Papazakos et al. 2005; ISMOSAV, 2009). The most important evidence of the presence of magma at depth are gases (fumaroles, mostly CO₂, vapour and air, 93-97 °C) in Nea Kameni and also small magnitude earthquakes especially at the Columbo volcanic centre offshore (Dimitriadis et al. 2009). Recent seismotectonic and tectonovolcanic activities in the Santorini area seems to be related with the Columbo line i.e. a lineament or zone containing the Columbo volcano, a morphological/structural discontinuity in Thera and the majority of hot springs identified in the caldera (Pavlidis and Valkaniotis 2003; Sigurdsson et al. 2006).

In early 2011, geodetic monitoring revealed new stage of caldera-wide uplift (Newman et al. 2012; Parks et al. 2012), accompanied by swarms of shallow earthquakes. This unrest lasted from January 2011 to April 2012 (Parks et al. 2013). Degassing activity at Santorini is currently concentrated in a small, hydrothermally altered area on top of Nea Kameni islet (Parks et al. 2013), where a number of weakly fuming fumaroles (mostly CO₂, water

vapour and air-derived gases; temperatures of 93–97° C) are concentrated (Tassi et al. 2013). A recent survey carried by Parks et al. (2013) indicated increased diffuse CO₂ emissions between September 2010 and January 2012; this period was characterized by a change in the degassing pattern, with an increase in soil CO₂ emissions peaking at 38 ± 6 t/d in January 2012 (Parks et al. 2013). Tassi et al. (2013) examined the response of fumarole composition to the 2011–2012 unrest, and reported increasing CO₂ concentrations (and decreasing $\delta^{13}\text{C-CO}_2$) from May 2011 to February 2012, suggesting mantle CO₂ contribution. The summit fumarolic field was the site of our 9 April 2013 survey (Fig. 5.10).

5.2.1 Results and Discussions

The GasFinder 2.0 operated for more than 4 hours at the top of Nea Kameni volcano (Fig. 5.10) on 9th April 2013. We concentrate here onto a subset of data (1,070 readings) extracted from the original dataset based on data quality criteria (R^2 value >0.95 and optimal light values were selected) and meteorological conditions (northern trending wind prevailed during the field campaign).

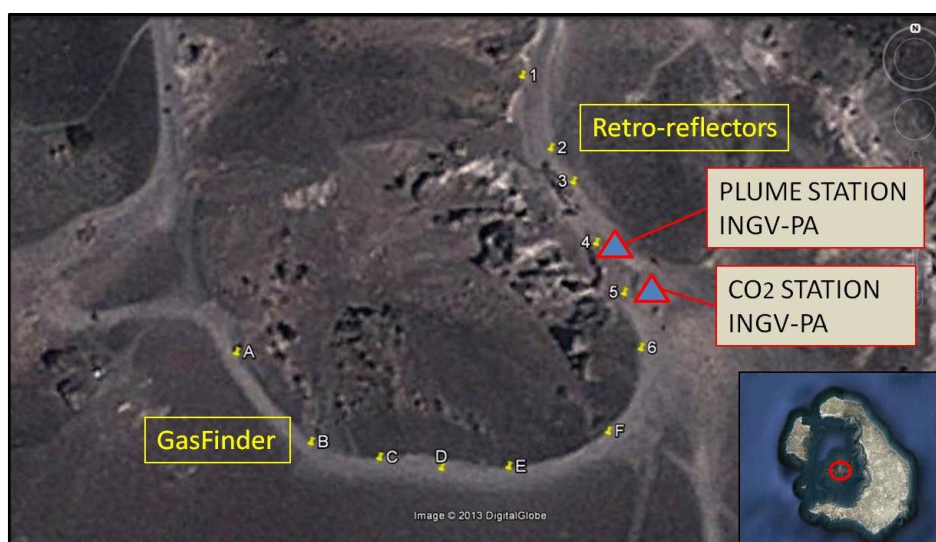


Fig. 5.10 Nea Kameni summit crater (Santorini island, Greece). The positions of GasFinder and retro-reflectors are shown with letters and numbers, respectively. The positions of MultiGAS stations (blue triangles) are also given.

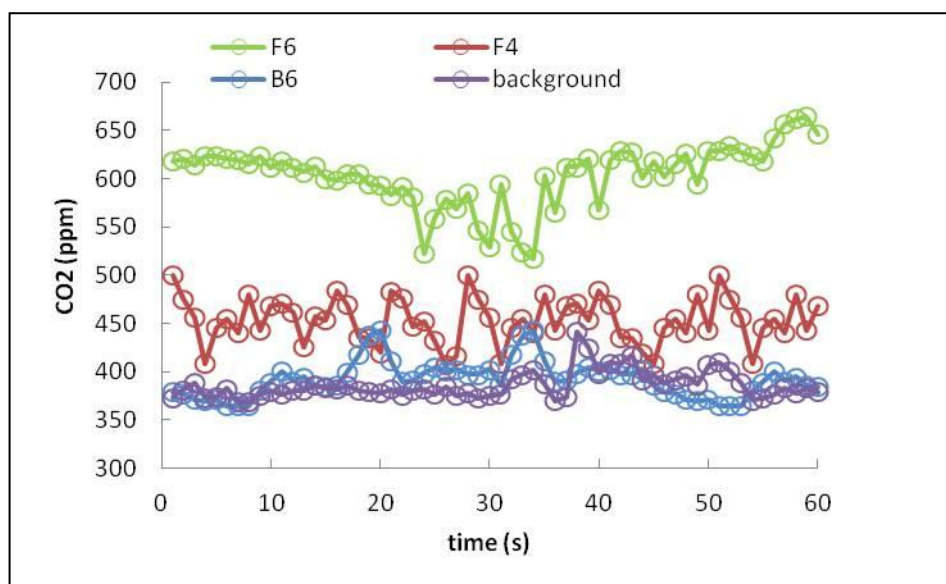


Fig. 5.11 Example of time-series of CO₂ mixing ratios (one minute data acquisition) at Nea Kameni summit crater obtained over three different categories of open paths: (i) near-vent plumes (F6); distal (aged) plumes (F4); plume margins (B6). Background values are also given.

Fig. 5.11 is an example of time-series of CO₂ mixing ratios (one minute data acquisition) at Nea Kameni summit crater obtained over three different categories of open paths: (i) near-vent plumes (F6); distal (aged) plumes (F4); and plume margins (B6).

Fig. 5.12 shows the Matlab-derived contour map of CO₂ concentration obtained for the campaign at Nea Kameni fumarolic field.

This map shows the distribution of CO₂ concentrations in a roughly horizontal cross-section of the plume located near eastern internal rim of summit crater (~1 m under INGV-Palermo plume station). Low CO₂ concentration (between 340 and 390 ppm) are observed at the margins of the fumarolic area; while higher CO₂ concentrations (range, from 540 to ~590 ppm) are seen in the gas emission zone; a peak CO₂ concentration is located in correspondence of one principal gas vent (marked as “Fum6” in Fig. 5.12). From integration of data in the contour map of Figure 5.12, a CO₂ output from Nea Kameni fumaroles of 63 ± 22 tons/day was estimated. This fumarolic output is ~4 times higher than the total diffuse discharge from the soils of 15.4 tons/day reported by Chiodini et al. (1998), and ~1.5 times higher than the soil CO₂ output of 38 ± 6 tons/day estimated (in January 2012) by Parks et al. (2013). The weak but persistent fumarolic activity on-top of Nea Kameni is the major emission source of CO₂ at this volcano.

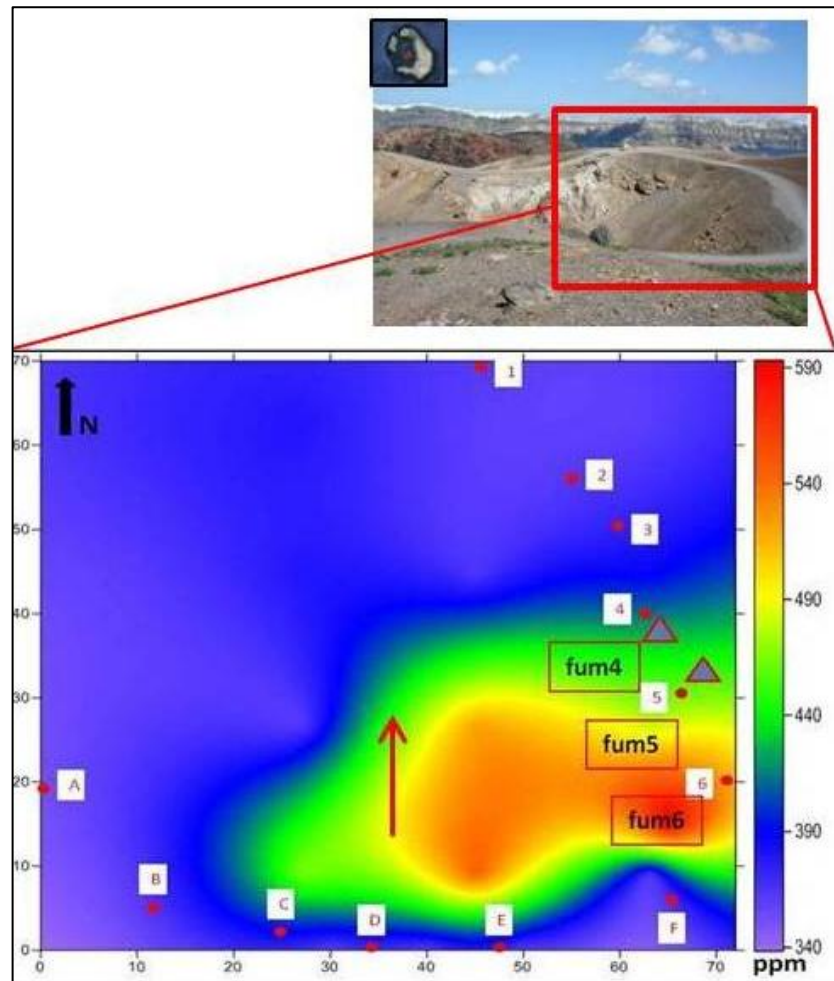


Fig. 5.12 CO₂ mixing ratios (ppm) contour map. GasFinder and retro-reflectors positions are shown with letters and numbers respectively. “Fum4”, “Fum5” and “Fum6”: positions of main degassing vents; blue triangles: permanent INGV-PA stations; red arrow: principal direction of plume dispersal. See text.

5.3 Hekla summit crater (Iceland)

Hekla is one of the most active volcanoes in Europe and its historical volcanic activity, petrology, and geochemistry have been the subject of several studies (e.g. Thorarinsson 1967; Sigmarsson 1992). Hekla volcano (63.98°N , 19.70°W ; 1490 m a.s.l) is located in the southern part of Iceland at the intersection of the South Iceland Fracture Zone and the Eastern Volcanic Zone (Moune et al. 2007). In its volcanic history, Hekla system has produced a suite of basalt, basaltic andesite, andesite, dacite and rhyolite magmas that belong to the transitional alkalic series (Jakobsson 1979). All historical eruptions of Hekla have started with a highly explosive sub-Plinian to Plinian phase that normally is followed by a longer-lasting phase of effusive activity (Thorarinsson 1967).

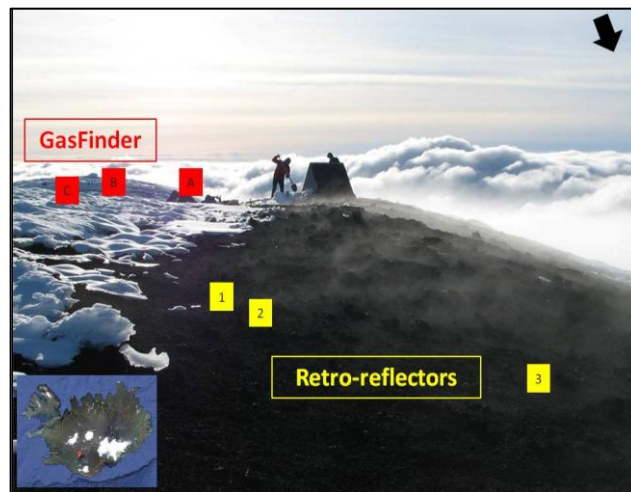


Fig. 5.13 Hekla summit (Iceland). The positions of GasFinder and retro-reflectors are shown with letters and numbers, respectively.

In recent decades, Hekla has erupted frequently, at an average rate of one eruption per decade, and most recently in 2000 (from 26 February to 8 March) (Höskuldsson et al. 2007). Gas information has long remained missing, because Hekla appears to be only degassing during eruptions. Very recently, Ilyinskaya et al. (2014) identified a weakly degassing, warm ground on the summit of the Hekla 1980-81 crater (Fig. 5.13), and studied the composition of this gas using data from a permanent Multi-GAS instrument, installed by INGV-PA (Istituto Nazionale di Geofisica e Vulcanologia, Sezione di Palermo) and IMO (Icelandic Meteorological Office) in 2012, and field campaigns using an accumulation chamber. These authors provided evidences for this gas spot being the

only current surface manifestation at Hekla. This degassing field was therefore the site of our measurement survey with the TDL on 2nd July 2013 (Fig. 5.13).

5.3.1 Results and Discussions

The GasFinder 2.0 operated for more than 4 1 hour for Hekla on 2nd July 2013 (Fig. 5.13); concentrating here onto a subset of data (985 readings) extracted from the original dataset based on data quality criteria and meteorological conditions (southern trending wind).

An example of acquisition in three different paths are given in figure 5.14.

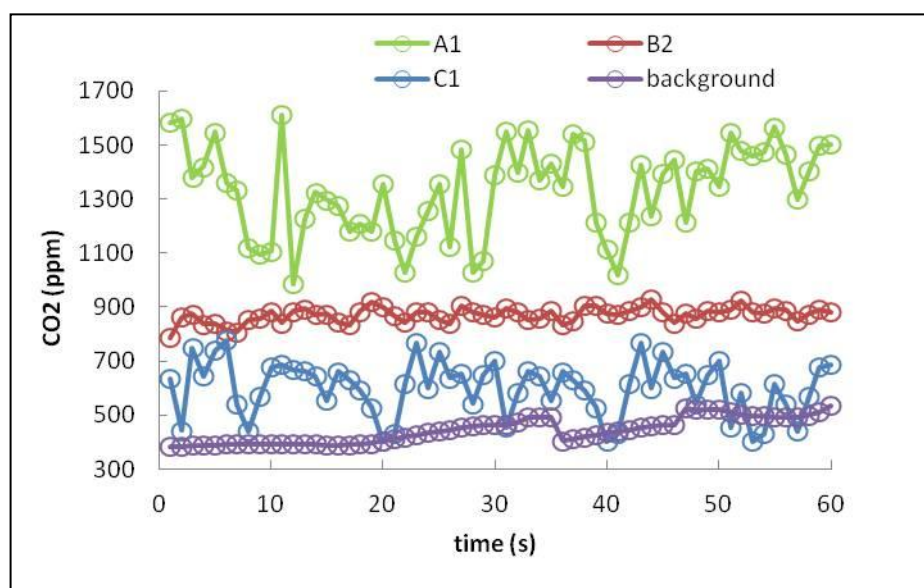


Fig. 5.14 Example of time-series of CO₂ mixing ratios (one minute data acquisition) at Hekla crater obtained over three different categories of open paths: (i) near-vent plumes (A1); distal (aged) plumes (B2); plume margins (C1). Background values are also given.

Figure 5.15 is a map of CO₂ concentrations measured in air ~1 m above the degassing ground of Hekla. In this area, the background concentration of CO₂ are ~400 ppm; while the highest CO₂ concentration values (up to ~1000 ppm) are consistently detected in the central part of the map, near the INGV-IMO plume station, where outgassing from the soil is most marked.

Given the positioning of Gas Finder and retro-reflectors, the Matlab-derived contour map is here relative to an hypothetical horizontal cross-section, taken at about 1m height above the warm degassing ground identified by Ilyinskaya et al. (2014) on the rim of the 1980-1981 summit crater of Hekla. From this map, we estimate a CO₂ flux of about 15 ± 7

tons/day. The large error in our flux estimate ($\pm 46\%$) is here reflecting the poor quality of our plume transport speed measurement, which determination was complicated by the strong winds blowing on top of Hekla by the time of our measurements. The flux value estimated matches closely the recently reported CO₂ flux for Hekla summit (13.7 ± 3.7 tons/day), obtained using conventional (accumulation chamber) soil survey techniques (Ilyinskaya et al. 2014).

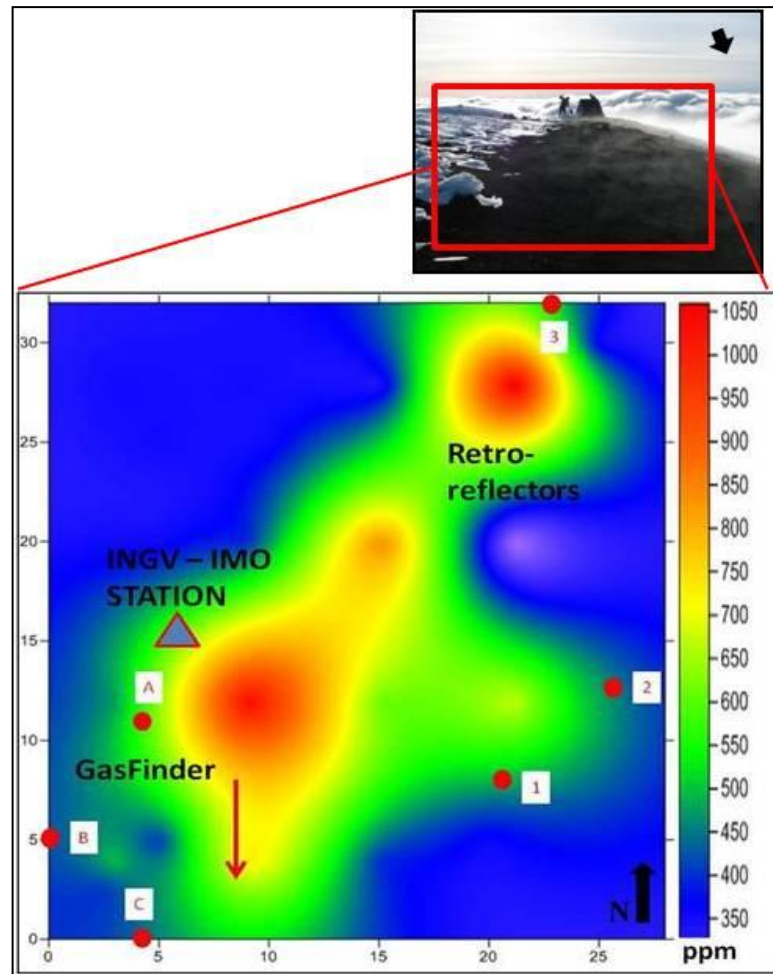


Fig. 5.15 Contour map of CO₂ mixing ratios (ppm), Hekla campaign of 2th July 2013. GasFinder and retro-reflectors positions are shown with letters and numbers respectively. Blue triangle: INGV-PA/IMO station; red arrow: principal direction of plume dispersal.

5.4 Krýsuvík (Iceland)

The Krýsuvík geothermal area is located on the Reykjanes Peninsula, in south-west Iceland. The peninsula is an oblique on-shore segment of the Mid-Atlantic ridge which formed since around 6-7 million years ago (Saemundsson 1979; Clifton and Schlische 2003). It is characterized by basaltic lavas ranging from picrite to tholeiite composition and hyaloclastite ridges formed in subglacial eruptions (Jónsson 1978). The Krýsuvík field is one of five presently active geothermal areas on the Reykjanes Peninsula (Markússon et al. 2011). Geothermal activity consists mainly of acid surface alteration and hot ground, steam vents and steam-heated hot springs and mud pots. Surface activity is concentrated in the Sveifluháls area, including Austurengjahver, and mostly within the small area of Seltún and Hveradalur (Markússon et al. 2011).

On 5th July 2013, we performed TDL observations in Hveradalur (63° 53,449'N, 22° 4,190'W; Fig. 5.16). This area included two major fumarolic manifestations (indicated as “FumA” and “FumB” in Fig. 5.16). The fumarolic vent “FumA” is monitored by a permanent Multi-GAS instrument (shown as a triangle in Fig. 5.16 and 5.18) deployed in a joint monitoring program led by BGS (British Geological Survey), INGV and IMO.

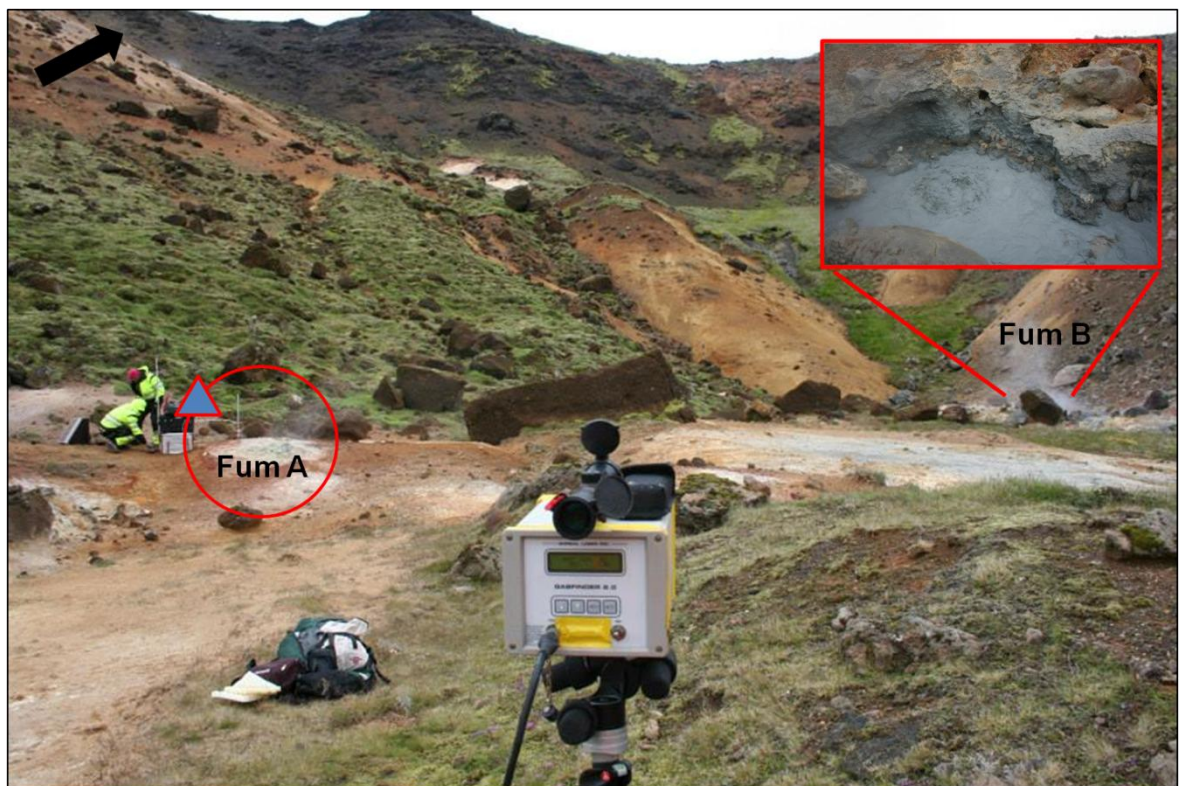


Fig. 5.16 Analysed area at Krýsuvík. “FumA” and “FumB” are the main degassing vents. A detail of “FumB” vent is given at the top of the picture. Blue triangle: IMO-INGV station. Black arrow: nord direction.

5.4.1 Results and Discussions

Acquiring for 1.5 hour on 5th July 2013, the GasFinder provided 1,150 readings (selected for nord-western trending wind).

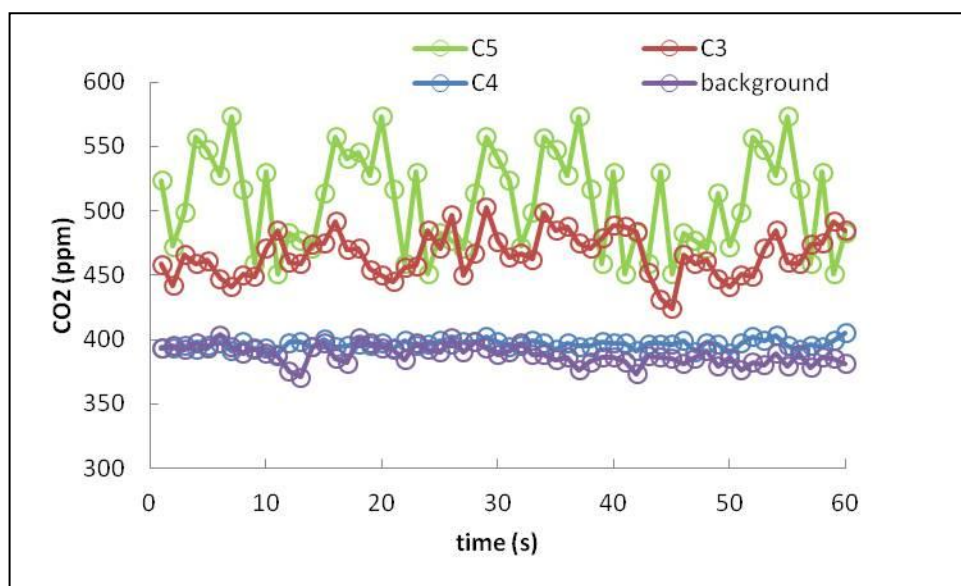


Fig. 5.17 Example of time-series of CO₂ mixing ratios (one minute data acquisition) at Krýsuvík obtained over three different categories of open paths: (i) near-vent plumes (C5); distal (aged) plumes (C3); plume margins (C4). Background values are also given.

The CO₂ contour map obtained at Krýsuvík is shown in figure 5.18. In this area, CO₂ mixing ratios ranged from 350-380 ppm at the periphery of the exhaling area, and up to ~500 ppm near the two main fumarolic vents (“FumA” and “FumB” in Fig. 5.16 and 5.18). For the Hveradalur fumarolic field of Krýsuvík, we estimate a CO₂ flux of 5.7 ± 0.9 tons/day. This is the first CO₂ output estimate for this area, at least to our knowledge.

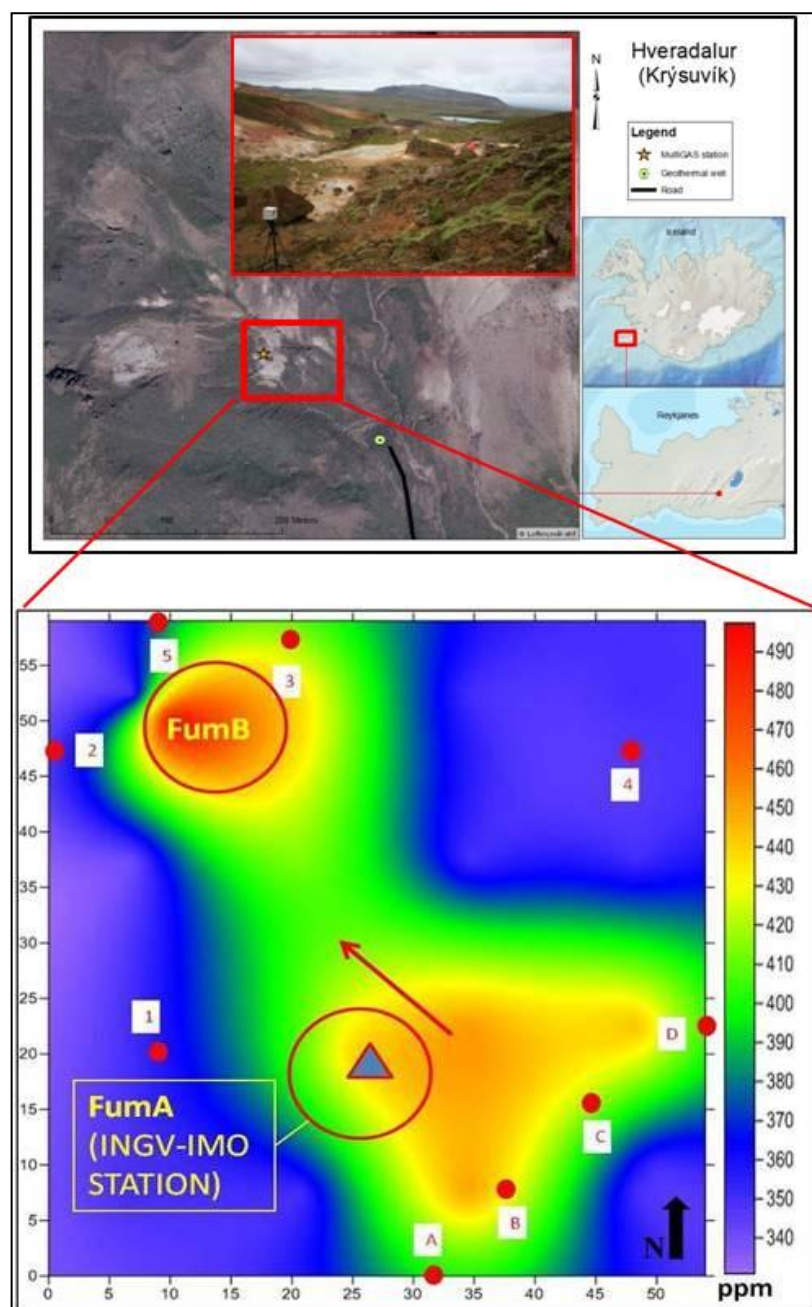


Fig. 5.18 Contour map of CO₂ mixing ratios (ppm), Krýsuvík (Hveradalur) campaign of 5th July 2013. GasFinder and retro-reflectors positions are shown with letters and numbers respectively. “FumA” and “FumB”: positions of main degassing vents; blue triangle: INGV-PA/IMO station; red arrow: principal direction of plume dispersal.

5.5 Vulcano island

Vulcano is a volcanic island belonging to the Aeolian Islands in the southern Tyrrhenian Sea in Italy. Since the last eruption in 1888-90, this closed-conduit volcanic system has been characterized by solfataric activity, located mainly in the summit area inside La Fossa crater. La Fossa cone (391 m a.s.l.) is a small, about 2-km diameter, strato-vulcano. All the explosive and effusive products of this cone have exhibited high potassium contents and chemical compositions ranging from trachytic to rhyolitic (Keller 1980). In the last decades, increasing degassing activity of vulcano Island indicated renewed activity, including large increase in fumarole temperature (Badalamenti et al. 1991; Chiodini et al. 1995; Capasso et al. 1997). Many episodes of fumarole gas/steam ratio change concentration were recorded in 1988-91, 1996, 1998, 2001, etc. (Paonita et al. 2002; Chiodini et al. 1996a; Capasso et al. 1999). Carbon dioxide represents the main constituent of anhydrous gases discharged in the summit areas of the volcano through the plume or from crater fumaroles (Chiodini et al. 2005; Inguaggiato et al. 2012). Attempts to measure the CO₂ output were considered in all geochemical monitoring programs (Brusca et al. 2004; Carapezza et al. 2004; Werner and Cardellini, 2006). Vulcano island fumaroles have been used as a natural laboratory to test new remote sensing techniques and different prototypes (Inguaggiato et al. 2012). In particular, Mori et al. (1995) used a FTIR Spectral Radiometer for remote measurements; Aiuppa et al. (2004) carried out an inter-comparison of different methodologies (FTIR, Filter-packs, direct sampling) on the plume; Tamburello et al. (2011) used UV camera measurements of fumarolic SO₂ degassing. Finally, Aiuppa et al (2004, 2005, 2006) and McGonigle et al. (2008) carried out measurements to determine H₂S/SO₂ and CO₂/SO₂ ratios and SO₂ fluxes with DOAS, Infra-Red and electrochemical sensors.

5.5.1 Results and Discussions

On 11th March 2014, the CO₂ emissions from La Fossa were investigated using the measurement configuration of figure 5.19.

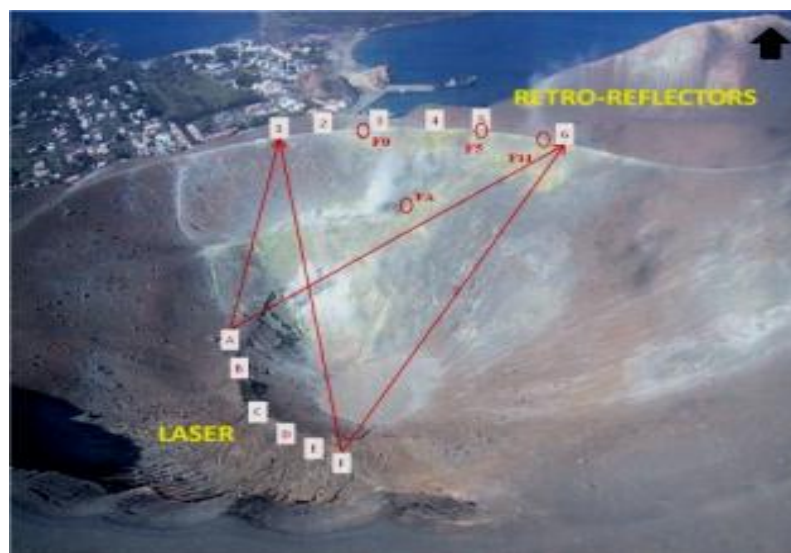


Fig. 5.19 Experimental set-up at La Fossa of Vulcano. The laser (letters) and retro-reflectors (numbers) positions are given. FA, F0, F5, and F11: the main degassing vents. Black arrow: nord direction.

During the campaign the laser operated for 2 hours (1,757 readings were selected). An example of time-series of mixing ratios is shown in figure 5.20.

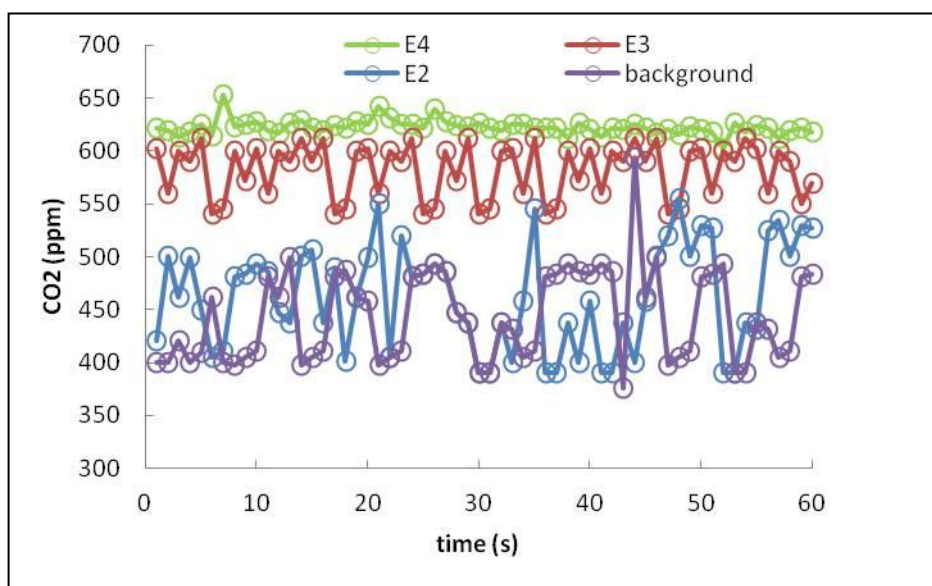


Fig. 5.20 Example of time-series of CO₂ mixing ratios (one minute data acquisition) at La Fossa of Vulcano obtained over three different categories of open paths: (i) near-vent plumes (E4); distal (aged) plumes (E3); plume margins (E2). Background values are also given.

The CO₂ distribution map of “La Fossa” crater at Vulcano Island is shown in figure 5.21. The highest CO₂ mixing ratios (up to 880 ppm; Fig. 5.21) were detected in correspondence of the principal fumaroles (“F0”, “F5” and “F11”) of the crater rim and the “FA” fumarolic field in the inner wall of the crater.

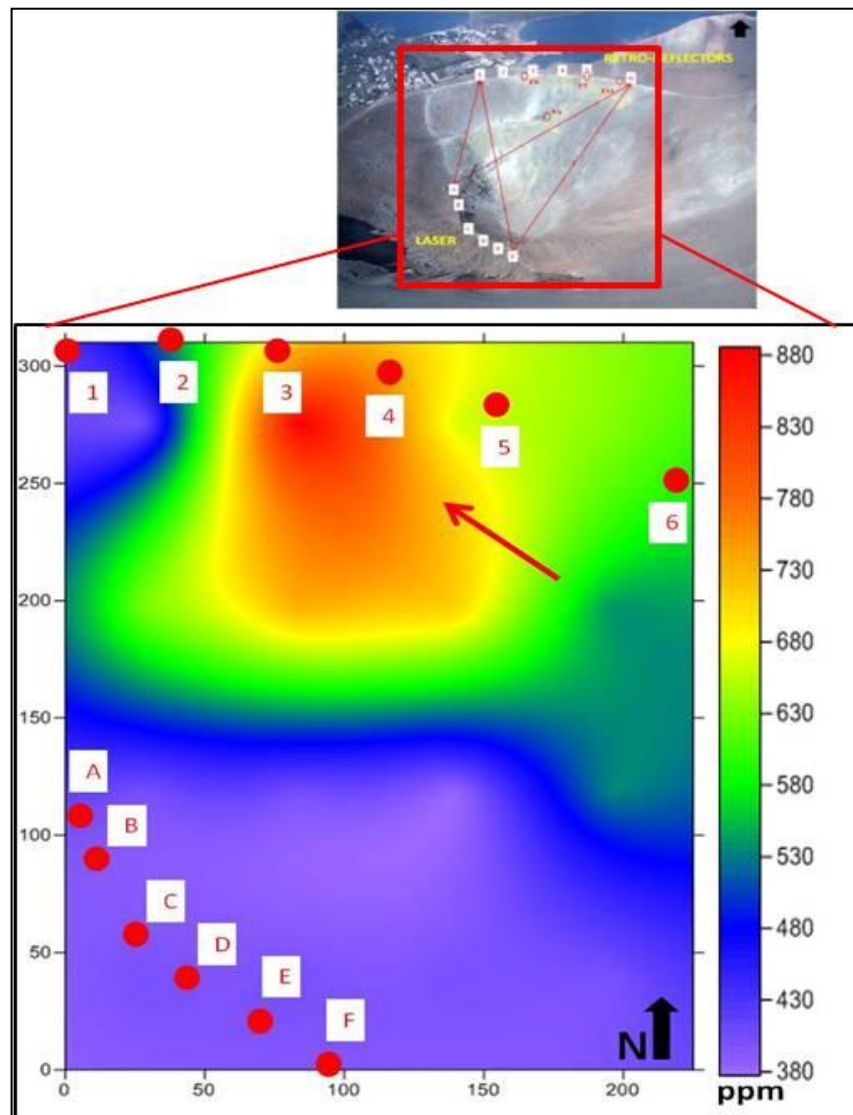


Fig. 5.21 Contour map of CO₂ mixing ratios (ppm), “La Fossa” campaign, Vulcano Island, 11th March 2014. GasFinder and retro-reflectors positions are shown with letters and numbers respectively. Red arrow: principal direction of plume dispersal.

The CO₂ flux at La Fossa crater was evaluated as 524 ± 108 tons/day. This is in the same range of CO₂ emissions obtained in previous studies by Aiuppa et al. (2005) (420 ± 250 t/d), Tamburello et al. (2011) (488 t/d, average of two campaigns in 2009) and Inguaggiato et al. (2012) (453 t/d) (see Fig. 5.22) using different techniques.

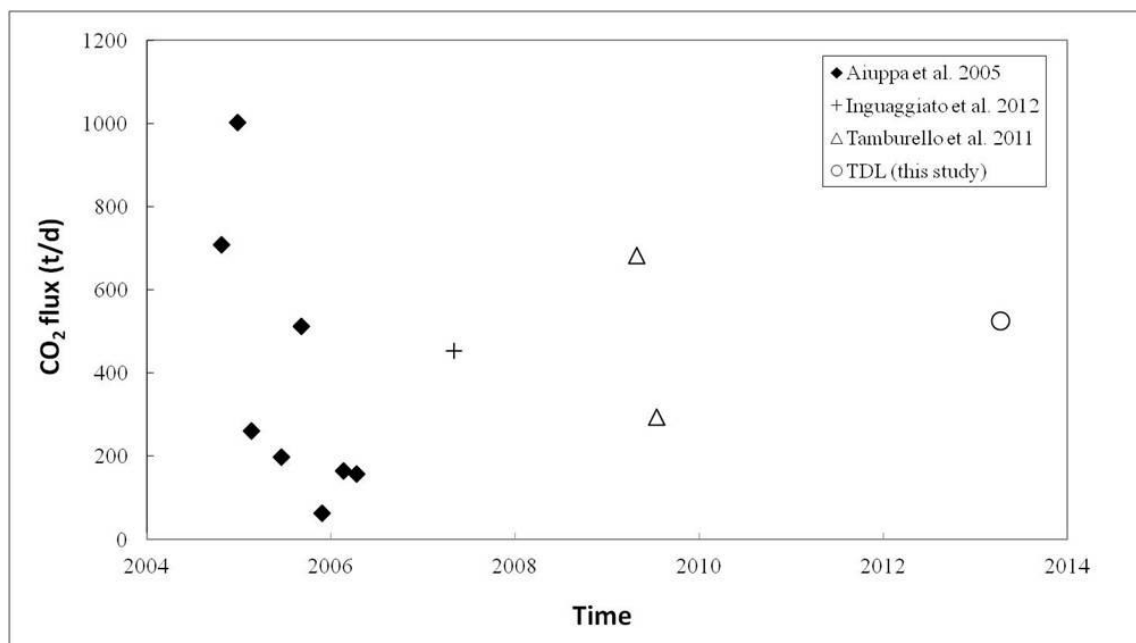


Fig. 5.22 Time-series of CO₂ flux values (tons/day) for “La Fossa crater” (Vulcano Island). Previous works: Aiuppa et al. (2005; 2006), Tamburello et al. (2011) and Inguaggiato et al. (2012). The flux value of 524 ± 108 t/d, obtained in this study, is also shown.

5.6 Paternò

Paternò (Lon 14.89°; Lat 37.57°) in the southern flank of Etna volcano (Fig. 5.23), is famous for the mud spots, volcano-sedimentary manifestations that drain gases and hot saline waters from underlying hydrothermal system (from which the name “Salinelle”) (D’Alessandro et al. 1997).

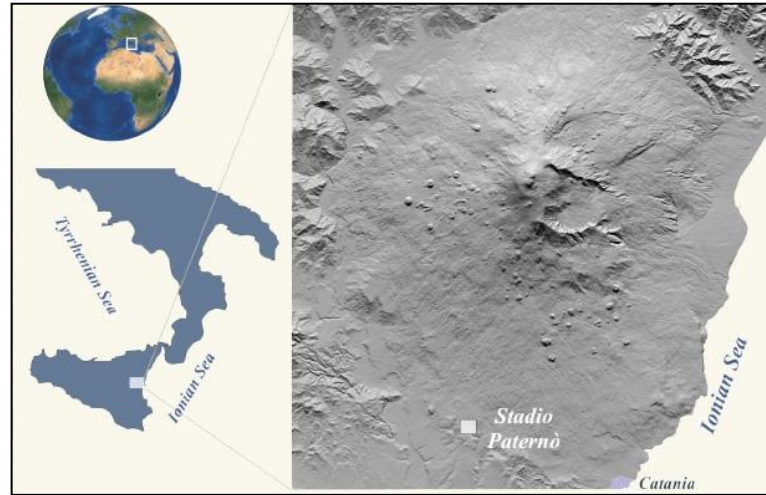


Fig. 5.23 Location of the study area of Paternò, in southern flank of Mt. Etna (Italy).

The gas emitted consists mainly of CO₂, with CH₄, N₂ and He as minor species. CO₂ and He stable isotopes indicate a clear magmatic origin for these gases, and their compositional changes during either eruptive or rest periods closely parallel that of crater fumaroles (Paonita et al. 2012). Although these manifestations are the most significant CO₂ emitters outside the crater area, their mass output has never been measured.

Gas bubbling (Fig. 5.24) within the mud pools is vigorous. Occasionally, paroxysmal emissions of hot water (40-50°C) and mud have been observed in the past (Silvestri 1879; Cumin 1954). These events have been correlated to coeval earthquakes. Indeed, the shaking produced by the earthquake can trigger explosive release of gas trapped within clayey sediments, carrying mud and salt water. The monitoring of mud volcanoes in the Southern flank of Mt. Etna is particularly appealing because the geological setting allows gas pressurization in this area, as an effect of variations of either the stress field or the volcanic activity. The periodic monitoring of gas flow rate in the mud volcano would provide direct information about the eventual pressurization of the local hydrothermal system (Chiodini 1996b).



Fig. 5.24 View of analyzed area at Paternò. Gas bubbling in the mud-spots is noticeable.

5.6.1 Results and discussions

Acquiring for ~ 4 hours on 4th April 2014, the GasFinder provided ~ 6000 readings (the dataset was filtered for wind speed ranged from 6 to 8 m/s and sud-east oriented dispersal). An example of one minute acquisition in three different paths is given in figure 5.25.

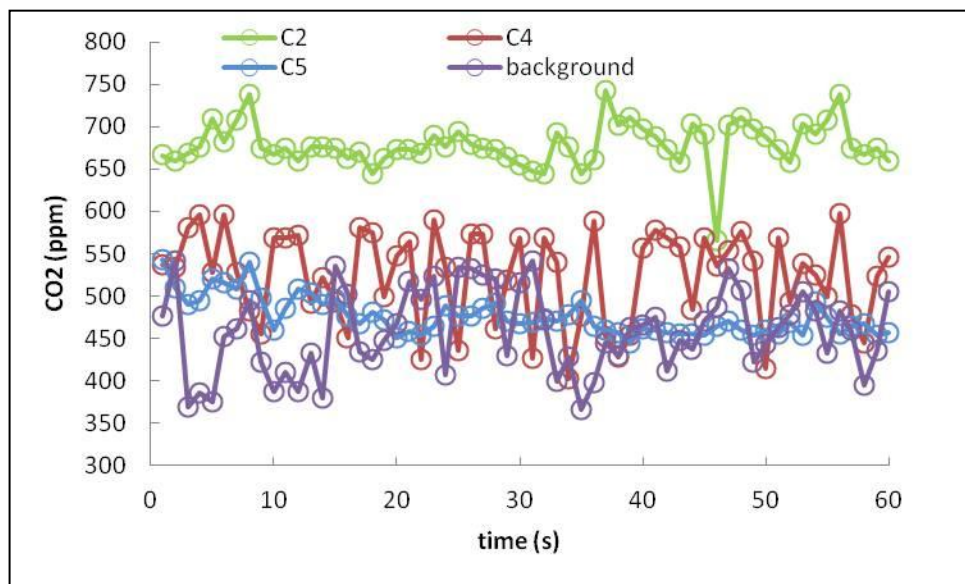


Fig. 5.25 Example of time-series of CO₂ mixing ratios (one minute data acquisition) at Paternò obtained over three different categories of open paths: (i) near-vent plumes (C2); distal (aged) plumes (C4); plume margins (C5). Background values are also given.

During the campaign a home-made apparatus (Fig. 5.26), able to capture the bubbles over an area of 0.64 m^2 , and a Multi-GAS (Fig. 5.27) were also used.

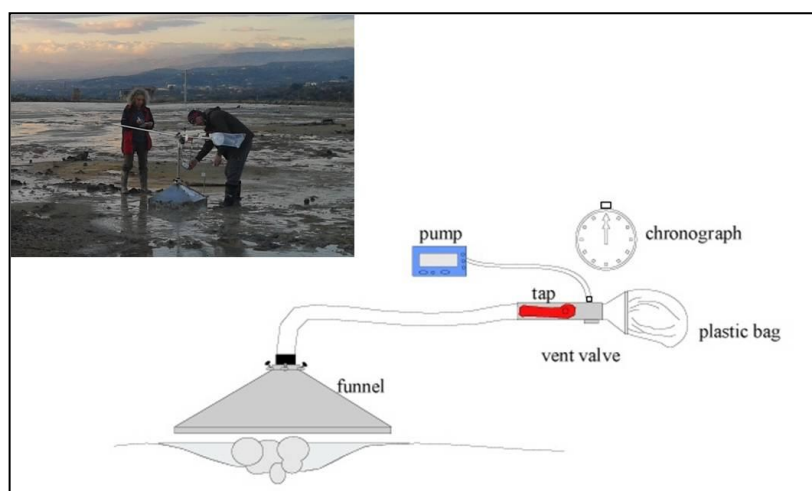


Fig. 5.26 Scheme of the home-made apparatus used to measure the flow rate value at each bubbling mud pool during the campaign on 4th April 2014.

As shown in figure 5.26, the apparatus is made of a stainless-steel funnel (dimension $0.8 \times 0.8 \text{ m}$) connected through a tap to a plastic bag. The plastic bag, pre-evacuated by mean of a pump at constant flow rate, is let to inflate with the bubbling gas by opening the tap. From the time of inflation and the volume of the bag (by means of the pump at constant flow rate), the flow rate is easily calculated. Over an area of about 6000 m^2 , the flow rate of every single bubbling pool, was measured, providing that the minimum flux rate was 0.5 l/min (Federico et al. 2014).

Direct measurements of gas flow rate have been compared with in-plume CO_2 measurements from a single mud pool. The method consists in detecting CO_2 mixing ratios by means of an IR spectrometer (inside Multi-GAS system, Fig. 5.27) over a cross section of the gas plume released by the bubbling pool (Fig. 5.27a), to obtain the Integrated Column Amount value.

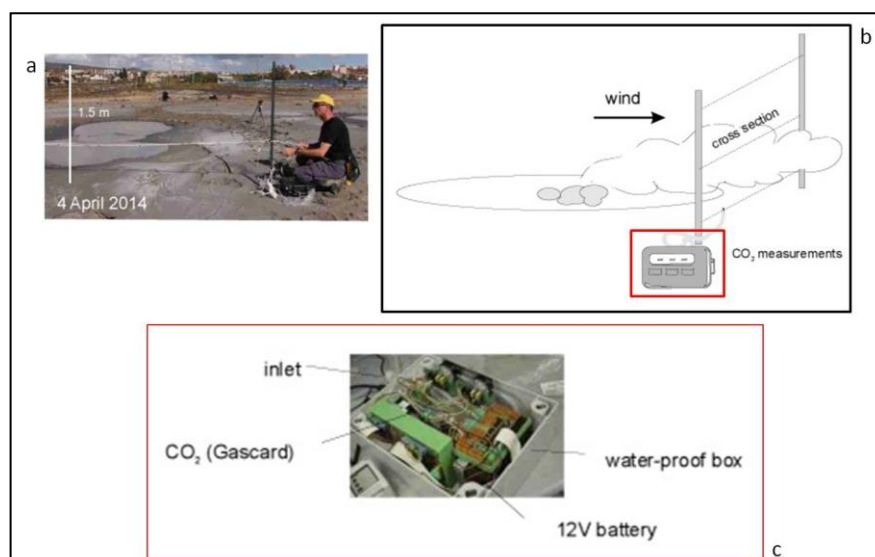


Fig. 5.27 **a-b** Scheme of the cross section of the gas plume released by the bubbling pool performed by using the MultiGAS at three different heights (under 1.5 m); **c** scheme of a MultiGAS portable system. The main components are indicated. A IR spectrometer Gascard for CO₂ measurements was used.

The results of the field campaign carried out via GasFinder and the home-made apparatus on 4th April 2014, are shown in a classed image map (Fig. 5.28). The most vigorous emissions are all concentrated in a 100 m² wide area. During the campaign, the maximum flow rate from a single bubbling pool was 115 l/m. The overall gas flow rate was 390 l/m. Considering an average CO₂ content of 95% in the bubbling pools, the total CO₂ output was 1.1 t/d (Federico et al. 2014). As regards the CO₂ distribution obtained from GasFinder dataset (plotted in the same figure), the background values were detected outside and up-wind of the main degassing area; instead, the highest mixing ratio values (from >500 to 690 ppmv) were detected down-wind respect to the bubbling vents. Once obtained the CO₂ distribution map, it would be possible to compute the overall CO₂ flux rate of the total investigated area by multiplying the Integrated Column Amount by the vertical transport speed.

Accurate measurements of the vertical upward air convections, weren't realized for Paternò area of "Salinelle". Considering a vertical gas speed estimation of about 0.03 m/s, the CO₂ flux could be 1.5 t/d.

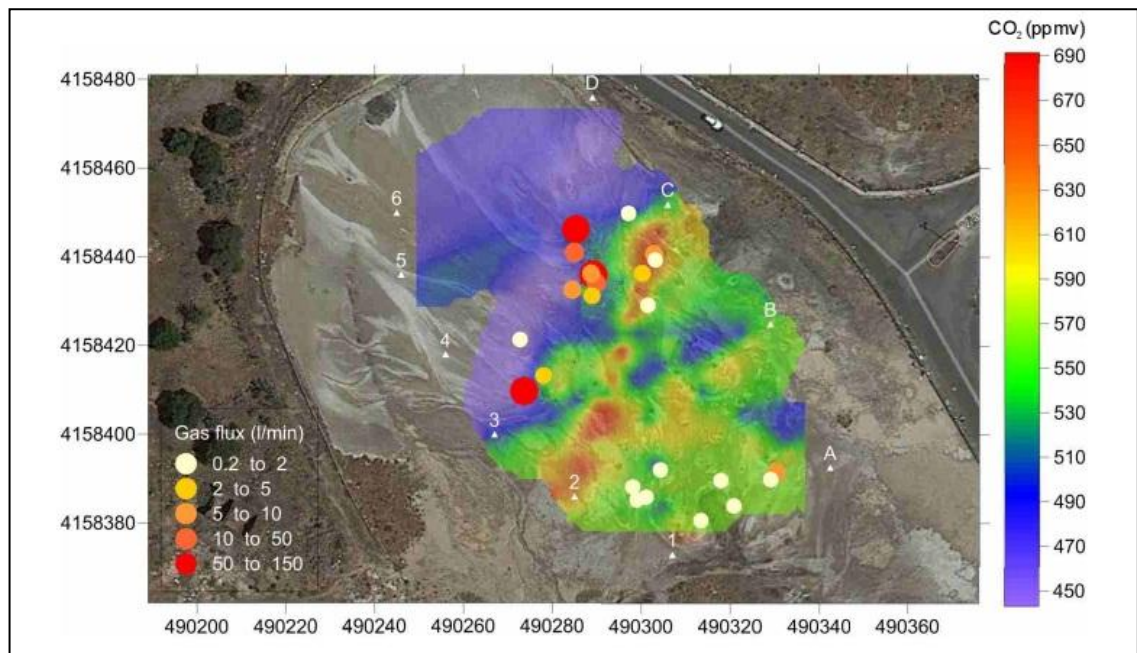


Fig. 5.28 Classed image map obtained by using the both home-made apparatus and GasFinder on 4th April 2014 campaign. The most vigorous emissions are all concentrated in a 100 m² wide area. During the campaign, the maximum flow rate from a single bubbling pool was 115 l/m (red circles). The overall gas flow rate was 390 l/m. CO₂ distribution, obtained from GasFinder dataset, is plotted. As expected, the background values were detected outside and up-wind of the main degassing area; instead, the highest mixing ratio values (from >500 to 690 ppmv) were closely down-wind with respect to the bubbling vents.

During the campaign, the MultiGAS cross sections (at three different heights from soil-level) were performed to extrapolate a flux rate value to compare with the results from the home-made apparatus. The results of CO₂ concentration measurements (ranged from 400 to 1000 ppmv) are shown in figure 5.29. The difference between the direct flux measurements (by home-made apparatus) and the CO₂ flux estimate by MultiGAS-results is about 12%. Flux estimate based on CO₂ MultiGAS measurements is lower due to the defective detection of the CO₂ anomalies near the ground (Fig. 5.29).

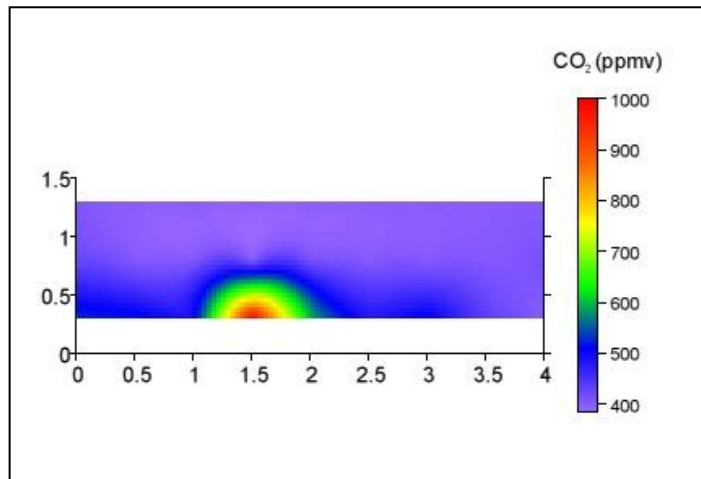


Fig. 5.29 Results of MultiGAS cross sections (at three heights under 1.5 m). The CO₂ concentrations are given (ranged from 400 to 1000 ppmv). The flux estimate is lower (~12%) due to the defective detection of the CO₂ anomalies near the ground.

The computed value of CO₂ emitted from the mud volcano (1.1 t/d) is about one order of magnitude lower than the CO₂ mass rate transported by the local shallow aquifer (Fig. 5.30): in an area of about 46 km², the mass rate of CO₂ transported by water is 16 t/d (Federico et al. 2014).

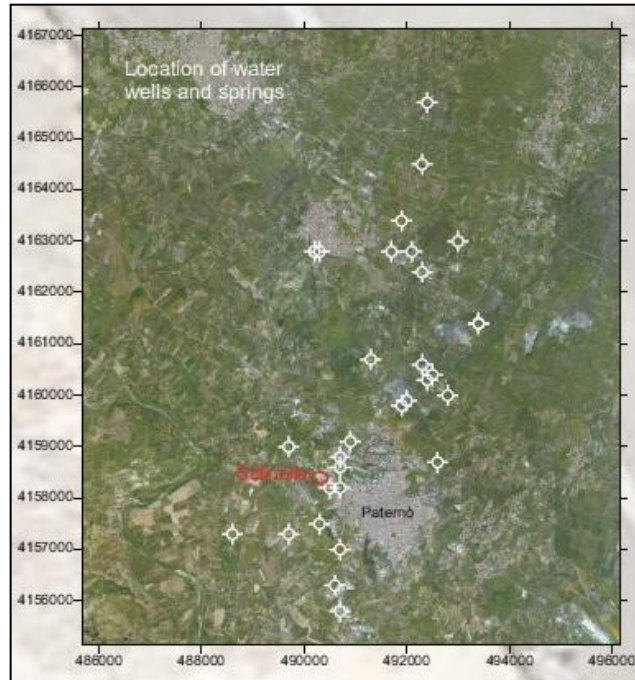


Fig. 5.30 Location of shallow aquifer close to Paternò area.

5.7 Furnas volcano (Azores)

The Azores archipelago is composed of nine volcanic islands located in the North Atlantic Ocean in the triple junction domain of American, Eurasian and Nubian plates (Searle 1980; Viveiros et al. 2012) (Fig. 5.31a). Due to the interaction between the complex tectonic setting and the presence of a mantle melting anomaly (Beier et al. 2010), seismicity and volcanism are frequent in the archipelago.

At present, volcanic activity in the Azores archipelago is characterised by seismic activity and secondary manifestations of volcanism such as low temperature fumaroles (95–100°C), steaming ground, thermal springs, cold CO₂-rich springs and soil diffuse degassing areas. Special attention has been given to CO₂ diffuse emissions (Ferreira 2005).

The most important degassing zones are located in São Miguel, Terceira and Graciosa islands and at some submarine volcano-tectonic structures along the Terceira Rift.

São Miguel Island, the biggest island of the archipelago, is characterized by three main active polygenetic volcanoes (Sete Cidades, Fogo and Furnas) with fissural volcanic zones in between (Fig. 5.31b).

Furnas Volcano is located in the eastern part of the island and its oldest volcanic products are dated to 100,000 years BP (Moore 1990).

After the last eruption, occurred in 1630 (Cole et al. 1995), hydrothermal explosions were reported in 1840–41, 1944 and 1990 from a fumarole belonging to the Furnas Village fumarolic field (Ferreira 1994). Present-day volcanic activity is characterised by widespread hydrothermalism. Most of the manifestations are located inside the caldera (Fig. 5.32), where three main fumarolic fields were observed (Viveiros et al. 2012):

- 1 Furnas Lake
- 2 Furnas Village
- 3 Ribeira dos Tambores.

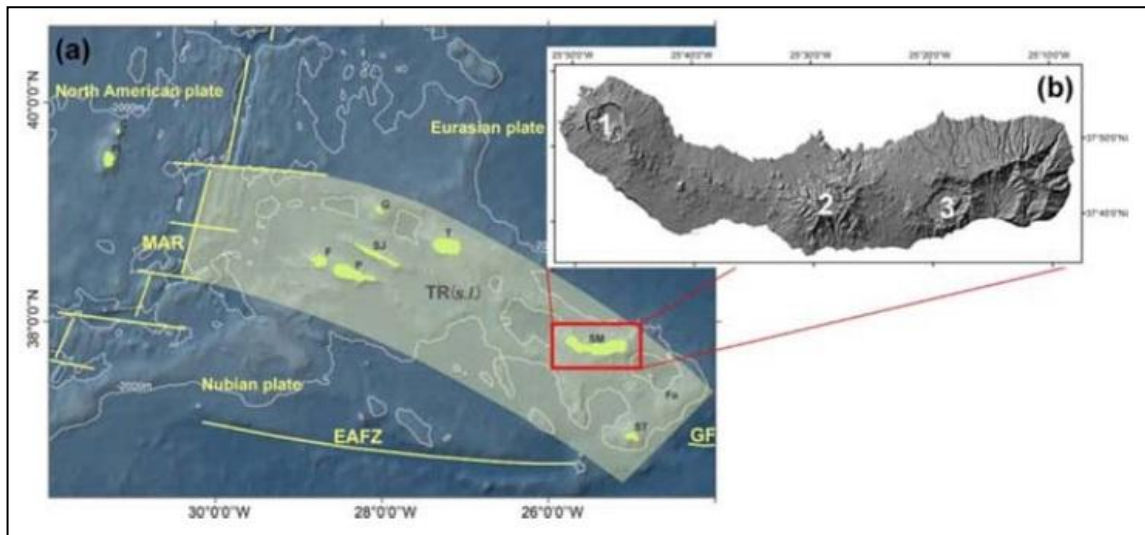


Figure 5.31 (a) Location map of the Azores archipelago with the main tectonic structures. Legend: MAR - Mid-Atlantic Ridge; EAFZ - East Azores Fracture Zone; GF - Gloria Fault; TR (s.l.) - Terceira Rift; C - Corvo; FI - Flores; F - Faial; P - Pico; SJ - São Jorge; G - Graciosa; T - Terceira; SM - São Miguel; ST - Santa Maria; Fo - Formigas Islet. White line represents bathymetry of -2000 m. (b) São Miguel Island digital elevation model (DEM) with location of the main active volcanic systems: (1) Sete Cidades, (2) Fogo (or Água de Pau) and (3) Furnas volcanoes (taken from Viveiros et al. 2012).

The fumarolic fields Furnas Lake and Furnas Village (“A” and “B” in figure 5.32) are located inside the Furnas caldera, defining a WNW-ESE cluster compatible with a major regional tectonic trend that cross the island (Gaspar et al. 1995).

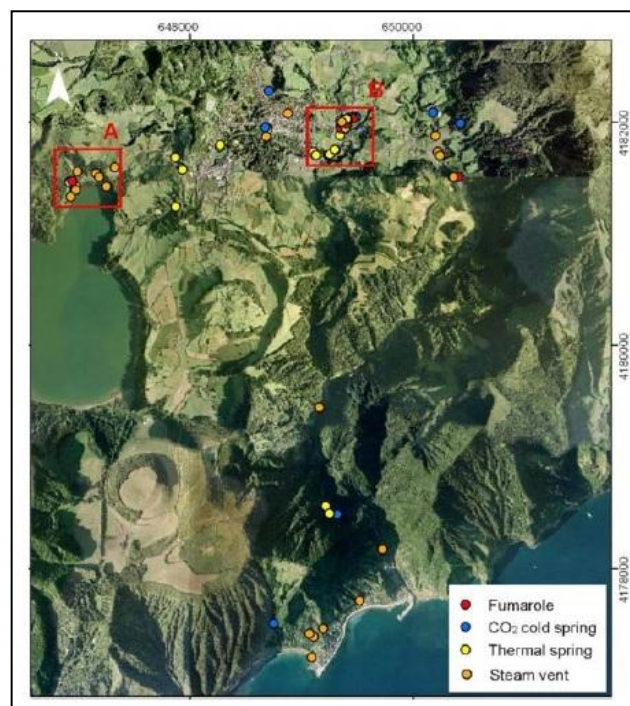


Fig. 5.32 Hydrothermal manifestations at Furnas Volcano. Cold CO₂-rich springs and thermal springs are identified by Costa (2006). Steam vents were mapped by Viveiros et al. (2010). Red squares ‘A’ and ‘B’ indicate the main fumarolic fields, Furnas Lake and Furnas Village, respectively.

The main components of the fumarolic discharges are water vapour followed by carbon dioxide, hydrogen sulphide, nitrogen, hydrogen, oxygen, methane and argon (Ferreira 1994; Ferreira and Oskarsson 1999; Ferreira et al. 2005).

The first soil diffuse degassing studies carried out in the archipelago (Baubron et al. 1994; Baxter et al. 1999; Oskarsson et al. 1999) were performed in Furnas caldera in the early nineties, showing that Furnas village is sited over an important CO₂ degassing area.

5.7.1 Results and discussions

In August 2014, two field-campaigns were carried out in the two main fumarolic fields: “Furnas Lake” (“A” in figure 5.32), on the north coast of “Lagoa das Furnas”, and “Furnas Village” (Caldeiras), in the eastern side of the caldera (“B” in figure 5.32).

The former is characterized by surface alteration of kaolinite, which indicates acid leaching of the surface layer (Ferreira and Oskarsson 1999). Here, three main degassing vents were investigated (Fig. 5.33): a vigorous degassing vent with boiling water jet (close to mirror 3-position in figure 5.33); two smaller fumaroles located in north-western part of the site (close to mirror 2-position in figure 5.33); and a mud pool degassing vent (close to mirror 5-position in figure 5.33).

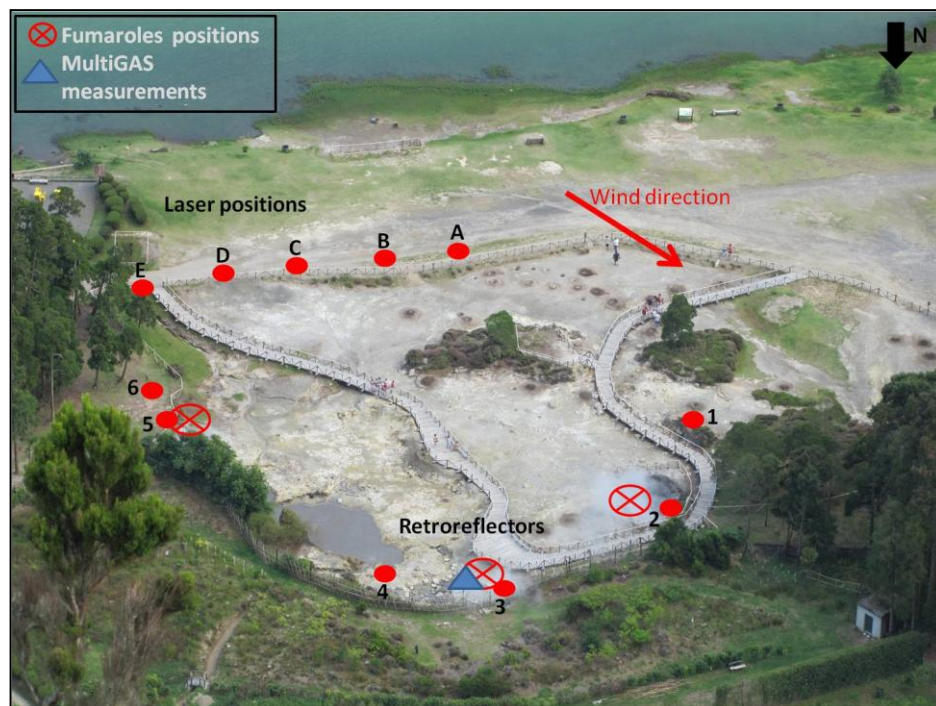


Fig. 5.33 Furnas Lake fumarolic site saw from the top of northern part of the volcano caldera. The positions of GasFinder and retro-reflectors are shown with letters and numbers, respectively. The positions of MultiGAS measurement-point (blue triangle) and the degassing vents (red crossed-circles) are also given.

On 19th August 2014, acquiring for ~ 6 hours, the GasFinder provided ~ 3600 readings (the dataset was filtered for wind nord-west oriented dispersal). An example of one-minute acquisition in three different paths is given in figure 5.34.

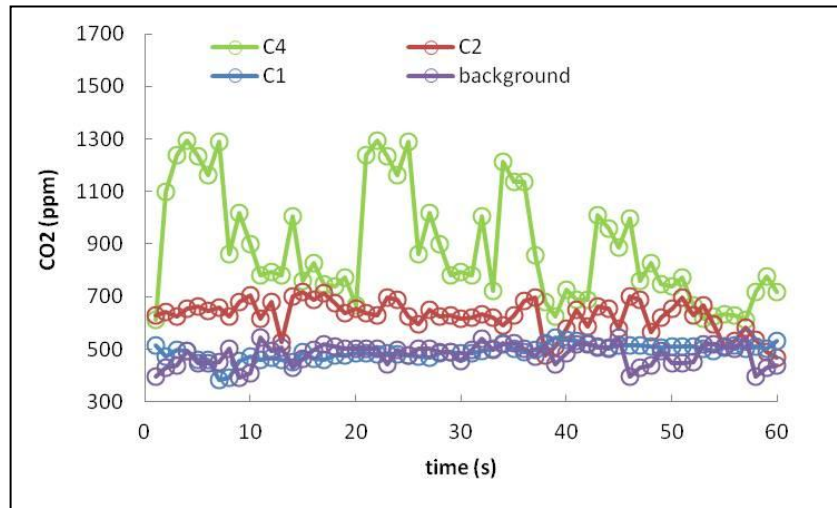


Fig. 5.34 Example of time-series of CO₂ mixing ratios (one minute data acquisition) at Furnas Lake obtained over three different categories of open paths: (i) near-vent plumes (C4); distal (aged) plumes (C2); plume margins (C1). Background values are also given.

Figure 5.35 is a CO₂ contour map derived from GasFinder dataset. CO₂ mixing ratio values range from 380 to ~ 900 ppm. In detail, the lower CO₂ mixing ratios were detected outside the fumarolic field; instead the higher mixing ratios (580-780 ppm) were found in down-wind direction and close to main degassing vents. A peak of CO₂ mixing ratio (~ 900 ppm) was detected close to the jet-water degassing vent (mirror 3-position) and a little water-pool (close to mirror 4-position; Figs. 5.33 and 5.35).

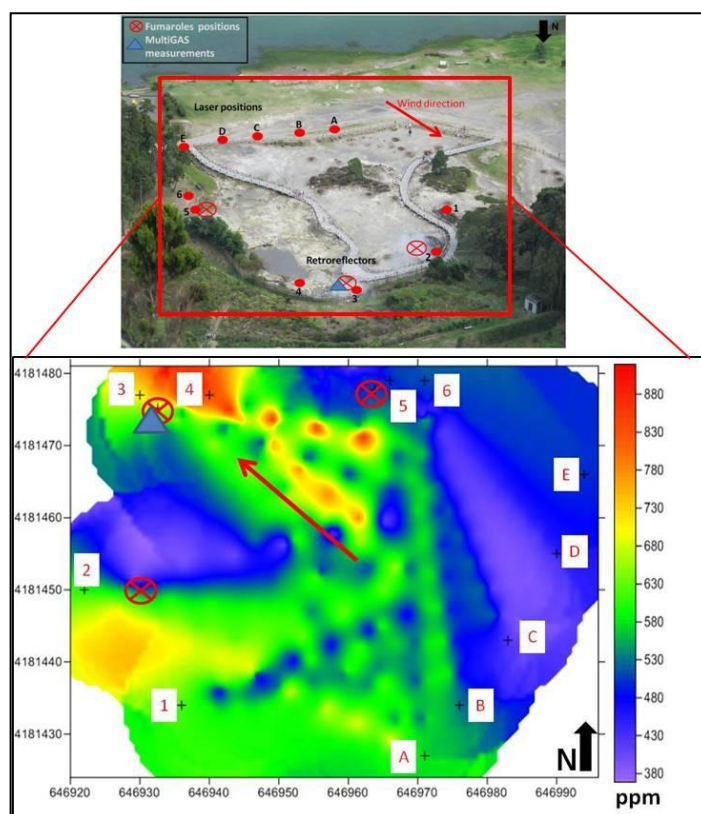


Fig. 5.35 Contour map of CO₂ mixing ratios (ppm) at “Furnas Lake” survey on 19th August 2014. GasFinder and retro-reflectors positions are shown with letters and numbers respectively. Investigated fumaroles (red crossed-circles) and MultiGAS measurement-point (blue triangle) positions are given. Red arrow: principal direction of plume dispersal.

Integrating the CO₂ contour map (Fig. 5.35), and multiplying this for the vertical gas transport speed (1.1 m/s), a CO₂ emission of 35 ± 3.1 t/d was estimated for an area of 4332 m².

During the same campaign, soil CO₂ effluxes were measured using an accumulation chamber method by Fátima Viveiros (from university of Azores in Ponta Delgada city). A total of 124 measurements were carried out in an area of approximately 3666 m². The CO₂ emitted in that area was 5.45 t/d, which was based on IDW deterministic interpolation method for a preliminary analysis (Fátima Viveiros pers. comm.).

Finally, the MultiGAS results obtained for the plume of the main jet-water degassing vent (close to mirror 3-position; fig. 5.33) are consistent with literature data. In detail, a mean CO₂/H₂S ratio of 353 (Fig. 5.36) was obtained, which fits well with a mean ratio of 348 found in a chemical survey in fumarolic samples (Ferreira and Oskarsson 1999). Using the CO₂/H₂S ratio measured from MultiGAS datasets, a H₂S flux of 0.099 t/d was estimated.

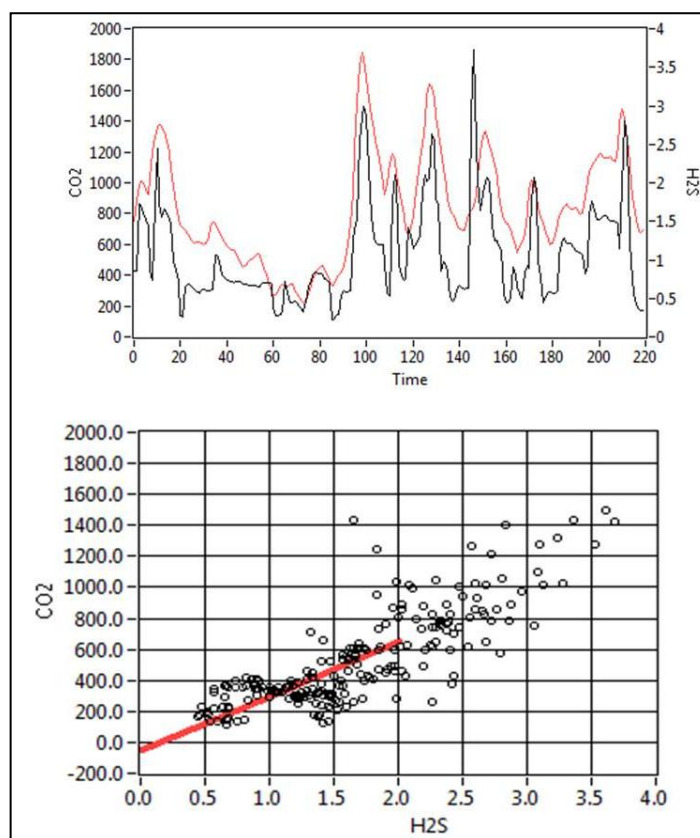


Fig. 5.36 Top: CO₂ and H₂S signals detected in 220 measurements close to the main degassing vent located in Furnas Lake site. Bottom: Correlation between two signals. The plots are exported by “RatioCalc” (a program of Giancarlo Tamburello - University of Palermo). In this example, the CO₂/H₂S is 352 (close to the mean ratio value found in the entire acquired measurements) and the R² regression line is 0.62.

“Furnas Village”, is the largest fumarole of the Furnas caldera, where several other moderately large fumaroles are active within an area of several hundred square metres. Of special importance is the “Caldeira Grande” vent, where hydrothermal fluid is discharged. “Caldeira do Asmodeu” is a vigorously boiling fumarole where steam explosions have occasionally occurred. “Caldeira Grande” and “Caldeira do Asmodeu” were previously studied by Cruz et al. (1999) and Ferreira and Oskarsson (1999). They are referred as “CG” and “CdA” in the subsequent text and figures (Fig 5.37).

On 22nd August 2014, acquiring for ~ 4 hours, the GasFinder provided ~ 3200 readings (the dataset was filtered for wind nord/nord-west oriented dispersal; Fig. 5.37).

Figure 5.38 is an example of time-series of CO₂ mixing ratios (one minute data acquisition) at Furnas Village obtained over three different categories of open paths: (i) near-vent plumes (E1); distal (aged) plumes (E2); plume margins (E3).

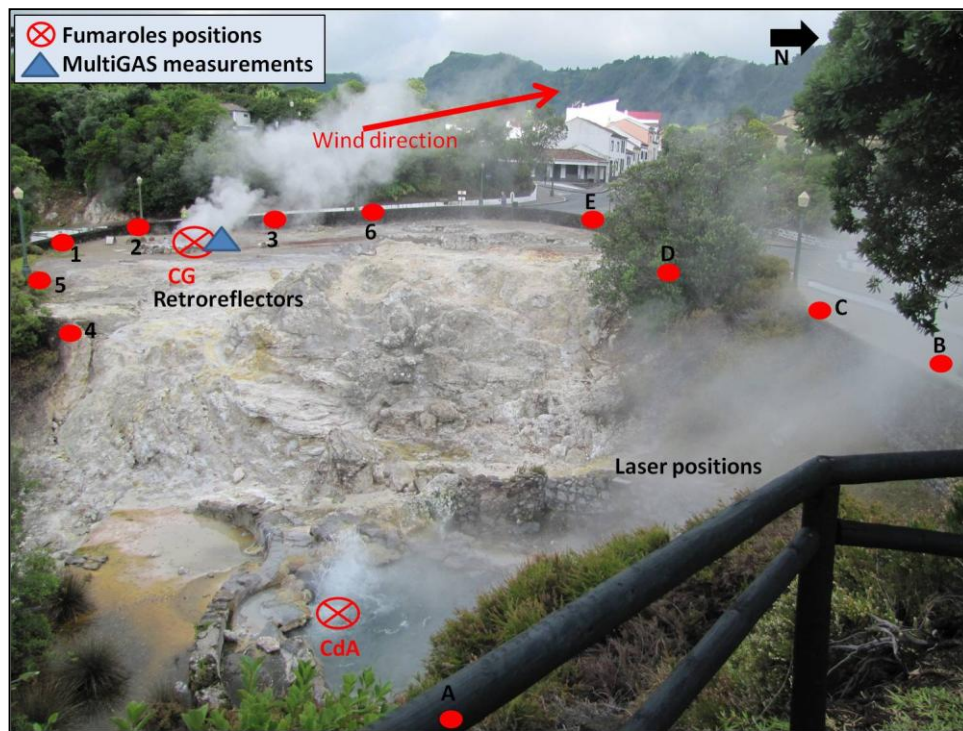


Fig. 5.37 Furnas Village fumarolic site. The positions of GasFinder and retro-reflectors are shown with letters and numbers, respectively. The positions of MultiGAS measurement-point (blue triangle) and two main degassing vents (“CG” and “CdA”, red crossed-circles) are also given.

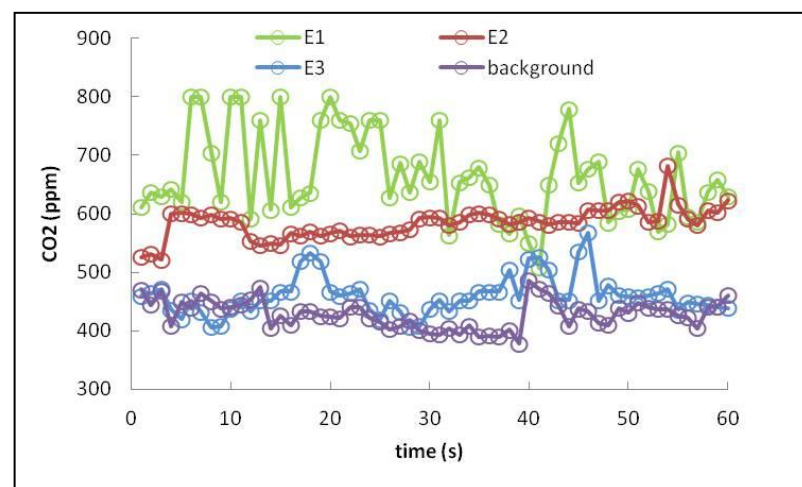


Fig. 5.38 Example of time-series of CO₂ mixing ratios (one minute data acquisition) at Furnas Village obtained over three different categories of open paths: (i) near-vent plumes (E1); distal (aged) plumes (E2); plume margins (E3). Background values are also given.

Figure 5.39 is a CO₂ contour map derived from GasFinder dataset. CO₂ mixing ratio detections (ranged from 360 to ~ 800 ppm) are lower than for “Furnas Lake” site. Here, is possible to notice a diffuse degassing area with moderately-high-values (500-660 ppm) for the presence of others smaller degassing vents placed between CG and CdA. Peaks of CO₂

mixing ratio (~ 700 - 800 ppm) are consistent with the plume/wind dispersal. The lower CO_2 mixing ratios were detected up-wind outside fumaroles positions (Fig. 5.39).

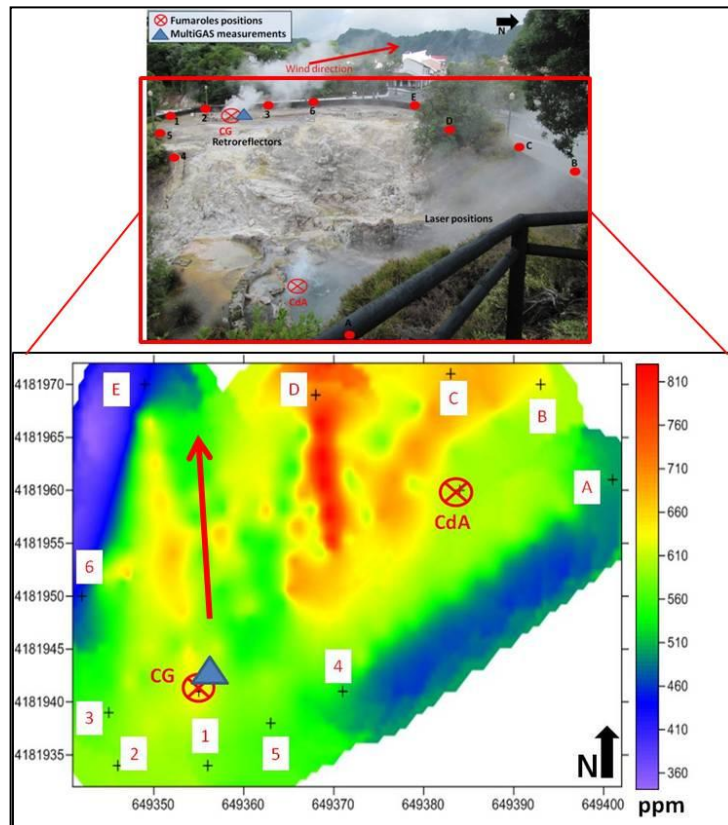


Fig. 5.39 Contour map of CO_2 mixing ratios (ppm) at “Furnas Village” survey on 22nd August 2014. GasFinder and retro-reflectors positions are shown with letters and numbers respectively. Investigated fumaroles (red crossed-circles) and MultiGAS measurement-point (blue triangle) positions are given. Red arrow: principal direction of plume dispersal. CG: Caldeira Grande; CdA: Caldeira do Asmodeu.

The estimated CO_2 emission for this survey is 25.5 ± 10 t/d in an area of 2440 m^2 .

Simultaneous accumulation chamber survey (95 soil CO_2 flux measurements) was carried out in an area of about 2300 m^2 . The CO_2 emitted in that area was 2.5 t/d, which was based on IDW deterministic interpolation method for a preliminary analysis (Fátima Viveiros pers. comm.).

At Furnas village, the $\text{CO}_2/\text{H}_2\text{S}$ mean ratio of 150 measured by using MultiGAS portable system (close to “Caldeira Grande”; Fig. 5.37 and 5.39) are consistent with the mean ratio (120) found by Ferreira and Oskarsson (1999). Using the $\text{CO}_2/\text{H}_2\text{S}$ ratio measured from MultiGAS datasets, a H_2S flux of 0.17 t/d was estimated. Here, a $\text{H}_2\text{O}/\text{CO}_2$ ratio, ranged 12-15, was also measured.

Finally, combining the fumaroles CO_2 flux (~ 60.5 t/d), with the total soil CO_2 emission (~ 8 t/d), the total cumulative CO_2 output at Furnas volcano was estimated of ~ 68.5 t/d.

Chapter 6

CO₂ emissions from the analyzed areas: implications

6.1 CO₂ emissions from the investigated areas

The ability of the TDL to contour CO₂ mixing ratios (Figs. 5.6 - 5.7 - 5.8 - 5.12 - 5.15 - 5.18 - 5.21 - 5.28 - 5.35 and 5.39) in a volcanic gas plume cross section opens the way to quantification of the fumarolic CO₂ output from each of the studied areas.

The calculated CO₂ fluxes are listed, for each site and each campaign, in Table 6.1. The accuracy (1 σ) of the mean flux estimates are calculated from error propagation theory applied to both ICA and plume transport vertical speed.

Table 6.1. CO₂ fluxes (in tons/day) and standard deviation (1 σ) calculated in the investigated areas of Campi Flegrei, Nea Kameni, Hekla, Krýsuvík, Vulcano and Furnas by GasFinder datasets. The plume transport vertical speed (in m/s) is also given for each site.

Site	Date	Gas speed (m/s)	CO ₂ Flux (t/d)
		($\pm 1 \sigma$)	($\pm 1 \sigma$)
Campi Flegrei ^a	2012-2013 ^b	1.40 \pm 0.60	487 \pm 97.9
Nea Kameni	9 th April 2013	1.20 \pm 0.40	63 \pm 22
Hekla	2 nd July 2013	1.00 \pm 0.50	15 \pm 7
Krýsuvík	5 th July 2013	1.17 \pm 0.18	5.7 \pm 0.9
Vulcano	11 th March 2014	1.00 \pm 0.20	524 \pm 108
Furnas Lake	19 th August 2014	1.10 \pm 0.09	35 \pm 3.1
Furnas Village	22 nd August 2014	1.04 \pm 0.40	25.5 \pm 10

^aTotal CO₂ fumarolic budget is considered: Pisciarelli and Solfatara sites

^bPisciarelli campaigns: 25th October 2012; 29th January and 8th May 2013. Solfatara campaigns: 26th October 2012; 30th January and 9th May 2013

As regards the survey at Furnas caldera, a total CO₂ budget of ~60 t/d was estimated, which is ~2 times higher than the total flux estimated in the both sites (14 t/d at Furnas Lake and 13-15 t/d at Furnas Village) by Viveiros et al. (2010; 2012). The accumulation chamber results for the campaign carried out in August are not known with certainty.

6.2 Implications to global scale

The volcanoes in the present work display a range of fumarolic activity, from weak (Hekla) to moderately strong (“La Fossa” of Vulcano and Campi Flegrei). As such, our results add novel information on the CO₂ degassing regime of quiescent volcanoes in Solfatara stage of activity, and on their potential contribution to the global volcanic CO₂ budget.

The current state-of-the-art of volcanic CO₂ flux research has recently been summarised in Burton et al. (2013). The authors presented a compilation of 33 subaerial volcanoes for which CO₂ flux observations were available at that time. These "measured" emissions totalled a cumulative CO₂ output of 59.7 Mt/yr. The same authors used linear extrapolation, from the measured 33 to the 150 plume-creating, passively degassing volcanoes on the GVP catalogue (Siebert and Simkin 2002), to obtain an extrapolated global volcanic CO₂ flux of ~271 Mt/yr.

The linear extrapolation approach of Burton et al. (2013) is based on the implicit assumption that the measured 33 volcanoes represent a statistically significant sub-set of the volcanic CO₂ flux population. However, I argue that past volcanic CO₂ observations have been prioritized at strongly degassing volcanoes under unrests; therefore, the 33 volcanoes population may be biased towards the category of top gas emitter, implying the linear extrapolation technique may be incorrect. The low CO₂ output associated to “quiet” volcanoes, as reported in the present work, corroborates this conclusion.

The alternative extrapolation approach used to quantify CO₂ emissions from “unmeasured” volcanoes is to assume that the distribution of volcanic CO₂ fluxes obeys a power law (Brantley and Koepnick 1995), as other geophysical parameters do (Marret and Allmendinger 1991; Turcotte 1992). If volcanic emissions follow a power-law distribution, then the number of volcanoes (N) with an emission rate $\geq f$ are given by:

$$N = af^{-c} \quad (6.1)$$

where a and c are constants that can be derived from linear regression on measured CO₂ emission datasets. In the power-law assumption, the global volcanic CO₂ flux (f_{tot}) was extrapolated to 88-132 Mt/yr (Brantley and Koepenick 1995) using the relation:

$$f_{tot} = f_1 + f_2 + f_3 + f_N \left[\frac{c}{1-c} (N+1) \left(\frac{N}{N+1} \right)^{\frac{1}{c}} \right] \quad (6.2)$$

where f_N refers to the Nth-largest measured flux. This 88-132 Mt/yr estimate is a factor 2-3 lower than obtained with the linear extrapolation technique (Burton et al. 2013). On the same basis, the volcanic+metamorphic CO₂ flux was evaluated at ~264 Mt/yr (Brantley and Koepenick 1995).

The power-law distribution assumption has extensively been used to extrapolate volcanic gas fluxes at both global and individual-arc scale (Hilton et al. 2002). However, concerns have recently been raised on its validity. For example, Mori et al. (2013) demonstrated that the SO₂ flux distribution of Japanese volcanoes noticeably diverges from a simple power law distribution. The case of the global volcanic CO₂ flux population is illustrated in Figure 6.1. The figure is a log-log plot of the cumulative number of volcanoes (N) having measured CO₂ flux of $\geq f$. The diagram is based upon the dataset of Burton et al. (2013), implemented with the results from this study (Table 6.1) and additional data for Turrialba (1140 tons/day; Conde et al. 2014) and Poas (24.7 tons/day; Aiuppa et al. 2014) in Costa Rica, Telica (132 tons/day; Conde et al. 2014) and San Cristobal (523 tons/day; Aiuppa et al. 2014) in Nicaragua, Lastarria (973 tons/day) and Láscar (534 tons/day) in Chile (Tamburello et al. 2013; 2014), and Soufriere in Guadeloupe (14.9 tons/day; Allard et al. 2014). This implemented CO₂ flux population (47 volcanoes in total) clearly departs from a linear trend, as would be expected for a power-law distribution (Eq. 6.1). The observed distribution shows, instead, a clear inflection point at $\log f \sim 2.5-2.8$ (e.g., CO₂ flux of ~ 300-600 tons/day), which appears to divide high (>600 tons/day) from low (<300 tons/day) CO₂ flux volcanoes (L and H regression lines in Fig. 6.1).

In view of these novel results (listed in table 6.1), I proposed that the non-linear behavior of the volcanic CO₂ flux population may (at least in part) reflect the scarcity of CO₂ flux information on weakly fuming, quiescent volcanoes (Pedone et al. 2014b). The case Hekla is emblematic in this context: the volcano has remained in a very active state in the last century (it violently erupted only fourteen years ago; Höskuldsson et al. 2007), but shows today no visible plume or gas emission. Yet however, our data suggest the volcano may

contribute daily ~ 15 tons of CO_2 to the atmosphere in invisible, but probably persistent form. Similarly, no plume is seen on top of Nea Kameni in Santorini, which weak fumaroles yet release 63 ± 22 tons of CO_2 every day (in addition to a sizeable diffuse contribution from the soil), and 5.7 ± 0.9 tons of CO_2 are released daily by quiet hydrothermal activity at Krýsuvík (which most recent activity probably dates back the 14th century; Smithsonian Institution 2013). While the individual contribution of each of the above volcanoes is negligible globally, the cumulative contribution of all feebly degassing volcanoes on Earth may not, and may impact the global CO_2 flux distribution of Figure 6.1.

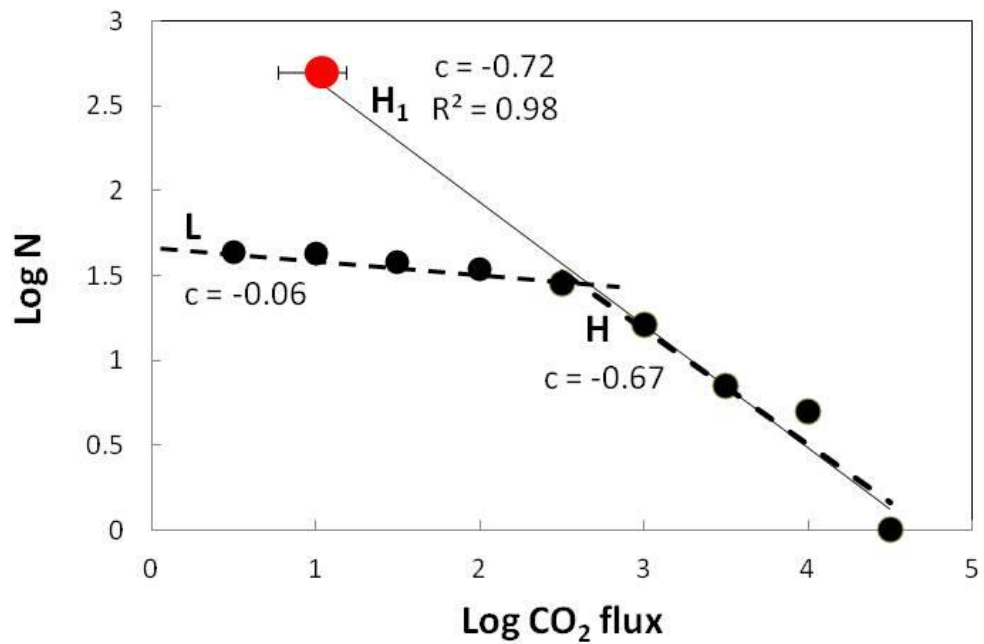


Fig. 6.1 Cumulative frequency of the number of volcanoes (N) emitting CO_2 flux $\geq f$ (in logarithmic scale). The diagram is based upon the dataset of Burton et al. (2013), implemented with new results from this study and additional data (see text). Red point, with coordinates $\log f = 1$ (CO_2 flux = 10 tons/day) and $\log N = 2.69$ (500 volcanoes), lies right above the linear regression line of the high CO_2 flux ($\log f > 2.5$) population (dashed line H). The regression line (line H_1 ; $R^2 = 0.98$) is obtained considering the high CO_2 flux volcanoes ($\log f \geq 2.5$) plus this new $\log f = 1$ point.

To explore the latter argument further, I consider that, of the 1549 volcanic structures listed in the GVP catalogue, around 500 are considered to have been active in the Holocene (Smithsonian Institution 2013), and thus still potentially degassing. For the sake of illustration, I assume that all such 500 volcanoes have a CO_2 flux equal to or higher than 10 tons/day (a flux value close to the weakly degassing investigated systems). This yields to a new point in Figure 6.1, with coordinates $\log f = 1$ (CO_2 flux = 10 tons/day) and $\log N = 2.69$ (500 volcanoes), which lies right above the linear regression line of the high CO_2

flux ($\log f > 2.5$) population (see dashed line H in Figure 6.1). The regression line (line H₁; $R^2 = 0.98$) obtained considering the high CO₂ flux volcanoes ($\log f \geq 2.5$) plus this new $\log f = 1$ point has slope $c = -0.72$. Using this value in relation (6.2), and with $N = 500$, we calculated an extrapolated CO₂ flux of 65.5 Mt/yr.

From these preliminary calculations, it possible to conclude that (i) the power-law distribution may be an appropriate representation of the population of CO₂ flux data, provided the output of the several hundreds of weakly degassing, quiescent/hydrothermal/dormant volcanoes is considered; (ii) a large number of volcanoes remain to be measured, possibly being characterized by intermediate CO₂ output ($\log f$ between 1 and 2.5 in Fig. 6.1) (Pedone et al. 2014b).

Chapter 7

Conclusions

In this thesis, the fumarolic CO₂ output from quiescent volcanoes in hydrothermal state of activity, were investigated using an Infra Red TDL. At each of the studied volcanoes, the acquired TDL results have been used to contour CO₂ mixing ratios in the plumes' cross-sections, and from this to quantifying the fumarolic CO₂ output. All these results show promise for the application of TDLS to volcanic gas research. Based on experiments, It can be concluded that commercially available IR laser systems can easily resolve volcanic CO₂ over the atmospheric background, at least for measurement distances of <350 m.

The TDL measurements reported here contribute new information on Campi Flegrei, Hekla, Krýsuvík, Nea Kameni, La Fossa of Vulcano, and Furnas. The estimated fluxes (Table 6.1) confirm a significant contribution of fumaroles to the total CO₂ budget of such areas.

The highest outputs (524 ± 108 tons/day) are obtained at La Fossa of Vulcano Island, and Campi Flegrei (with an average total CO₂ emission of 487 tons/day from the both investigated fumarolic fields). The lowest CO₂ output (5.7 ± 0.9 tons/day) is associated with hydrothermal activity at Krýsuvík, with intermediate emissions at Hekla (15 ± 7 tons/day), Furnas Village (25.5 ± 10 tons/day), Furnas Lake (35 ± 3.1 tons/day) and Nea Kameni (63 ± 22 tons/day).

Krýsuvík, Hekla and Nea Kameni volcanoes currently display weak exhalative activity and no visible plume emission. We therefore suggest that a 5.7-63 tons/day CO₂ output range may be characteristic of many of the ~ 500 volcanoes active in the Holocene, this in spite the majority lack obvious surface manifestations of degassing. Assuming a representative CO₂ output of 10 tons/day for such 500 Holocene volcanoes, I argue that the global population of CO₂ emissions may approach a simple power-law distribution.

Acknowledgments

The research leading to these results has received funding from contract V2_01 (Progetto V2 “Precursori”; DPC-INGV research agreement 2012-2013), from Miur (PRIN 2009; PI M.V.), from the European Research Council under the European Union’s Seventh Framework Programme (FP7/2007/2013)/ERC grant agreement n1305377 (PI, Alessandro Aiuppa) and from the FP7 grant "Futurevolc".

I would like to acknowledge technical assistance from Boreal Laser Inc. in particular Michael Sosef, who helped me in many ways in setting up the instruments. I also acknowledge IMO (Icelandic Meteorological Office), INGV (Istituto Nazionale di Geofisica e Vulcanologia) and University of Azores (in Ponta Delgada - São Miguel) staff.

Many thanks to the thesis-referees: Dr. Tobias Fischer and Dr. Patrick Allard who provided useful suggestions. I would like to acknowledge all persons who supported me during the field campaigns and PhD period. I would to acknowledge Ing. Gaetano Giudice (from INGV-Palermo) for the kind collaboration during fieldworks, and for the realization of Matlab routine usefull for the tomographic post-processing of datasets. A special acknowledgment to my supervisor, Prof. Alessandro Aiuppa (from DiSTeM-University of Palermo) who believed in me, providing this once-in-a-lifetime opportunity.

References

Aiuppa A, Burton M, Muré F, Inguaggiato S (2004) Intercomparison of volcanic gas monitoring methodologies performed on Vulcano Island, Italy. *Geophys Res Lett* 31. L02610. doi:10.1029/2003GL018651

Aiuppa A, Federico C, Giudice G, Gurrieri S (2005) Chemical mapping of a fumarolic field: La Fossa Crater, Vulcano Island (Aeolian Islands, Italy). *Geophys Res Lett* 32. doi:10.1029/2005GL023207

Aiuppa A, Federico C, Giudice G, Gurrieri S, Valenza M (2006) Hydrothermal buffering of the SO₂/H₂S ratio in volcanic gases: Evidence from La Fossa Crater fumarolic field, Vulcano Island. *Geophys Res Lett* 33. doi:10.1029/2006GL027730

Aiuppa A, Moretti R, Federico C, Giudice G, Gurrieri S, Liuzzo M, Papale P, Shinohara H, Valenza M (2007) Forecasting Etna eruptions by real-time observation of volcanic gas composition. *Geology* 35:1115-1118. doi:10.1130/G24149A.1

Aiuppa A, Giudice G, Gurrieri S, Liuzzo M, Burton M, Caltabiano T, McGonigle AJS, Salerno G, Shinohara H, Valenza M (2008) Total volatile flux from Mount Etna. *Geophys Res Lett* 35. L24302. doi:10.1029/2008GL035871

Aiuppa A, Bertagnini A, Métrich N, Moretti R, Di Muro A, Liuzzo M, Tamburello G (2010) A model of degassing for Stromboli volcano. *Earth and Planetary Science Letters* 295:195-204

Aiuppa A, Tamburello G, Di Napoli R, Cardellini C, Chiodini G, Giudice G, Grassa F, Pedone M (2013) First observations of the fumarolic gas output from a restless caldera: Implications for the current period of unrest (2005-2013) at Campi Flegrei. *Geochemistry Geophysics Geosystems*. doi: 10.1002/ggge.20261

Aiuppa A, Robidoux P, Tamburello G, Conde V, Galle B, Avaré G, Bagnato E, De Moor M, Martínez M, Muñoz A (2014) The Costa Rica-Nicaragua volcanic segment: along-arc variations in volcanic gas chemistry and an improved CO₂ budget. *EPSL* 406:134-147

Allard P et al. (1991) Eruptive and diffuse emissions of CO₂ from Mount Etna. *Nature* 351: 387– 391

Allard P, Burton M, Muré F (2005) Spectroscopic evidence for lava fountain driven by previously accumulated magmatic gas. *Nature* 433: 407-410

Allard P, Aiuppa A, Beauducel F, Calabrese S, Di Napoli R, Gaudin D, Crispi O, Parello F, Hammouya G, Tamburello G (2014) Steam and gas emission rate from La Soufriere volcano, Guadeloupe (Lesser Antilles): implications for the magmatic supply during degassing unrest. *Chem Geol* 384:76-93

Badalamenti B, Chiodini G, Cioni R, Favara R, Francofonte S, Gurrieri S, Hauser S, Inguaggiato S, Italiano F, Magro G, Nuccio PM, Parello F, Pennisi M, Romeo L, Sortino F, Valenza M, Vurro F (1991) Special field workshop at Vulcano (Aeolian Islands) during summer 1998: geochemical result. *Acta Vulcanol* 1:223-227

Baubron JC, Baxter P, Coutinho R, Allard P, Ferreira T, Gaspar JL (1994) Methodology for the drawing up of the Furnas Gas Hazard Map. In Barberi F, Casale R, Fratta M (Eds.): *The European laboratory volcanoes, Workshop Proceedings*, Catania, pp:262–267

Baxter P, Baubron JC, Coutinho R (1999) Health hazards and disaster potential of ground gas emissions at Furnas Volcano, São Miguel, Azores. , *Journal of Volcanology and Geothermal Research* 92:95–106

Beier C, Turner S, Plank T, White W (2010) A preliminary assessment of the symmetry of source composition and melting dynamics across the Azores plume. *Geochemistry Geophysics Geosystems* 11(2), Q02004.doi: 10.1029/2009GC002833

Belotti C, Cuccoli F, Facheris L, Vaselli O (2003) An application of tomographic reconstruction of atmospheric CO₂ over a volcanic site based on open-path IR laser measurements. *IEEE Transaction on geoscience and remote sensing* 41(11)

Bond A, Sparks RSJ (1976) The Minoan eruption of Santorini, Greece. *J Geol Soc London*, 132:1-16

Bonafede M, Mazzanti M (1998) Modelling gravity variations consistent with ground deformation in the Campi Flegrei caldera (Italy). *J Volcanol Geotherm Res* 81:137-157

Boreal Laser Inc. (2007) GasFinder 2.0 portable system. Operation Manual

Brantley SL and Koepenick KW (1995) Measured carbon dioxide emissions from Oldoinyo Lengai and showed distribution of passive volcanic fluxes. *Geology* 23: 933-936

Brusca L, Inguaggiato S, Longo M, Madonna P, Maugeri R (2004) The 2002-2003 eruption of Stromboli (Italy): Evaluation of the volcano activity by means of continuous monitoring of soil temperature, CO₂ flux, and meteorological parameters. *Geochem Geophys Geosyst* 5.doi:10.1029/2004GC000732

Burton MR, Oppenheimer C, Horrocks LA, Francis PW (2000) Remote sensing of CO₂ and H₂O emissions from Masaya Volcano, Nicaragua, by Fourier transform spectrometry. *Geology* 28:915-918

Burton MR, Mader HM, Polacci M (2007) The role of gas percolation in quiescent degassing of persistently active basaltic volcanoes. *Earth and Planetary Science Letters* 264:46-60

Burton MR, Sawyer GM, Granieri D (2013) Deep Carbon Emissions from Volcanoes. *Reviews in Mineralogy and Geochemistry* 75:323-354. doi: 10.2138/rmg.2013

Caltabiano T, Burton M, Giammanco S, Allard P, Bruno N, Muré F, Romano R (2004) Volcanic gas emissions from the summit craters and flanks of Mt. Etna, 1987–2000, in *Mt. Etna: Volcano Laboratory. Geophys Monogr Ser 143*, edited by A. Bonaccorso et al., pp. 111– 128, AGU, Washington, DC

Capasso G, Favara R, Inguaggiato S (1997) Chemical features and isotopic composition of gaseous manifestations on Vulcano Island (Aeolian Islands, Italy): an interpretative model of fluid circulation. *Geochim Cosmochim Acta* 61:3425-3440

Capasso G, Favara R, Francofonte S, Inguaggiato S (1999) Chemical and isotopic variations in fumarolic discharge and thermal waters at Vulcano Island (Aeolian Islands, Italy) during 1996: evidence of resumed volcanic activity. *J Volcanol Geoth Res* 88:167-175

Carapezza ML, Inguaggiato S, Brusca L, Longo M (2004) Geochemical precursors of the activity of an open-conduit volcano: The Stromboli 2002-2003 eruptive events. *Geophys Res Lett* 31. doi:10.1029/2004GL019614

Cardellini C, Chiodini G, Frondini F (2003) Application of stochastic simulation to CO₂ flux from soil: Mapping and quantification of gas release. *J Geophys Res* 108. doi:10.1029/2002JB002165

Cerling TE, Solomon DK, Quade J, Bowman JR (1991) On the isotopic composition of carbon in soil carbon dioxide. *Geochim Cosmochim Acta* 55: 3403-3405

Chiodini G, Cioni R, Marini L, Panichi C (1995) Origin of the fumarolic fluids of Vulcano Island, Italy and implications for volcanic surveillance. *Bull Volcanol* 57:99-110

Chiodini C, Frondini F, Raco B (1996a) Diffuse emission of CO₂ from the Fossa crater, Vulcano Island (Italy). *Bull Volcanol* 58:41-50

Chiodini G, D'Alessandro W, Parello F (1996b) Geochemistry of gases and waters discharged by the mud volcanoes at Paternò, Mt. Etna (Italy). *Bull Volcanol* 58:51-58

Chiodini C, Cioni R, Guidi M, Raco B, Marini L (1998) Soil CO₂ flux measurements in volcanic and geothermal areas. *Appl Geochem* 13:543-552

Chiodini G, Frondini F, Cardellini C, Granieri D, Marini L, Ventura G (2001) CO₂ degassing and energy release at Solfatara Volcano, Campi Flegrei, Italy. *J Geophys Res* 106:16,213–16,221

Chiodini G, Todesco M, Caliro S, Del Gaudio C, Macedonio G, Russo M (2003) Magma degassing as a trigger of bradyseismic events; the case of Phlegrean Fields (Italy). *Geophys Res Lett* 30(8):1434. doi: 10.1029/2002GL01679

Chiodini G, Granieri D, Avino R, Caliro S, Costa A, Werner C (2005) Carbon dioxide diffuse degassing and estimation of heat release from volcanic and hydrothermal systems. *J Geophys Res.* doi:10.1029/2004JB003542

Chiodini G, Caliro S, Cardellini C, Granieri D, Avino R, Baldini A, Donnini M, Minopoli C (2010) Long-term variations of the Campi Flegrei, Italy, volcanic system as revealed by the monitoring of hydrothermal activity. *J Geophys Res* 115, B03205. doi : 10.1029/2008JB006258

Chiodini G, Caliro S, De Martino P, Avino R, Ghepardi F (2012) Early signals of new volcanic unrest at Campi Flegrei caldera? Insights from geochemical data and physical simulations. *Geology* 40:943-946

Clifton AE and Schlische RW (2003) Fracture populations on the Reykjanes Peninsula, Iceland: comparison with experimental clay models of oblique rifting. *J Geophys Res* 108:2074

Cole P, Queiroz G, Wallenstein N, Gaspar JL, Duncan AM, Guest J (1995) An historic subplinian/phreatomagmatic eruption: the 1630 AD eruption of Furnas Volcano, São Miguel, Azores. *Journal of Volcanology and Geothermal Research* 69:117–135

Conde V, Robidoux P, Avard G et al. (2014) Measurements of SO₂ and CO₂ by combining DOAS, Multi-GAS and FTIR: Study cases from Turrialba and Telica volcanoes. *International Journal of Earth Sciences*, in press, doi:10.1007/s00531-014-1040-7

Cropper WPJr, Ewel KC, Raich JW (1985) The measurement of soil CO₂ evolution in situ. *Pedobiologia* 28:35-40

Cruz JV, Coutinho R, Carvalho MR, Óskarsson N, Gislason SR (1999) Chemistry of waters from Furnas Volcano, São Miguel, Azores: Fluxes of volcanic carbon dioxide and leached material. *J Volcanol Geotherm Res* 92:151–167

Cumin G (1954) Le Salinelle di Paternò e la loro attuale attività. *Bollettino dell'Accademia Gioenia di Scienze Naturali, Catania*, IV 2(9):515-528

D'Alessandro W, De Gregorio S, Dongarrà G, Gurrieri S, Parello F, Parisi B (1997) Chemical and isotopic characterization of the gases of Mount Etna (Italy). *Journal of Volcanology and Geothermal Research* 78(1–2):65-76

Daag AS, Dolan MT, Laguerta EP, Meeker GP, Newhall CG, Pallister JS, Solidum RU (1996) Monitoring sulphur dioxide emissions at Mount Pinatubo, in *Fire and Mud: Eruptions and Lahars of Mount Pinatubo, Philippines*, edited by Newhall CG and Punongbayan RS, pp. 647– 664. Philip Inst of Volcanol and Seismol, Quezon City, Philippines

Del Gaudio C, Aquino I, Ricciardi GP, Ricco C, Scandone R (2010) Unrest episodes at Campi Flegrei: A reconstruction of vertical ground movements during 1905–2009. *J Volcanol Geotherm Res* 195:48-56

De Natale P, Gianfrani L, De Natale G, Cioni R (1998) Gas concentration measurements with DFB lasers to monitor volcanic activity *SPIE Proceedings Series. Applications of Photonic Technology-3* 3491:783-787

De Natale P, Gianfrani L, De Natale G (2001) Optical methods for monitoring of volcanoes: techniques and new perspectives. *J Volcanol Geotherm Res* 109:235-245

- De Rosa M, Gagliardi G, Rocco A, Somma R, De Natale P, De Natale G (2007) Continuous in situ measurements of volcanic gases with a diode-laser-based spectrometer: CO₂ and H₂O concentration and soil degassing at Vulcano (Aeolian islands: Italy). *Geochemical Transactions*. doi:10.1186/1467-4866-8-5
- Di Vito MA, Isaia R, Orsi G, Southon J, De Vita S, D'Antonio M, Pappalardo L, Piochi M (1999) Volcanism and deformation since 12,000 years at the Campi Flegrei caldera (Italy). *J Volcanol and Geotherm Res* 91: 221-246
- Diliberto IS, Gurrieri S, Valenza M (2002) Relationships between diffuse CO₂ emissions and volcanic activity on the island of Vulcano (Aeolian Islands, Italy) during the period 1984–1994. *Bull Volcanol* 64:219–228. doi 10.1007/s00445-001-0198-6
- Dimitriadis I, Karagianni E, Panagiotopoulos D, Papazachos C, Hatzidimitriou P, Bohnhoff M, Rische M, Meier T (2009) Seismicity and active tectonics at Coloumbo Reef (Aegean Sea, Greece): monitoring an active volcano at Santorini Volcanic Center using a temporary seismic network. *Tectonophysics* 465:136–149
- Dominey-Howes D and Minos-Minopoulos D (2004) Perceptions of hazard and risk on Santorini. *J Volcanol Geotherm Res* 137:285-310
- Druitt TH, Edwards L, Mellors RM, Pyle DM, Sparks RSJ, Lanphere M, Davies M, Barreiro B (1999) Santorini Volcano. Geological Society, London, Memoirs 19
- Edmonds M, Oppenheimer C, Pyle DM, Herd RA, Thompson G (2003) SO₂ emissions from Soufriere Hills volcano and their relationship to conduit permeability, hydrothermal interaction and degassing regime. *J Volcanol Geotherm Res* 124: 23– 43
- Edwards NT (1982) The use of soda-lime for measuring respiration rates in terrestrial systems. *Pedobiologia* 23:321-330
- Favara R, Giammanco S, Inguaggiato S, Pecoraino G (2001) Preliminary estimate of CO₂ output from Pantelleria Island volcano (Sicily, Italy): Evidence of active mantle degassing. *Appl Geochem* 16:883-894

Federico C, Giudice G, Liuzzo M, Pedone P, Cosenza P, Riccobono G (2014) First measurements of gas output from bubbling pools in a mud volcano at the periphery of Mt Etna (Italy): methodologies and implications for monitoring. EGU2014-14948, EGU General Assembly, Wien

Ferreira T (1994) Contribuição para o estudo das emissões gasosas associadas a processos de vulcanismo no arquipélago dos Açores. Unpublished Master Thesis, University of the Azores, p.183, (in Portuguese)

Ferreira T and Oskarsson N (1999) Chemistry and isotopic composition of fumarole discharges of Furnas caldera. *Journal of Volcanology and Geothermal Research* 92:169–179

Ferreira T, Gaspar JL, Viveiros F, Marcos M, Faria C, Sousa F (2005) Monitoring of fumarole discharge and CO₂ soil degassing in the Azores: contribution to volcanic surveillance and public health risk assessment. *Annals of Geophysics* 48(4–5):787–796

Fischer TP (2008) Fluxes of volatiles (H₂O, CO₂, N₂, Cl, F) from arc volcanoes. *Geochem J* 42(1):21-38

Fytikas M, Kolios N, Vougioukalakis G (1990) Post- Minoan volcanic activity on the Santorini volcano. Volcanic hazards and risk, forecasting possibilities. In: Hardy DA, Keller J, Galanopoulos VP, Flemming NC, Druitt TH (Eds.) *Thera and the Aegean World III*, Earth Sciences, vol. 2. The Thera Foundation, London, pp. 183– 198

Francis PW, Burton M, Oppenheimer C (1998) Remote measurements of volcanic gas compositions by solar FTIR spectroscopy. *Nature* 396:567-570

Gagliardi G, Restieri R, De Biasio G, De Natale P, Cotrufo F, Gianfrani L (2001) Quantitative diode laser absorption spectroscopy near 2 μm with high precision measurements of CO₂ concentration. *Rev Sci Inst* 72:4228-4233

Gagliardi G, Restieri R, Casa G, Gianfrani L (2002) Chemical and isotopic analysis using diode laser spectroscopy: applications to volcanic gas monitoring. *Optics and Lasers in Engineering* 37:131-142

Gagliardi G, Castrillo A, Iannone RQ, Kerstel ERT, Gianfrani L (2003) High-precision of the $^{13}\text{CO}_2/^{12}\text{CO}_2$ isotope ratio using a portable 2.008- μm diode-laser spectrometer. *Appl Phys B* 77:119-124. doi: 10.1007/s00340-003-1240-5

Galle B, Oppenheimer C, Geyer A, McGonigle AJS, Edmonds M, Horrocks L (2003) A miniaturised ultraviolet spectrometer for remote sensing of SO_2 fluxes: a new tool for volcano surveillance. *J Volcanol Geotherm Res* 119:241-254

Gaspar JL, Ferreira T, Queiroz G, Wallenstein N, Pacheco J, Guest J, Duncan AM, Cole P (1995) Evolução morfoestrutural do Vulcão das Furnas (ilha de S. Miguel, Açores) (in Portuguese). *Mem Mus Lab Mineral Geol Fac Cienc Univ, Porto*, 4:999–1003

Gianfrani L, Gagliardi G, Pesce G, Sasso A (1997a) High sensitivity detection of NO_2 by using a 740nm semiconductor diode laser. *Appl Phys B* 64:487

Gianfrani L, Gabrysch M, Corsi C, De Natale P (1997b) Detection of H_2O and CO_2 with distributed feedback diode lasers: measurement of broadening coefficients and assessment of the accuracy levels for volcanic monitoring. *Appl Opt* 36:9481-9486

Gianfrani L, De Natale P, De Natale G (2000) Remote sensing of volcanic gases with a DFB-laser-based fiber spectrometer. *Appl Phys B-Rapid Commun* 70:467-470

Giggenbach WF (1975) A simple method for the collection and analysis of volcanic gas samples. *Bull Volcanol* 39:132–145

Giggenbach WF (1996) Chemical composition of volcanic gases in Monitoring and Mitigation of Volcanic Hazards. In Scarpa R, Tilling RI (Eds). Springer, Berlin, pp 221-256

Gurrieri S. and Valenza M. (1988) Gas transport in natural porous mediums: a method for measuring CO_2 flows from the ground in volcanic and geothermal areas. *Rend Soc Ital Mineral Petrologia* 43:1151-1158

Hernández PA, Notsu K, Salazar JM, Mori T, Natale G, Okada H, Virgili G, Shimoike Y, Sato M, Pèrez NM (2001) Carbon dioxide degassing by advective flow from Usu volcano, Japan. *Science* 292:83-86

Herzberg G (1991) *Molecular Spectra and Molecular Structure II: Infrared and Raman Spectra of Polyatomic Molecules*. Krieger Publishing Company. Reprint Edition

Hilton DR, Fisher TP, Marty B (2002) Noble gases and volatile recycling at subduction zones. *Rev Mineral Geochem* 47:319-370

Höskuldsson Á, Óskarsson N, Pedersen R, Grönvold K, Vogfjörð K, Ólafsdóttir R (2007) The millennium eruption of Hekla in February 2000. *Bull Volcanol* 70:169-182. doi:10.1007/s00445-007-0128-3

Humphries SD, Nehir AR, Keith CJ, Repasky KS, Dobeck LM, Carlsten JL, Spangler LH (2008) Testing carbon sequestration site monitor instruments using a controlled carbon dioxide release facility. *Applied Optics* 47:548-555

Ilyinskaya E, Aiuppa A, Bergsson B, Di Napoli R, Fridriksson T, Ólafsdóttir AA, Óskarsson F, Grassa F, Pfeffer M, Lechner K, Yeo R, Giudice G (2014) Degassing regime of Hekla volcano 2012-2013. *Geochimica et Cosmochimica Acta*, accepted

Inguaggiato S, Martin-Del Pozzo AL, Aguayo A, Capasso G, Favara R (2005) Isotopic, chemical and dissolved gas constraints on spring water from Popocatepetl (Mexico): Evidence of gas-water interaction magmatic component and shallow fluids. *J Volcanol Geotherm Res* 141:91-108

Inguaggiato S, Vita F, Rouwet D, Bobrowski N, Morici S, Sollami A (2011) Geochemical evidence of the renewal of volcanic activity inferred from CO₂ soil and SO₂ plume fluxes: The 2007 Stomboli eruption (Italy). *Bull Volcanol* 73:443-456

Inguaggiato S, Mazot A, Diliberto IS, Inguaggiato C, Madonia P, Rouwet D, Vita F (2012) Total CO₂ output from Vulcano island (Aeolian Islands, Italy). *Geochemistry Geophysics Geosystems*. doi:10.1029/2011GC003920

Isaaks EH and Srivastava RM (1989) *An Introduction to Applied Geostatistics*, Oxford University Press, New York, pp 561

ISMOSAV (2009) Website of the Institute for the Study and Monitoring of the Santorini Volcano, <http://ismosav.santorini.net/>

Jakobsson SP (1979) Petrology of recent basalts from the eastern volcanic zone, Iceland. *Acta Nat Isl* 26:1–103

Jónsson J (1978) *Geological Map of the Reykjanes Peninsula*. Reykjavik Energy Authorities, OS-JHD-7831

Kanemasu ET, Powers WL, Sij JW (1974) Field chamber measurements of CO₂ flux from soil surface. *Soil Science* 118:233-237

Keller J (1980) The island of Vulcano. *Rend Soc Ital Mineral Petrol* 36:369–414

Khristenko SV, Maslov AI, Shevelko VP (1998) *Molecules and Their Spectroscopic Properties*. Springer Series on Atomic Optical and Plasma Physics

Kinzig AP and Socolow RH (1994) Human impact on the nitrogen cycle. *Physics Today* 47(11):24-31

Kucera CL and Kirkham DR (1971) Soil respiration studies in tallgrass prairie in Missouri. *Ecology* 52:912-915

Larsen G, Dugmore AJ, Newton AJ (1999) Geochemistry of historical-age silicic tephra in Iceland. *The Holocene* 9:463-471

Lieth H and Ouellette R (1962) Studies on the vegetation of the Gaspé Peninsula. II. The soil respiration of some plant communities. *Can J Bot* 40:127-140

Linnerud I, Kaspersen P, Jæger T (1998) Gas Monitoring in the process industry using diode laser spectroscopy. *Appl Phys B* 67:297-305

Marinatos S (1939) The volcanic destruction of Minoan Crete. *Antiquity* 13:425– 439

Markússon SH and Stefánsson A (2011) Geothermal surface alteration of basalts, Krýsuvík Iceland-Alteration mineralogy, water chemistry and the effects of acid supply on the alteration process. *J Volcanol Geoth Res* 206:46-59

Marret R and Almendinger RW (1991) Estimates of strain due to brittle faulting: Sampling of fault populations *Journal of Structural Geology* 13:735-738

Mazot A, Rouwet D, Taran Y, Inguaggiato S, Varley N (2011) CO₂ and He degassing at El Chichón volcano (Chiapas, Mexico): Gas flux, origin, and relationship with local and regional tectonics. *Bull Volcanol* 73:423-441. doi:10.1007/s00445-010-0443-y

McCoy FW, Heiken G (2000) The Late-Bronze age explosive eruption of Thera (Santorini), Greece: regional and local effects. *Geological Society of America Special Paper* 345:43– 70

McGonigle AJS, Aiuppa A, Giudice G, Tamburello G, Hodson AJ, Gurrieri S (2008) Unmanned aerial vehicle measurements of volcanic carbon dioxide fluxes. *Geophys Res Lett* 35:L06303. doi:10.1029/2007GL032508

Millan MM, Gallant AJ, Chung YS, Fanaki F (1985) COSPEC observation of Mt. St. Helens volcanic SO₂ eruption cloud of 18 may 1980 over Southern Ontario. *Atmospheric Environment* 19:255-263

Moore R (1990) Volcanic geology and eruption frequency, São Miguel, Azores. *Bulletin of Volcanology* 52:602–614

Mori T, Notsu K, Tohjima Y, Wakita H, Nuccio PM, Italiano F (1995) Remote detection of fumarolic gas chemistry at Vulcano, Italy, using an FT-IR spectral radiometer. *Earth Planet Sci Lett* 134:219–224. doi:10.1016/0012- 821X(95)00119-W

Mori T, Hernández PA, Salazar JML, Pérez MM, Notsu K (2001) An in situ method for measuring CO flux from volcanic-hydrothermal fumaroles. *Chemical Geology* 177:85–99

Mori T, Shinohara H, Kazahaya K, Hirabayashi J, Matsushima T, Mori T, Ohwada M, Odai M, Iino H, Miyashita M. (2013) Time-averaged SO₂ fluxes of subduction-zone volcanoes: Example of a 32-year exhaustive survey for Japanese volcanoes. *Journal of Geophysical Research* 118:8662-8674

Moune S, Sigmarsson O, Thordarson T, Gauthier PJ (2007) Recent volatile evolution in the magmatic system of Hekla volcano, Iceland. *Earth and Planetary Science Letters* 255:373–389

Newman AV, Stiros S, Feng L, Psimoulis P, Moschas F, Saltogianni V, Jiang Y, Papazachos C, Panagiotopoulos D, Karagianni E, Vamvakaris D (2012) Recent geodetic unrest at Santorini Caldera, Greece. *Gephys Res Lett* 39.doi:10.1029/2012GL051286

Oppenheimer C, Bani P, Calkins JA, Burton MR, Sawyer GM (2006) Rapid FTIR sensing of volcanic gases released by Strombolian explosions at Yasur volcano, Vanuatu. *Appl Phys B* 85:2 – 3. doi:10.1007/s00340-006-2353-4

Oppenheimer C, Lomakina A, Kyle PR, Kingsbury NG, Boichu M (2009) Pulsatory magma supply to a phonolite lava lake. *Earth Planet Sci Lett* 284:392-398

Oppenheimer C (2010) Ultraviolet sensing of volcanic sulfur emissions. *Elements* 6:87–92

Oppenheimer C, Moretti R, Kyle PR, Eschenbacher A, Lowenstern JB, Hervig RL, Dunbar NW (2011) Mantle to surface degassing of alkalic magmas at Erebus volcano, Antarctica. *Earth Planet Sci Lett* 306:261-271

Orsi G, De Vita S, Di Vito M (1996) The restless, resurgent Campi Flegrei nested caldera (Italy): constraints on its evolution and configuration. *J Volcanol Geotherm Res* 74:179–214

Orsi G, Di Vito MA, Isaia R (2004) Volcanic hazard assessment at the restless Campi Flegrei caldera. *Bull Volcanol* 66:514-530

Orsi G, Di Vito MA, Selva J, Marzocchi W (2009) Long-term forecast of eruptive style and size at Campi Flegrei caldera (Italy). *Earth Planet Sci Lett* 287:265-276

Oskarsson N, Pálsson K, Ólafsson H, Ferreira T (1999) Experimental monitoring of carbon dioxide by low power IR-sensors: soil degassing in the Furnas Volcanic Centre, Azores. *Journal of Volcanology and Geothermal Research* 92:181–193

Paonita A, Favara R, Nuccio PM, Sortino F (2002) Genesis of fumarolic emissions as inferred by isotope mass balances: CO₂ and water at Vulcano Island, Italy. *Geochim Cosmochim Acta* 66:759–772

Paonita A, Caracausi A, Iacono-Marziano G, Martelli M, Rizzo A (2012) Geochemical evidence for mixing between fluids exsolved at different depths in the magmatic system of Mt. Etna (Italy). *Geochim Cosmochim Acta* 84:380-394

Papazachos BC, Dimitriadis ST, Panagiotopoulos DG, Papazachos CB, Papadimitriou EE (2005) Deep structure and active tectonics of the southern Aegean volcanic arc. *Developments in Volcanology* 7:47-64

Parkinson KJ (1981) An improved method for measuring soil respiration in the field. *Journal of Applied Ecology* 18:221-228

Parks MM, Biggs J, England P, Mather TA, Nomikou P, Palamartchouk K, Papanikolaou X, Paradissis D, Parsons B, Pyle DM, Raptakis C, Zacharis V (2012) Evolution of Santorini volcano dominated by episodic and rapid fluxes of melt from depth. *Nat Geosci* 5:749-754

Parks MM, Caliro S, Chiodini G, Pyle DM, Mather TA, Berlo K, Edmonds M, Biggs J, Nomikou P, Raptakis C (2013) Distinguishing contributions to diffuse CO₂ emissions in volcanic areas from magmatic degassing and thermal decarbonation using soil gas ²²²Rn– $\delta^{13}\text{C}$ systematics: Application to Santorini volcano, Greece. *Earth and Planetary Science Letters* 377–378:180-190

- Pavlidis SB and Valkaniotis S (2003) Tectonic regime of Santorini–Amorgos area. Proceedings of International Conference "The South Aegean Active Volcanic Arc: Present Knowledge and Future Perspectives", Milos Island, Greece, p 76
- Pecoraino G, Brusca L, D'Alesandro W, Giammanco S, Inguaggiato S, Longo M (2005) Total CO₂ output from Ischia Island volcano (Italy). *Geochem J* 39:451-458. doi:10.2343/geochemj.39.451
- Pedone M, Aiuppa A, Giudice G, Grassa F, Cardellini C, Chiodini G, Valenza M (2014a) Volcanic CO₂ flux measurement at Campi Flegrei by Tunable Diode Laser absorption Spectroscopy. *Bull Volcanol* 76. doi: 10.1007/s00445-014-0812-z
- Pedone M, Aiuppa A, Giudice G, Grassa F, Francofonte V, Bergsson B, Ilyinskaya E (2014b) Tunable Diode Laser measurements of hydrothermal/volcanic CO₂, and implications for the global CO₂ budget. *Solid Earth* 5:1209-1221. doi:10.5194/sed-5-1209-2014
- Reid J, Schewchun J, Garside BK, Ballik A (1978) High sensitivity Pollution Detection Employing Tunable Diode Lasers. *App Opt* 17:300-307
- Reiners WA (1968) Carbon dioxide evolution from the Floor of three Minnesota forests. *Ecology* 49:471-483
- Richter D, Erdelyi M, Curl RF, Tittel FK, Oppenheimer C, Duffell HJ, Burton M (2002) Field measurements of volcanic gases using tunable diode laser based mid-infrared and Fourier transform infrared spectrometers. *Optics and Lasers in Engineering* 37:171-186
- Rogie JD, Kerrick DM, Sorey ML, Chiodini G, Galloway DL (2001) Dynamics of carbon dioxide emission at Mammoth Mountain, California. *Earth Planet Sci Lett* 188:535–541
- Rosi M, Sbrana A, Principe C (1983) The Phlegrean Fields: Structural evolution, volcanic history and eruptive mechanisms. *J Volcanol Geotherm Res* 17:273-288

Saemundsson K (1979) Outline of the geology of Iceland. *Jökull* 29:7–29

Sawyer GM, Carn SA, Tsanev VI, Oppenheimer C, Burton M (2008) Investigation into magma degassing at Nyiragongo volcano, Democratic Republic of the Congo. *Geochem Geophys Geosyst* 9, Q02017. doi:10.1029/2007GC001829

Schiff HI, Mackay GI, Bechara J (1994a) The Use of Tunable Diode Laser Absorption Spectroscopy for Atmospheric Measurements. *Res Chem Intermed* 20:525-556

Schiff HI, Mackay GI, Bechara J (1994b) The Use of Tunable Diode Laser Absorption Spectroscopy for Atmospheric Measurements. In: Sigrist MW (ed) *Air Monitoring by Spectroscopic Techniques*. Chemical Analysis Series. Wiley, New York, pp. 239-333

Searle R (1980) Tectonic pattern of the Azores spreading centre and triple junction. *Earth and Planetary Science Letters* 51:415–434

Shinohara H, Aiuppa A, Giudice G, Gurrieri S, Liuzzo M (2008) Variation of H₂O/CO₂ and CO₂/SO₂ ratios of volcanic gases discharged by continuous degassing of Mount Etna volcano, Italy. *J Geophys Res* 113, B09203. doi:10.1029/2007JB005185

Shinohara H (2013) Volatile flux from subduction zone volcanoes: Insights from a detailed evaluation of the fluxes from volcanoes in Japan. *J Volcanol Geotherm Res.* 268:46-63

Siebert L and Simkin T (2002) *Volcanoes of the World: An Illustrated Catalog of Holocene Volcanoes and their Eruptions*. Smithsonian Institution Digital Information Series GVP-3, <http://www.volcano.si.edu/world>

Sigmarsson O, Condomines M, Fourcade S (1992) A detailed Th, Sr and O isotope study of Hekla: differentiation processes in an Icelandic volcano. *Contrib Mineral Petrol* 112:20-34

Sigurdsson H, Carey S, Alexandri M, Vougioukalakis G, Croff K, Roman C, Sakellariou D, Anagnostou C, Rousakis G, Ioakim C, Gogou A, Ballas D, Misaridis T, Nomikou P (2006) Marine investigations of Greece's Santorini volcanic field. *Eos* 87 (34):337–339

Silvestri O (1879) Eruzione di fango presso l'Etna. Boll Vulc It 6(1-3):28-31

Smithsonian Institution (2013) http://www.volcano.si.edu/data_criteria.cfm

Stiros SC, Psimoulis P, Vougioukalakis G, Fyticas M (2010) Geodetic evidence and modeling of a slow, small-scale inflation episode in the Thera (Santorini) volcano caldera, Aegean Sea. *Tectonophysics* 494:180–190

Stoer J and Bulirsch R (2002) *Introduction to Numerical Analysis* (3rd ed). Springer-Verlag, Berlin, New York, ISBN 978-0-387-95452-3, p 619

Svanberg S (2002) Geophysical gas monitoring using optical techniques: volcanoes, geothermal fields and mines. *Optics and Lasers in Engineering* 37:245-266

Symonds R, Rose WI, Bluth GJS, Gerlach TM (1994) Volcanic-gas studies: methods, results and applications. In: MR Carroll and JR Halloway (ed) *Volatiles in Magmas*. Mineralogical Society of America, pp.1–66

Tamburello G, Kantzas EP, McGonigle AJS, Aiuppa A, Giudice G (2011) UV camera measurements of fumarole field degassing (La Fossa crater, Vulcano Island). *J Volcanol Geoth Res* 199:47-52

Tamburello G, Hansteen TH, Bredemeyer S, Aiuppa A, Giudice G (2013) Gas fluxes and compositions of two active volcanoes in Northern Chile: Lascar and Lastarria. *American Geophysical Union Fall Meeting 2013*, abstract #V31B-2703

Tamburello G, Hansteen TH, Bredemeyer S, Aiuppa A, Tassi F (2014) Gas emissions from five volcanoes in northern Chile and implications for the volatiles budget of the Central Volcanic Zone. *Geophysical Research Letters* 41(14):4961-4969

Tassi F, Vaselli O, Papazachos C, Giannini L, Chiodini G, Vougioukalakis GE, Karagianni E, Vamvakaris D, Panagiotopoulos D (2013) Geochemical and isotopic changes in the fumarolic and submerged gas discharge during the 2011-2012 unrest at Santorini caldera (Greece). *Bull Volcanol* 75. doi:10.1007/s00445-013-0711-8

Thorarinsson S (1967) The eruption of Hekla 1947-48. Soc Sci Isl 1-183

Trasatti E, Bonafede M, Ferrari C, Giunchi C, Berrino G (2011) On deformation sources in volcanic areas: Modeling the Campi Flegrei (Italy) 1982-84 unrest. Earth Planet Sci Lett 306:175-185

Trottier S, Gunter WD, Kadatz B, Olson M, Perkins EH (2009) Atmospheric Monitoring for the Pembina Cardium CO₂ Monitoring Project using Open Path Laser Technology. Science Direct Energy Procedia 1:2307-2314. doi:10.1016/j.egypro.2009.01.300

Tsapanos TM, Galanopoulos D, Burton PW (1994) Seismicity in the Hellenic Volcanic Arc: relation between seismic parameters and the geophysical fields in the region. Geophys J Int 117:677-694

Tulip J (1997) Gas detector, United States Patent 5,637,872 250/338.5

Turcotte DL (1992) Fractals and chaos in geology and geophysics. Cambridge University Press, pp 52-64

Viveiros F, Cardellini C, Ferreira T, Caliro S, Chiodini G, Silva C (2010) Soil CO₂ emissions at Furnas volcano, São Miguel Island, Azores archipelago: Volcano monitoring perspectives, geomorphologic studies, and land use planning application. J Geophys Res 115, B12208. doi:10.1029/2010JB007555

Viveiros F, Cardellini C, Ferreira T, Silva C (2012) Contribution of CO₂ emitted to the atmosphere by diffuse degassing from volcanoes: The Furnas Volcano case study. Int J Global Warming 4(3-4):287-304

Vougioukalakis GE, Mitropoulos D, Perissoratis C, Andrinopoulos A, Fytikas M (1994) The submarine volcanic centre of Coloumbo, Santorini, Greece. Bull Soc Geol Greece XXX, 3:51-360

Weida MJ (2007) A Brief Comparison of 2f and Broadly Swept Detection Techniques. Daylight Solutions Inc D0084 RevA

Weidmann D, Wysocki G, Oppenheimer C, Tittel FK (2005) Development of a compact quantum cascade laser spectrometer for field measurement of CO₂ isotopes. *Applied Physics B* 80:255-260

Werle P (1998) A review of recent advances in semiconductor laser based gas monitors. *Spectrochim Acta A* 54:197-236

Werle P, Slemr F, Maurer K, Kormann R, Mücke R, Jänker B (2002) Near- and mid-infrared laser-optical sensors for gas analysis. *Optics and Lasers in Engineering* 37:101-114

Werner C and Cardellini C (2006) Comparison of carbon dioxide emissions with fluid upflow, chemistry, and geologic structures at the Rotorua geothermal system, New Zealand. *Geothermics* 35:221-238.doi:10.1016/j.geothermics.2006.02.2006

Yoshimura S and Nakamura M (2013) Flux of volcanic CO₂ emission estimated from melt inclusions and fluid transport modelling. *Earth and Planetary Science Letters* 361:497–503

<http://www.britannica.com/EBchecked/topic/558901/spectroscopy> (Enciclopedia Britannica)

Supplementary Materials

Dataset

The dataset acquired at the different investigated area during the field campaigns (from October 2012 to August 2014) is reported in the next tables (Tabs. from A1 to A13). In the tables, each row refers to a specific laser-mirror open-path configuration. The following parameters are reported in each table:

N: progressive number of the path;

Link L-M: code identifying each GasFinder-retro-reflector path. Letters indicate position of the laser unit and numbers refer to position of the mirrors (e.g.: link “A1” is the open path linking the “A” position of Laser and the “1” position of retro-reflector).

Dist: the optical path length (the distance between the GasFinder unit and the retro-reflector), in metres.

Start time: start-time of data acquisition.

End time: end of data acquisition.

Duration: difference between end and start time.

M: average CO₂ mixing ratio (ppmv).

Dev.Std: standard deviation of CO₂ mixing ratios

Tab. A1: Pisciarelli, 25th October 2012

N	Link L-M	DIST	START TIME	END TIME	DURATION	M	DEV.STD
1	B2	57	10:53:00	10:58:00	00:05:00	879	137.82
2	B1	61	11:03:00	11:10:00	00:07:00	390	85.24
3	B4	55	11:11:00	11:19:00	00:08:00	937	175.09
4	B3	60	11:20:00	11:25:00	00:05:00	708	84.44
5	B5	51.7	11:29:00	11:35:00	00:06:00	829	267.14
6	B6	52	11:41:00	11:47:00	00:06:00	1076	200.43
7	B7	54	11:53:00	11:55:00	00:02:00	579	33.05
8	B8	60	12:02:00	12:06:00	00:04:00	600	255.87
9	A8	69	12:15:00	12:20:00	00:05:00	672	229.74
10	A7	67	12:21:00	12:25:00	00:04:00	601	76.77
11	A6	58	12:28:00	12:33:00	00:05:00	1262	252.02
12	A5	55	12:40:00	13:09:00	00:29:00	776	147.37
13	A4	58	13:13:00	13:17:00	00:04:00	987	300.02
14	A3	62	13:21:00	13:25:00	00:04:00	513	95.12
15	A2	56	13:28:00	13:32:00	00:04:00	569	49.39
16	A1	58	13:34:00	13:37:00	00:03:00	515	23.34
18	C2	62	13:53:00	14:09:00	00:16:00	533	121.03
19	C1	66	14:13:00	14:19:00	00:06:00	480	57.34

20	C3	62	14:23:00	14:28:00	00:05:00	809	189.56
21	C4	56	14:36:00	14:42:00	00:06:00	752	212.50
22	C5	50	14:43:00	14:48:00	00:05:00	780	165.77
23	C6	49	14:50:00	15:00:00	00:10:00	909	129.15
24	C7	51	15:03:00	15:08:00	00:05:00	799	230.46
25	C8	55	15:11:00	15:19:00	00:08:00	1019	178.87
26	D8	48	15:34:00	15:41:00	00:07:00	636	59.46
27	D7	44	15:44:00	15:50:00	00:06:00	1071	100.70
28	D6	44.1	15:53:00	15:58:00	00:05:00	1190	187.28
29	D4	53	16:00:00	16:10:00	00:10:00	1161	216.03
31	D3	61	16:24:00	16:29:00	00:05:00	924	173.98
32	D2	62.5	16:36:00	16:40:00	00:04:00	731	100.89
33	D1	68	16:43:00	16:46:00	00:03:00	561	78.94
34	D5	45	16:47:00	16:50:00	00:03:00	843	260.84
35	E5	41	16:59:00	17:00:00	00:01:00	830	67.65
36	E6	38	17:03:00	17:05:00	00:02:00	558	12.20
37	E7	37	17:07:00	17:15:00	00:08:00	526	44.71
38	E8	41	17:16:00	17:18:00	00:02:00	504	19.64
39	E4	49	17:21:00	17:23:00	00:02:00	641	8.79
40	E3	58	17:25:00	17:26:00	00:01:00	634	25.36
41	E2	62.5	17:29:00	17:30:00	00:01:00	916	72.43
42	E1	67	17:32:00	17:35:00	00:03:00	571	60.83

Tab. A2: Solfatara, 26th October 2012

N	LINK L-M	DIST	START TIME	END TIME	DURATION	M	DEV.STD
1	A1	122	10:17:07	10:22:33	00:05:26	891	136.39
2	A2	124	10:32:39	10:38:04	00:05:25	827	144.28
3	A3	125	10:38:37	10:41:36	00:02:59	731	118.45
4	A4	129	10:45:55	10:48:09	00:02:14	683	87.42
5	A5	136	10:50:23	10:53:21	00:02:58	613	52.29
6	A6	128	10:54:49	10:59:24	00:04:35	630	120.22
7	B1	116	11:13:07	11:18:15	00:05:08	985	93.33
8	B2	116.5	11:20:04	11:24:42	00:04:38	1166	210.29
9	B3	114	11:25:51	11:31:06	00:05:15	1068	166.89
10	B4	117	11:37:30	11:40:23	00:02:53	692	142.69
11	B5	123	11:42:26	11:45:46	00:03:20	578	70.27
12	B6	114	11:47:37	11:51:25	00:03:48	621	52.76
13	C1	119	12:22:01	12:27:09	00:05:08	768	81.80
14	C2	116	12:27:47	12:31:13	00:03:26	929	167.45
15	C3	112	12:33:12	12:38:24	00:05:12	814	213.20
16	C4	113	12:39:45	12:44:45	00:05:00	690	105.62
17	C5	117	13:52:23	13:57:51	00:05:28	640	52.44
18	C6	105	14:09:51	14:18:57	00:09:06	639	41.57
20	D1	123	14:36:29	14:46:10	00:09:41	452	111.56
21	D2	117	14:47:31	14:51:40	00:04:09	781	142.72
22	D3	112	14:53:13	14:55:55	00:02:42	617	42.52
23	D4	111	14:56:57	15:00:00	00:03:03	566	45.10
24	D5	112	15:01:08	15:05:18	00:04:10	571	49.00
25	D6	98	15:07:44	15:11:17	00:03:33	518	9.90

Tab. A3: Pesciarelli, 29th January 2013

N	LINK L-M	DIST	START TIME	END TIME	DURATION	M	DEV.STD
1	A2	57	09:33:06	09:36:04	00:02:58	511	43.48
2	A3	58	09:40:51	09:46:14	00:05:23	849	148.59
3	A4	55	09:50:26	09:55:36	00:05:10	715	113.03
4	A1	53	10:11:26	10:17:32	00:06:06	461	17.71
5	A5	57	10:19:06	10:26:37	00:07:31	702	98.25
6	A6	53	10:34:34	10:37:27	00:02:53	627	108.56
7	A8	66	10:42:15	10:49:17	00:07:02	572	66.01
8	A7	58	10:53:57	10:57:21	00:03:24	795	65.68
9	B8	57	11:05:26	11:07:31	00:02:05	794	101.37
10	B7	52	11:13:06	11:16:48	00:03:42	590	54.53
11	B5	54	11:24:34	11:33:24	00:08:50	752	91.12
12	B6	49	12:00:43	12:04:12	00:03:29	780	98.99
13	B4	53	12:05:10	12:09:49	00:04:39	683	100.73
14	B3	58	12:11:04	12:13:39	00:02:35	497	29.25
15	B2	60	12:14:23	12:17:04	00:02:41	462	49.64
16	B1	58	12:20:49	12:22:02	00:01:13	479	42.99
17	C1	66	12:32:26	12:37:19	00:04:53	555	53.98
18	C2	67	12:39:56	12:45:02	00:05:06	498	35.64
19	C3	63	12:46:30	12:53:53	00:07:23	420	50.02
20	C4	57	12:55:44	13:01:57	00:06:13	595	118.27
21	C7	47	13:04:13	13:12:33	00:08:20	472	88.62
22	C5	55	13:17:41	13:21:59	00:04:18	964	130.77
23	C6	48	13:25:42	13:29:36	00:03:54	652	199.46
24	C8	51	14:39:52	14:45:35	00:05:43	493	29.75
25	D8	44	14:58:15	15:01:14	00:02:59	456	13.39
26	D7	43	15:02:49	15:04:53	00:02:04	1266	176.79
27	D6	44	15:06:19	15:09:47	00:03:28	747	133.62
28	D4	56	15:12:00	15:16:32	00:04:32	624	78.28
29	D2	69	15:19:32	15:22:23	00:02:51	571	68.64
30	D1	70	15:24:19	15:27:30	00:03:11	558	47.30
31	D3	64	15:35:10	15:39:24	00:04:14	594	89.15
32	D5	53	15:45:02	15:54:29	00:09:27	833	203.67
33	E6	44	16:04:59	16:07:55	00:02:56	572	112.50
34	E5	54	16:09:49	16:13:26	00:03:37	707	126.72
35	E4	57	16:16:15	16:20:35	00:04:20	802	147.32
36	E2	74	16:22:40	16:25:27	00:02:47	646	90.42
37	E3	67	16:28:23	16:31:00	00:02:37	696	80.96
38	E1	77	16:34:24	16:36:30	00:02:06	649	71.57
39	E7	38	16:41:29	16:45:25	00:03:56	930	214.87
40	E8	38	16:51:00	16:56:29	00:05:29	453	61.63
41	F8	32	17:01:24	17:02:34	00:01:10	448	33.51
42	F7	37	17:05:49	17:07:26	00:01:37	567	53.18
43	F2	78	17:35:45	17:37:49	00:02:04	699	22.06
44	F1	81	17:38:27	17:39:48	00:01:21	570	46.99
45	F4	60	17:45:00	17:46:42	00:01:42	434	61.39
46	F3	70	17:49:30	17:51:08	00:01:38	745	55.04
47	F5	55	17:54:07	17:55:40	00:01:33	764	21.47
48	F6	43	17:57:01	17:58:54	00:01:53	484	6.74

Tab. A4: Solfatara, 30th January 2013

N	LINK L-M	DIST	START TIME	END TIME	DURATION	M	DEV.STD
1	A1	52	10:15:51	10:19:46	00:03:55	615	46.53
2	A2	62	10:23:32	10:26:16	00:02:44	603	58.29
3	A3	74	10:28:08	10:31:28	00:03:20	969	72.17
4	A4	79	10:35:39	10:41:33	00:05:54	560	45.47
5	A5	96	10:44:33	10:48:25	00:03:52	828	43.08
6	A6	87	10:50:48	10:52:23	00:01:35	804	82.69
7	B6	81	11:05:31	11:13:44	00:08:13	689	80.86
8	B5	93	11:15:32	11:19:04	00:03:32	758	87.54
9	B4	80	11:21:48	11:23:47	00:01:59	821	209.63
10	B3	77	11:26:00	11:28:47	00:02:47	507	57.55
11	B2	66	11:31:08	11:33:27	00:02:19	657	95.92
12	B1	58	11:34:36	11:36:54	00:02:18	566	41.50
13	C1	66	11:41:10	11:46:17	00:05:07	551	42.78
14	C2	72	11:49:05	11:52:47	00:03:42	1282	174.72
15	C3	80	11:54:39	11:55:06	00:00:27	943	110.61
16	C4	81	11:59:09	12:03:58	00:04:49	692	58.16
17	C6	76	12:09:52	12:12:11	00:02:19	606	132.19
18	C5	89	12:14:15	12:15:44	00:01:29	683	21.28
19	D6	72	12:19:05	12:23:51	00:04:46	665	93.52
20	D5	87	12:25:20	12:29:05	00:03:45	699	129.08
21	D4	84	12:32:15	12:35:33	00:03:18	953	195.17
22	D3	86	12:37:32	12:41:12	00:03:40	772	182.92
23	D2	79	12:42:33	12:46:55	00:04:22	772	120.11
24	D1	75	12:49:09	12:53:16	00:04:07	668	95.10
25	E1	84	12:57:58	13:00:18	00:02:20	811	53.67
26	E2	85	13:01:11	13:03:50	00:02:39	748	121.69
27	E3	92	13:05:06	13:06:22	00:01:16	517	48.75
28	E4	87	13:09:25	13:15:55	00:06:30	695	59.87
29	E5	86	13:18:11	13:23:24	00:05:13	758	67.80
30	E6	70	13:26:16	13:30:42	00:04:26	790	58.02
31	F6	69	13:35:59	13:39:38	00:03:39	610	54.27
32	F5	86	13:41:49	13:43:56	00:02:07	677	51.48
33	F4	92	13:49:16	13:50:37	00:01:21	557	54.69
34	F3	98	13:53:39	13:55:53	00:02:14	1017	156.35
35	F2	93	13:58:19	14:01:36	00:03:17	524	71.91
36	F1	92.5	14:04:23	14:16:25	00:12:02	611	88.83

Tab. A5: Pisciarelli, 8th May 2013

N	LINK L-M	DIST	START TIME	END TIME	DURATION	M	DEV.STD
1	A1	53	08:26:20	08:31:41	0:05:21	646	128.02
2	A2	57	08:32:46	08:36:52	0:04:06	698	173.32
3	A4	53	08:42:03	08:47:22	0:05:19	721	208.76
4	A3	57	08:49:15	08:53:44	0:04:29	805	188.77
5	A6	53	08:58:33	09:03:10	0:04:37	561	86.38
6	A5	57	09:09:26	09:15:46	0:06:20	530	76.07
7	A7	61	09:17:00	09:22:17	0:05:17	479	122.89
8	A8	65	09:26:35	09:30:56	0:04:21	526	129.76
9	B8	58	09:38:01	09:42:01	0:04:00	608	118.47
10	B7	55	09:43:26	09:47:47	0:04:21	616	117.79
11	B6	50	09:48:11	09:52:14	0:04:03	582	142.02
12	B5	55	09:53:00	09:57:00	0:04:00	610	204.23
13	B4	53	09:59:41	10:05:57	0:06:16	650	186.41
14	B3	59	10:14:15	10:19:45	0:05:30	522	93.39
15	B1	58.5	10:21:35	10:26:05	0:04:30	428	112.65
16	B2	61	10:26:47	10:30:57	0:04:10	499	93.92
17	C2	67	10:37:05	10:42:59	0:05:54	638	170.12
18	C8	51	11:23:44	11:28:30	0:04:46	478	73.95
19	C6	49	11:31:50	11:35:50	0:04:00	520	112.01
20	C3	64	11:38:29	11:43:22	0:04:53	485	38.79
21	C4	56	11:46:59	11:52:30	0:05:31	680	124.21
22	C5	56.3	11:54:01	11:57:13	0:03:12	845	144.04
23	C7	50	11:58:36	12:03:31	0:04:55	543	117.79
24	C1	66.8	12:05:08	12:08:58	0:03:50	577	81.22
25	D5	52	12:19:00	12:23:00	0:04:00	573	131.07
26	D4	54	12:24:22	12:28:02	0:03:40	517	96.99
27	D3	63	12:29:35	12:33:05	0:03:30	414	30.54
28	D2	70	12:34:47	12:39:01	0:04:14	568	124.69
29	D1	71	12:40:57	12:45:46	0:04:49	561	144.32
30	D6	43	12:46:08	12:51:25	0:05:17	518	102.00
31	D7	42	12:52:52	12:59:16	0:06:24	667	160.83
32	D8	41	13:10:32	13:16:00	0:05:28	594	144.04
33	E8	37	15:10:09	15:14:59	0:04:50	567	96.12
34	E7	39	15:16:33	15:21:49	0:05:16	770	121.04
35	E6	43	15:23:58	15:28:27	0:04:29	613	82.38
36	E3	66	15:30:43	15:36:16	0:05:33	574	101.17
37	E2	74	15:37:31	15:43:18	0:05:47	457	58.65
38	E1	76	15:45:10	15:49:08	0:03:58	506	74.02
39	E4	56	15:51:12	15:55:00	0:03:48	585	96.78
40	E5	53	15:55:54	15:59:38	0:03:44	729	146.84
41	F8	32	16:04:27	16:11:14	0:06:47	596	132.84
42	F7	34	16:23:54	16:30:06	0:06:12	988	219.26
43	F5	53	16:30:30	16:34:00	0:03:30	765	50.00
44	F4	57.2	16:34:11	16:38:40	0:04:29	647	110.11
45	F2	76.4	16:41:44	16:45:19	0:03:35	647	158.54
46	F1	80	16:47:06	16:52:53	0:05:47	503	86.47
47	F3	70	17:01:27	17:05:44	0:04:17	656	91.52
48	F6	43	17:06:54	17:12:53	0:05:59	772	163.09

Tab. A6: Solfatara, 9th May 2013

N	LINK L-M	DIST	START TIME	END TIME	DURATION	M	DEV.STD
1	A1	49	09:16:25	09:21:07	0:04:42	627	93.49
2	A2	57.6	09:22:19	09:25:51	0:03:32	564	59.45
3	A3	74	09:27:37	09:32:02	0:04:25	676	104.71
4	A4	83	09:33:31	09:37:03	0:03:32	677	84.26
5	A5	96	09:40:30	09:45:59	0:05:29	589	139.97
6	A6	86	09:47:00	09:50:59	0:03:59	501	58.90
7	B6	84	09:51:03	09:54:55	0:03:52	533	56.62
8	B5	98	09:56:15	09:59:15	0:03:00	528	63.82
9	B4	86	09:59:58	10:03:00	0:03:02	803	122.39
10	B3	80	10:04:37	10:08:45	0:04:08	575	108.18
11	B2	65	10:09:43	10:13:31	0:03:48	522	80.71
12	B1	58	10:14:16	10:20:27	0:06:11	489	73.11
13	C6	80	10:23:01	10:28:35	0:05:34	502	74.30
14	C5	98	10:29:48	10:33:28	0:03:40	836	95.98
15	C4	91	10:33:52	10:38:34	0:04:42	667	92.64
16	C3	86	10:39:06	10:43:55	0:04:49	758	157.27
17	C2	73	10:44:12	10:47:57	0:03:45	503	41.96
18	C1	69	10:48:36	10:52:16	0:03:40	482	36.45
19	D6	80	10:53:44	10:57:32	0:03:48	455	63.90
20	D5	100	10:58:26	11:01:59	0:03:33	590	58.15
21	D4	97	11:02:34	11:05:34	0:03:00	959	115.76
22	D3	93	11:05:54	11:09:21	0:03:27	657	123.16
23	D2	81	11:09:54	11:13:21	0:03:27	478	60.64
24	D1	78	11:13:58	11:19:00	0:05:02	426	36.52
25	F6	80	11:19:59	11:22:57	0:02:58	519	45.06
26	F5	106	11:23:35	11:26:07	0:02:32	481	52.75
27	F4	110	11:26:52	11:29:47	0:02:55	919	112.02
28	F3	109.5	11:31:56	11:35:40	0:03:44	538	68.84
29	F2	98	11:36:54	11:39:10	0:02:16	522	36.31
30	F1	97	11:39:31	11:43:31	0:04:00	581	61.06
31	E6	78.3	11:46:29	11:49:51	0:03:22	557	64.40
32	E5	101.6	11:51:39	11:54:59	0:03:20	516	43.95
33	E4	102.6	11:55:03	11:58:29	0:03:26	701	63.68
34	E3	101.1	11:59:06	12:01:11	0:02:05	766	111.21
35	E2	89.5	12:01:34	12:04:49	0:03:15	730	135.94
36	E1	87.1	12:05:28	12:08:50	0:03:22	545	66.30

Tab. A7: Nea Kameni, 9th April 2013

N	LINK L-M	DIST	START TIME	END TIME	DURATION	M	DEV.STD
1	A1	71	09:24:28	09:28:01	03:33	515	25.32
2	A2	65	09:30:19	09:33:16	02:57	386	13.93
3	A3	65.5	09:34:50	09:37:28	02:38	400	23.27
4	A4	67	09:41:28	09:47:25	05:57	432	29.06
5	A5	70	09:51:29	09:54:08	02:39	506	19.59
6	A6	70.5	09:59:54	10:04:42	04:48	462	14.94
7	B6	59	10:10:59	10:13:39	02:40	392	18.93
8	B5	61	10:16:52	10:19:20	02:28	371	7.64
9	B2	65	10:20:52	10:26:01	05:09	406	18.77
10	B1	75	10:28:07	10:30:28	02:21	379	17.50
11	B4	61	10:37:48	10:40:21	02:33	410	23.01
12	B3	62	10:45:41	10:47:59	02:18	384	17.87
13	C6	48	10:56:14	10:59:04	02:50	379	12.32
14	C5	51	10:59:53	11:02:05	02:12	367	14.08
15	C4	53	11:03:48	11:05:54	02:06	559	36.15
16	C3	57	11:10:00	11:13:00	03:00	450	10.00
17	C2	61	11:18:11	11:21:00	02:49	371	8.44
18	C1	73	11:21:45	11:23:56	02:11	421	28.72
19	D1	70	11:28:22	11:31:00	02:38	474	22.75
20	D2	57	11:32:16	11:33:52	01:36	474	16.16
21	D3	52	11:34:33	11:36:36	02:03	472	26.33
22	D5	42	11:50:30	11:53:13	02:43	434	17.28
23	D6	37	11:53:58	11:57:04	03:06	377	1.15
24	D4	46	12:00:47	12:03:14	02:27	374	12.90
25	E1	70	12:07:12	12:09:38	02:26	416	18.82
26	E2	56	12:10:00	12:12:38	02:38	435	7.06
27	E4	41	12:13:42	12:16:48	03:06	500	49.64
28	E5	34	12:18:29	12:20:34	02:05	394	31.39
29	E6	28	12:28:37	12:31:40	03:03	425	12.18
30	E3	49	12:33:28	12:35:32	02:04	445	26.66
31	F1	65	12:58:24	13:00:26	02:02	402	10.30
32	F2	51	13:01:59	13:04:02	02:03	404	6.72
33	F3	43	13:06:32	13:10:24	03:52	407	23.14
34	F4	32	13:24:19	13:27:13	02:54	452	24.31
35	F6	15	13:28:58	13:34:45	05:47	604	43.37
36	F5	23	13:36:40	13:39:28	02:48	508	26.14

Tab. A8: Hekla, 2nd July 2013

N	LINK L-M	DIST	START TIME	END TIME	DURATION	M	DEV.STD
1	A1	12	16:49:44	16:53:13	03:29	1337	146.92
2	A2	18	16:59:54	17:02:30	02:36	965	39.56
3	A3	28	17:05:18	17:11:27	06:09	635	26.66
4	B3	33	17:17:10	17:22:55	05:45	1119	40.82
5	B2	21	17:26:09	17:30:39	04:30	881	34.41
6	B1	19	17:34:04	17:37:18	03:14	925	52.42
7	C1	17	17:39:19	17:42:17	02:58	617	102.21
8	C2	20	17:44:23	17:46:49	02:26	820	31.28
9	C3	35	17:48:13	17:52:52	04:39	842	25.88

Tab. A9: Krýsuvík, 5th July 2013

N	LINK L-M	DIST	START TIME	END TIME	DURATION	M	DEV.STD
1	B4	36.8	12:01:53	12:07:18	05:25	400	4.22
2	B1	33	12:08:39	12:14:02	05:23	385	22.50
3	B2	55	12:16:02	12:18:35	02:33	439	18.69
4	B3	53	12:19:19	12:23:17	03:58	373	5.33
5	A1	30	12:27:28	12:30:10	02:42	408	7.70
6	A2	55	12:31:21	12:33:15	01:54	432	15.02
7	A3	58	12:34:05	12:36:47	02:42	408	4.20
8	A4	46	12:37:28	12:40:12	02:44	398	2.34
9	C4	27	12:43:45	12:46:05	02:20	393	5.96
10	C3	48.5	12:47:34	12:49:59	02:25	467	17.91
11	C2	55	12:50:50	12:54:36	03:46	381	3.17
12	C1	38	12:55:35	12:58:13	02:38	390	3.12
13	D3	51	13:05:11	13:07:57	02:46	403	8.60
14	D2	60	13:08:52	13:12:30	03:38	405	4.97
15	D1	47	13:13:19	13:16:41	03:22	371	7.90
16	D4	22.5	13:18:25	13:21:09	02:44	388	7.30
17	D5	60	13:22:41	13:24:13	01:32	374	3.30
18	C5	56.5	13:26:15	13:27:52	01:37	514	37.46
19	B5	58	13:30:11	13:32:24	02:13	415	25.27
20	A5	61	13:33:32	13:34:52	01:20	420	5.82

Tab. A10: Vulcano, 11th March 2014

N	LINK L-M	DIST	START TIME	END TIME	DURATION	M	DEV.STD
1	A1	204	13:19:03	13:23:27	04:24	649	15.53
2	A4	234	13:34:11	13:40:35	06:24	637	26.45
3	A5	244	13:42:36	13:49:09	06:33	653	24.97
4	A2	217	13:50:04	13:52:32	02:28	614	8.69
5	A3	226	13:56:28	13:59:19	02:51	576	70.96
6	B1	225	14:03:53	14:05:41	01:48	623	25.63
7	B4	253	14:06:16	14:13:59	07:43	616	23.86
8	B2	239	14:17:31	14:20:37	03:06	610	27.59
9	B5	261	14:22:39	14:27:18	04:39	583	39.85
10	C1	253	14:35:42	14:37:44	02:02	621	8.01
11	C2	262	14:39:12	14:44:07	04:55	641	38.76
12	C4	270	14:44:56	14:46:39	01:43	636	20.05
13	C5	275	14:47:04	14:52:22	05:18	613	32.78
14	D1	276	15:03:31	15:05:13	01:42	609	10.24
15	D2	282	15:06:06	15:07:20	01:14	609	27.27
16	D3	283	15:08:28	15:09:41	01:13	632	19.83
17	D4	284	15:10:02	15:12:31	02:29	629	22.88
18	D5	285	15:13:07	15:21:07	08:00	665	23.68
19	E1	296	15:21:43	15:23:17	01:34	624	22.66
20	E4	294	15:23:35	15:25:07	01:32	620	9.93
21	E5	292	15:25:35	15:28:04	02:29	637	28.65
22	E2	300	15:28:38	15:33:54	05:16	567	94.41
23	E3	297	15:36:51	15:40:05	03:14	610	40.71
24	F1	316	15:46:05	15:48:23	02:18	619	22.30
25	F4	303	15:49:00	15:50:23	01:23	687	37.25
26	F5	296	15:51:13	15:52:56	01:43	660	66.33
27	F2	315	15:53:37	15:56:24	02:47	639	59.44
28	A6	283	15:57:00	15:59:02	02:02	580	70.20
29	B6	283	16:00:01	16:02:00	01:59	570	65.00
30	C6	282	16:02:38	16:04:00	01:22	570	41.70
31	D6	287	16:05:00	16:07:00	02:00	600	21.00
32	E6	286	16:09:00	16:11:28	02:28	600	9.05
33	F6	288	16:14:18	16:17:00	02:42	580	8.01
34	B3	237	16:18:45	16:21:00	02:15	620	24.00
35	C3	262	16:22:34	16:25:00	02:26	655	18.03
36	F3	311	16:26:35	16:29:00	02:25	690	17.69

Tab. A11: Paternò, 4th April 2014

N	LINK L-M	DIST	START TIME	END TIME	DURATION	M	DEV.STD
*1	A1	38	10:35:30	10:40:27	04:57	750	47.41
2	A3	75	10:42:00	11:08:43	26:43	562	5.68
3	A2	57	11:11:37	11:14:57	03:20	587	44.89
4	A4	90	11:16:06	11:18:21	02:15	600	13.45
5	A5	106	11:19:29	11:21:54	02:25	570	13.25
6	A6	116	11:23:02	11:25:45	02:43	485	6.57
7	B1	57	11:30:33	11:35:05	04:32	519	66.40
8	B2	58	12:42:23	12:56:57	14:34	555	43.54
9	B3	65	12:57:55	13:01:57	04:02	430	71.81
10	B4	71	13:04:02	13:07:23	03:21	496	50.39
11	B5	83	13:08:23	13:13:47	05:24	509	56.60
12	B6	89	13:15:10	13:22:56	07:46	539	8.60
13	C1	83	13:24:05	13:30:17	06:12	569	46.76
14	C2	70	13:33:07	13:37:07	04:00	675	27.10
15	C3	65	13:38:39	13:49:52	11:13	444	40.73
16	C4	57	13:51:25	13:55:01	03:36	503	66.31
17	C5	58	13:55:30	14:00:59	05:29	473	27.97
18	C6	60	14:01:11	14:13:11	12:00	452	43.21
19	D6	52	14:18:55	14:28:55	10:00	476	7.60
20	D5	58	14:33:43	14:38:08	04:25	483	64.07
21	D4	66	14:39:05	14:40:30	01:25	508	56.17
22	D3	80	14:43:54	14:47:41	03:47	495	45.85
23	D2	91	14:49:24	14:52:45	03:21	447	65.59
24	D1	107	14:55:21	14:58:23	03:02	472	51.34

*eliminated path for the contour map reconstruction

Tab. A12: Furnas Lake, 19th August 2014

N	LINK L-M	DIST	START TIME	END TIME	DURATION	M	DEV.STD
1	A1	39	10:59:52	11:07:12	07:20	594	84.65
2	A2	56	11:08:17	11:14:57	06:40	692	103.99
3	A3	62	11:15:40	11:22:12	06:32	534	51.88
4	B1	44	11:25:57	11:28:40	02:43	595	44.20
5	B2	61	11:29:52	11:35:21	05:29	615	99.98
6	B3	60.5	11:36:10	11:39:43	03:33	574	90.23
7	C3	62	11:43:26	11:46:22	02:56	662	36.61
8	C2	66	11:47:08	11:52:39	05:31	605	81.50
9	C1	51	11:55:18	12:03:47	08:29	532	61.06
10	D1	60	12:33:05	12:45:00	11:55	463	56.56
11	D2	71	12:56:12	13:07:34	11:22	499	91.91
12	D3	65	13:09:13	13:28:42	19:29	493	76.88
13	E3	68	13:33:20	13:40:45	07:25	896	123.78
14	E2	78	13:41:42	13:49:23	07:41	400	36.92
15	E1	68	13:51:31	13:54:16	02:45	635	95.76
16	A6	43	15:17:23	15:25:53	08:30	579	63.08
17	A5	48	15:26:33	15:28:47	02:14	508	28.31
18	A4	56	15:29:54	15:32:28	02:34	615	35.13
19	B4	53	15:36:46	15:45:14	08:28	548	78.68
20	B5	41	15:46:03	15:48:42	02:39	585	45.22
21	B6	34	15:50:03	15:52:59	02:56	485	37.61
22	C6	29	15:56:33	15:58:29	01:56	415	20.20
23	C5	37	15:59:46	16:02:03	02:17	522	24.48
24	C4	53	16:03:05	16:07:04	03:59	790	132.00
25	D4	55	16:54:40	16:58:27	03:47	601	101.13
26	D5	33	16:59:18	17:01:31	02:13	422	40.23
27	D6	27	17:02:57	17:10:45	07:48	455	4.37
28	E4	57	17:13:47	17:18:55	05:08	545	72.90
29	E5	31	17:20:29	17:22:55	02:26	504	72.21
30	E6	23	17:24:20	17:30:14	05:54	500	10.46

Tab. A13: Furnas Village, 22nd August 2014

N	LINK L-M	DIST	START TIME	END TIME	DURATION	M	DEV.STD
1	A1	51	13:17:12	13:20:52	03:40	564	46.50
2	A2	61	13:21:33	13:26:54	05:21	596	21.96
3	A3	59	13:28:39	13:33:24	04:45	599	63.70
4	B1	51	13:38:39	13:42:35	03:56	592	50.34
5	B2	59	13:43:46	13:47:06	03:20	662	79.84
6	B3	57	13:47:57	13:52:30	04:33	594	39.79
7	C1	46	13:57:24	13:59:31	02:07	679	56.76
8	C2	54	14:00:08	14:07:00	06:52	617	40.02
9	C3	51	14:07:53	14:14:22	06:29	573	72.96
10	D1	37	14:26:31	14:29:00	02:29	533	57.82
11	D2	43	14:31:37	14:36:02	04:25	601	58.55
12	D3	38	14:37:01	14:41:24	04:23	622	79.27
13	E1	36	14:51:15	15:00:46	09:31	654	75.74
14	E2	37	15:01:41	15:05:08	03:27	589	31.86
15	E3	29	15:06:19	15:10:14	03:55	549	60.11
16	A4	34	16:18:08	16:29:41	11:33	498	77.58
17	A5	43	16:31:26	16:34:21	02:55	527	35.34
18	A6	59	16:35:30	16:39:59	04:29	612	45.97
19	B4	34	16:56:29	16:59:47	03:18	600	58.41
20	B5	44	17:00:34	17:05:08	04:34	653	129.21
21	B6	56	17:06:27	17:10:50	04:23	682	39.17
22	C4	31	17:15:11	17:19:09	03:58	683	68.49
23	C5	40	17:20:08	17:21:55	01:47	702	78.78
24	C6	51	17:22:51	17:25:13	02:22	636	62.84
25	D4	27	17:35:18	17:38:47	03:29	851	35.45
26	D5	32	17:39:56	17:41:31	01:35	708	77.39
27	D6	34	17:42:36	17:44:11	01:35	622	28.78
28	E4	36	17:53:02	17:55:41	02:39	539	46.81
29	E5	35	17:56:26	17:58:23	01:57	538	36.72
30	E6	27	17:59:01	18:03:01	04:00	434	26.92